

UC Irvine

UC Irvine Electronic Theses and Dissertations

Title

Spin Torque and Spin-Dependent Transport in Nanoscale Devices

Permalink

<https://escholarship.org/uc/item/6zz2m4tb>

Author

Chen, Jen-Ru

Publication Date

2018

Peer reviewed|Thesis/dissertation

UNIVERSITY OF CALIFORNIA,
IRVINE

Spin Torque and Spin-Dependent Transport in Nanoscale Devices

THESIS

submitted in partial satisfaction of the requirements
for the degree of

DOCTOR OF PHILOSOPHY

in Chemical and Material Physics

by

Jen-Ru Chen

Thesis Committee:
Professor Ilya N. Krivorotov, Chair
Professor Wilson Ho
Professor Zuzanna S. Siwy

2018

TABLE OF CONTENTS

	Page
LIST OF FIGURES	iv
ACKNOWLEDGMENTS	viii
CURRICULUM VITAE	ix
ABSTRACT OF THE THESIS	xi
1 Introduction	1
2 Background	3
2.1 Magnetoresistance	3
2.1.1 Giant Magnetoresistance (GMR)	3
2.1.2 Tunneling Magnetoresistance (TMR)	7
2.2 Lateral Spin Transport Devices	10
2.2.1 Non-local Measurements and Spin Diffusion	10
2.2.2 Spin Injection and Detection	12
2.3 Spin Hall Effect	13
2.4 Magnetization Dynamics	15
2.4.1 Spin Transfer Torque (STT)	15
2.4.2 Spin Torque Oscillator (STO) and Spin Hall Oscillator (SHO)	18
2.5 Topological Insulator	18
2.5.1 Topological Surface States	19
3 Experimental Details	21
3.1 Nano-Fabrications Instruments and Methods	21
3.1.1 Sputtering Deposition	21
3.1.2 Electron Beam Evaporation	23
3.1.3 Scanning Electron Microscopy and Electron Beam Lithography	23
3.1.4 Ion Miller Etching	24
3.1.5 In-Filed Oven Annealing	25
3.2 Device Fabrication Procedures	25
3.2.1 Nanofabrication of GMR-based SHO Nanowire Devices	25
3.2.2 Nanofabrication of Sb ₂ Te ₃ Lateral Devices	33

4	GMR-based and AMR-based SHOs	38
4.1	Introduction	38
4.2	SHO nanowire devices, GMR and Spectrum	41
4.3	Integrated power analysis	45
4.4	Angular dependence	46
4.5	Conclusion	49
5	Ionizing Radiation Effect on Perpendicular Magnetic Tunnel Junctions	50
5.1	Introduction	50
5.2	Irradiation considerations	53
5.3	Experimental Details and Data	54
5.4	Conclusion	60
6	Spin-dependent transport properties in lateral Sb_2Te_3 nanowire devices	62
6.1	Introduction	62
6.2	Synthesis and fabrication of Sb_2Te_3 nanowire devices	63
6.3	Magneto-transport properties of lateral Sb_2Te_3 nanowire devices	65
6.4	Temperature dependence of Magneto-transport properties	74
	Bibliography	76

LIST OF FIGURES

	Page
2.1 GMR effect in Fe/Cr superlattices. (Adapted from [1])	4
2.2 Top: The schematic drawings of two spin polarity electrons going through FM/NM/FM multilayers. The left graph shows parallel (P) state of two FM layers. The electron with the same spin orientation as the FM layers pass through this multilayer straightly while the electron with opposite spin orientation is largely scattered when passing through FM layer. The right graph shows anti-parallel (AP) state. Both electrons go straight through in one layer and scatter in another layer. Bottom: The Mott two-current model of P and AP states of FM/NM/FM structure correspond to the tops. The same-spin and opposite-spin channel is represented as R_1 and R_2	6
2.3 Julliere model for tunneling magnetoresistance.	9
2.4 Lateral spin valves in a non-local measurement geometry, with schematic for the geometry.	11
2.5 Spin Injection at FM/NM Interface. Top: Schematic of the interface between a ferromagnetic metal (FM) and a non-magnetic metal (NM). Bottom: Adapted from [2]. Spin-dependent chemical potentials as a function of position at the interface of FM and NM materials.	13
2.6 The schematic of spin Hall effect (SHE). The spin-up (green) and spin-down (red) charge carriers are deflected perpendicular from its original trajectories and imbalance accumulated to the two edges $y = 0$ and $y = L$. The right graph shows that the electric voltages at two edges are the same, V_{SH} , however spin dependent chemical potential differently.	15
2.7 A example schematic shows spin transfer torques (STTs). The random spin electron current is polarized when pass through the FM1. This spin polarized current is transferred to FM2 and exert torque to local magnetic moment due to exchange interaction. After interaction, both magnetization in FM2 and transferred carriers change its spin orientations.	16
2.8 Illustration of the affection of spin transfer torque (STT) that leads to different motions of magnetic moment. If $\tau_{st} < \tau_d$, the magnetic moment relax back to its equilibrium. If $\tau_{st} \approx \tau_d$, the magnetic moment moves along a stable trajectory and self-oscillates. If $\tau_{st} > \tau_d$, the magnetic moment could oscillates in a larger and larger trajectory and eventually switches to another equilibrium position. [3]	17

2.9	Left: Dirac cone of the TI surface states, with the spin at right angles to the momentum at each point. Right: Top view of the $k_x - k_y$ plane of the TI surface states. An applied voltage produces a net momentum along k_x and spin-momentum locking gives rise to a net spin polarization oriented in-plane and at right angles to the current.	20
3.1	Left: The mechanism of sputtering deposition system. Right: The pictures of AJA magnetron sputtering system in the Lab.	22
3.2	The SEM image of a Sb_2Te_3 nanoribbon. The scale bar is 500 nm.	24
3.3	The drawing of an alignment mark used for milling defined nanowire devices.	27
3.4	The drawing of a nanowire geometry.	28
3.5	SEM images of a GMR-based SHO nanowire device. Top left: The 60,000x magnification image. Top right: The 15,000x magnification image. Bottom right: The 4000x magnification image. Bottom left: The 500x magnification image.	30
3.6	Nano-fabrication procedures.	31
3.7	Nano-fabrication procedures.	32
3.8	The drawings of an alignment mark used for random located nanowires.	34
3.9	The SEM image of a Sb_2Te_3 nanowire with a cross nearby to define it's coordinates.	35
3.10	The drawing of four electrodes contacts for randomly located small nanowires.	36
3.11	The SEM image of a lateral Sb_2Te_3 nanowire device with four Co (40 nm)/Al(5 nm) electrodes.	37
4.1	(a) The schematic of AMR-based SHO structure which includes one FM layer and one HM layer. The in-plane DC current flow through the HM layer to generate spin current in in-plane perpendicular direction via Spin Hall effect and add onto the FM layer. The top two equation simply imply the behavior that AC output power is proportional to resistance oscillation. The amplitude of resistance oscillation comes from MR, which is GMR or AMR here. And the GMR magnitude is much larger than AMR magnitude. (b) The schematic of GMR-based SHO structure, which includes a free FM layer, a normal metal (NM) layer, a fixed FM layer and a AFM layer. (c) The normalized AMR angular dependence plot. The AMR variance is proportional to $\cos(\theta)^2$. (d) The normalized GMR angular dependence plot. The GMR variance is proportional to $(1 - \cos(\theta))/2$	40
4.2	(a)/(b) The scanning electron microscopy (SEM) image of GMR/AMR-based SHO nanowire device and it's multilayer structure showing on the bottom.	42
4.3	(a)/(b) The MR of the GMR-based SHO device with the magnetic field applying in-plane parallel to the easy/hard axis.	43
4.4	The MR of the AMR-based SHO device with the magnetic field applying in-plane parallel to the nanowire axis.	44

4.5	(a) Current bias (I_{dc}) dependent power spectral density (PSD) of GMR-based SHO device at $H = 800$ G. (b) Current bias (I_{dc}) dependent PSD of AMR-based SHO device at $H = 800$ G. (c) The PSD cross line profile of GMR-based SHO spectrum at $I_{dc} = 6$ mA. (d) The PSD cross line profile of AMR-based SHO spectrum at $I_{dc} = 3.65$ mA.	45
4.6	(a) The bias dependent auto-oscillation integral microwave power of GMR based SHO (blue) and AMR-based SHO (red). (b) The enlarge image of the red curve plotted in (a).	47
4.7	(a) The angular dependence of the integral power of GMR-based SHO at $H = 500$ G. θ indicates the angle of applied external field related to the nanowire axis. The bottom graph shows the single spectra of θ equals to 90, 80, and 70 degree. The integrated power decreases as the θ increases. (b) The angular dependence of the integral power of AMR-based SHO at $H = 500$ G.	48
5.1	Schematic of a perpendicular MTJ.	52
5.2	(a) Field and b current induced switching characteristics before and after neutron irradiation.	56
5.3	Before and after gamma irradiation results for 23 circular devices. (a) From top to bottom, TMR ratio; center of bistable field H_o ; width of switching field H_w . (b)/(c) The distribution of $\Delta H_o/\Delta H_w$ for 23 circular devices. $\Delta H_o/\Delta H_w$ is defined as $H_o^{after}/H_w^{after} - H_o^{before}/H_w^{before}$	57
5.4	Before and after gamma irradiation results for 23 circular devices. (a) top: center value of current switching loop I_o ; bottom: width of current switching loop I_w (b)/(c) The distribution of $\Delta I_o/\Delta I_w$ for 23 circular devices. $\Delta I_o/\Delta I_w$ is defined as $I_o^{after}/I_w^{after} - I_o^{before}/I_w^{before}$	58
5.5	Before and after TRIGA [®] (neutron + gamma) irradiation results for 66 elliptical devices. (a) From top to bottom, TMR ratio; center of bistable field H_o ; width of switching field H_w . (b)/(c) The distribution of $\Delta H_o/\Delta H_w$ for 66 elliptical devices.	59
5.6	Before and after TRIGA (neutron + gamma) irradiation results for 66 elliptical devices. (a) top: center value of current switching loop I_o ; bottom: width of current switching loop I_w (b)/(c) The distribution of $\Delta I_o/\Delta I_w$ for 66 elliptical devices.	60
6.1	Schematic of the nonlocal spin valve device on a TI Sb_2Te_3 nanowire channel.	64
6.2	SEM image of the device with two inner Py/Cu/Co/CoO _x composite spin valve electrodes and two outer Nb/Au non-magnetic electrodes.	65
6.3	The temperature dependent magneto-transport measured through two Nb/Au contacts with the sweeping magnetic field applied along the electrodes (out-of-plane to the two side walls of Sb_2Te_3 nano-ribbon). The magnetoresistance (MR) behavior shows the weak anti-localization (WAL) effect at low temperature and decreases as temperature goes up, which suggests a conduction in Fermi Dirac states in the Sb_2Te_3 nanowire	66
6.4	The two-point magnetoresistance measured through T1 and T2 with magnetic field applied (a) perpendicular (b) parallel to the FM T2 electrode.	68

6.5	The two-point magnetoresistance measured through T3 and T4 with magnetic field applied (a) perpendicular (b) parallel to the FM T3 electrode.	69
6.6	The electrical detection of spin-momentum locking (SML) effect of the lateral Sb₂Te₃ nanowire device. (a), (b) The field dependent voltage measured by applying current across T3 and T4 and detecting through T2 and T1 for +24 μ A and -24 μ A, respectively. (c)/(d) schematic drawings of a positive current applied through T3 to T4 and the magnetization of FM electrodes point down/up. (e), (f) schematic drawings of a negative current applied through T3 to T4 and the magnetization of FM electrodes point down/up.	72
6.7	The electrical detection of spin-momentum locking (SML) effect of the lateral Sb₂Te₃ nanowire device. (a), (b) The field dependent voltage measured by applying current across T1 and T3 and detecting through T2 and T4 for +24 μ A and -24 μ A, respectively. (c)/(d) schematic drawings of a positive current applied through T1 to T3 and the magnetization of FM electrodes point down/up. (e), (f) schematic drawings of a negative current applied through T1 to T3 and the magnetization of FM electrodes point down/up.	73
6.8	Temperature dependence of SML effect in the lateral Sb₂Te₃ nanowire device. Top shows the circuit schematic. The non-locally detected voltages measured from 4 K to 120 K.	75

ACKNOWLEDGMENTS

I would like to thank my advisor, Professor Ilya Krivorotov, who has been patient and supportive to guide me into the research. He is one of most knowledgeable physicists I have ever met. It has been a great pleasure to discuss with him and learn from him.

I also want to thank everyone in Ilya's group: Igor Barsukov, Eric Montoya, Zheng Duan, Brian Youngblood, Liu Yang, Yu-Jin Chen, Han Kyu Lee, Andrew Smith, Jieyi Zhang, Alejandro Jara, Chris Safranski, Josh Dill, Chengcen Sha, Amanatullah Khan (Mishu), Mara Mishner, and Joshua Yang. I really enjoy the heritage of our group, which people respect to each other and help each other as much as they can in research.

CURRICULUM VITAE

Jen-Ru Chen

EDUCATION

Master of Science in Chemical and Material Physics University of California, Irvine	2018 <i>Irvine, CA</i>
Master of Science in Physics National Taiwan University	2007 <i>Taipei, Taiwan</i>
Bachelor of Science in Physics National Taiwan University	2004 <i>Taipei, Taiwan</i>

RESEARCH EXPERIENCE

Graduate Research Assistant University of California, Riverside	2010–2013 <i>Riverside, California</i>
Graduate Research Assistant University of California, Irvine	2013–present <i>Irvine, California</i>

TEACHING EXPERIENCE

Teaching Assistant University of California, Riverside	2010–2012 <i>Riverside, California</i>
Teaching Assistant University of California, Irvine	2013–2014 <i>Irvine, California</i>

REFEREED JOURNAL PUBLICATIONS

Jen-Ru Chen, Patrick M Odenthal, Adrian G Swartz, George Charles Floyd, Hua Wen, Kelly Yunqiu Luo, Roland K Kawakami., Control of Schottky barriers in single layer MoS₂ transistors with ferromagnetic contacts, *Nano letters* 13 (7), 3106 (2013)

REFEREED CONFERENCE PUBLICATIONS

Jen-Ru Chen, E. Montoya, H. K. Lee, C. Sha, R. Ngelale, H. W. Tseng, L. Wan, E. Yang, M. Nilsson, O. Boyraz, N. Bagherzadeh, and Ilya Krivorotov., Effect of Ionizing Radiation on CoFeB/MgO/CoFeB Nanoscale Magnetic Tunnel Junctions, *Magnetism and Magnetic Materials*, Oral (2017)

Jen-Ru Chen, Andrew Smith, and Ila Krivorotov., Enhancement of spin Hall oscillator (SHO) power via giant magneto-resistance (GMR) effect, *Magnetism and Magnetic Materials*, Oral (2016)

Jen-Ru Chen, P. Odenthal, and R. Kawakami., Electrical transport and contact characteristics of single layer MoS₂ devices, *APS meeting*, Oral (2013)

ABSTRACT OF THE THESIS

Spin Torque and Spin-Dependent Transport in Nanoscale Devices

By

Jen-Ru Chen

Doctor of Philosophy in Chemical and Material Physics

University of California, Irvine, 2018

Professor Ilya N. Krivorotov, Chair

Spin Hall effect in a heavy metal (HM) generates a pure spin current flowing perpendicular to an applied electric charge current. When injected into a ferromagnet (FM), this pure spin current can act as negative magnetic damping thereby exciting self-oscillations of magnetization. In a simple HM/FM bilayer geometry, the current-driven self-oscillations of magnetization result in a microwave voltage generation due to anisotropic magneto-resistance (AMR) of the FM. Since AMR in thin films of typical FM materials such as Permalloy (Py) is relatively small, the output microwave signal generated by the HM/FM bilayer spin Hall oscillators (SHOs) is typically limited to ~ 0.1 nW. In this thesis, a new type of SHO by replacing FM layer with spin valve multilayers. In this type of devices, the microwave power generation relies on current-in-plane (CIP) giant magneto-resistance (GMR) instead of AMR. Since the magnitude GMR typically exceeds that of AMR, this new type of SHO can generate significantly higher power than the AMR-based SHOs. The maximum microwave power generated by the device exceeds 1 nW, which is over an order of magnitude higher than that in HM/FM bilayer SHO nanowire devices.

Spin Transfer Torque Random Access Memory (STT-RAM) is a promising non-volatile memory technology that offers scalable area, fast operation, and low power consumption advantages over traditional SRAM, DRAM, and flash memories. Performance of the STT-RAM

sensitively depends on magnetic anisotropy and properties of the magnetic tunnel junctions (MTJs), which is the most essential part in STT-RAM. We present here the results on the effect of ionizing radiation on perpendicular-anisotropy MTJs (PMTJs). These samples were exposed to both gamma radiation and a mix of gamma and thermal neutron, using the TRIGA[®] reactor. The study was on TMR, the electrical transport measurements taken on the MTJ nanopillars, both before and after the irradiation. Our results match the previous study[4], in which no explicit changes on TMR curves of MTJs after the gamma and neutron irradiation. We also investigated the radiation effect on current switching TMR loop of PMTJs that no one reported before. To be confirmed robustness of MTJs statistically, more than 150 devices were investigated in this study.

Non-local lateral devices have been extensively employed for studies of spin-dependent transport in a wide range of non-magnetic (NM) metals and semiconductors. In these devices, pure spin currents in non-magnetic channel materials can be generated and their propagation and decay can be electrically detected. We have successfully observed a non-local spin valve signal in a topological insulator (TI) channel material Sb_2Te_3 . The characteristic property of TI, spin-momentum locking (SML), was identified. The spins of the TI Dirac surface state lies in-plane, and is locked at right angles to the electrons' momentum.

Chapter 1

Introduction

Spin-related electronics, or spintronics, aims to utilize spin degree of freedom of electrons for applications in computer logic and information storage. Many significant state of the art studies have been made in the field towards applications that could replace standard Si-based electronics. For example, the discovery of giant magnetoresistance (GMR) (Nobel Prize in Physics 2007)[1, 5] and tunneling magnetoresistance[6–8] has improved magnetic sensing technology and increased hard drive storage. A new type of non-volatile memory, spin transfer torque random access memory (STT-RAM) is developing rapidly towards to be a real application commercially. Also, much of the field in spintronics takes advantage of the spin-polarized nature of ferromagnetic materials. Recently, there have been more advances on trying to realize spin dynamics and spin-related quantum effect in systems such as spin torque oscillators (STOs) and topological insulators (TIs).

In this thesis, the focus of spin dynamics is on GMR-based spin Hall oscillator (SHO) nanowire devices. The study of ionizing radiation effect on magnetic tunnel junctions (MTJs) which is the core element of STT-RAMs is also an important topic here. Finally, the spin-dependent transport behavior in topological insulator is explored and studied.

Chapter 2 covers the background of spin-related physics for understanding the topics. In Chapter 3, the nano-fabrication of different types of nanowire devices, including the introduction of instruments and fabrication procedures, is addressed. The motivation and experimental results for the study of GMR-based SHOs is discussed in Chapter 4. MTJs are believed to be radiation hard and could be a part of the electronic applications in severe environments, such as in the space. We focus on the study of ionizing radiation effect on MTJs in Chapter 5 for a proof. Topological insulators (TIs) have been mentioned in such a high frequency because of its fascinating quantum-based property in Physics. In Chapter 6, we study the electrical detection of spin momentum locking (SML) effect of topological surface state (TSS) in single crystal 3D TI nanowires.

Chapter 2

Background

2.1 Magnetoresistance

2.1.1 Giant Magnetoresistance (GMR)

In spintronics, Magnetoresistance (MR) is a very frequently mentioned word. Simply speaking, MR is the change in electrical resistance due to the change of magnetization amplitude and orientation. There are many different types of MR, and one of the most important ones is GMR. The discovery of GMR is initially in antiferromagnetic coupled Fe/Cr superlattices system which Grunberg and Fert studied and won for the Nobel Prize in 2007.[1, 5] In this system, the Cr layer thickness is controlled such that the interlayer exchange coupling of the Fe layers is antiferromagnetic.(Figure 2.1) At zero applied external magnetic field, the magnetization alignment is anti-parallel (AP). After applying sufficiently strong in-plane magnetic field, the AP alignment was changed to a parallel (P) magnetization that yields a change in resistance of around 45 % at room temperature.

Now, of course, it is known that the antiferromagnetic coupling is not completely necessary

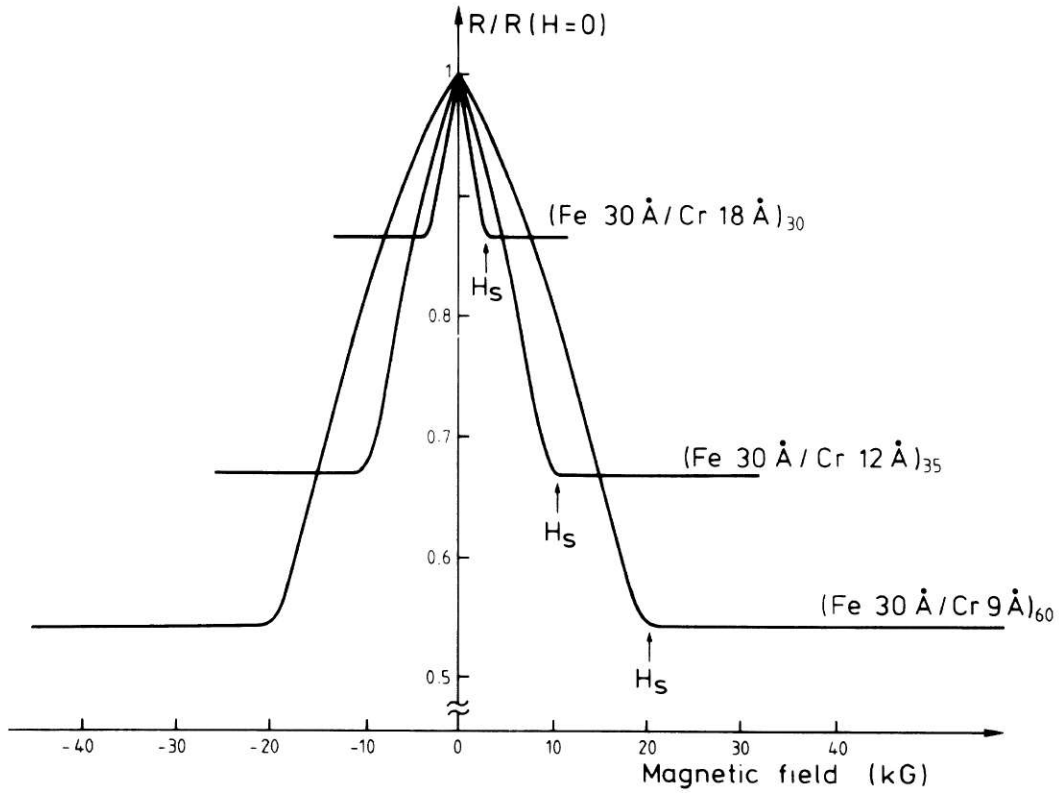


Figure 2.1: GMR effect in Fe/Cr superlattices. (Adapted from [1])

for the GMR effect. More generally, GMR is the dependence of electrical resistance on the angles between the magnetization orientations of two ferromagnetic layers which are separated by a non-magnetic metal (NM) layer. The resistance is low for parallel (P) alignment, and high for anti-parallel (AP) alignment in collinear magnetization geometry. This concept has triggered the studies on a simply trilayer structure, or named metallic spin valve structure, and has been applied widely in magnetic memories and sensors.

The GMR effect can be explained by spin-dependent electron scattering mechanism. Ideally, we can assume that at the interface the scattering rate depends on the electrons spin orientation with respect to the local magnetization. So in the top graphs of Figure 2.2, it is assumed that only electrons with opposite spin orientation related to FM layer are scat-

tered. This yields an increase of total number of scattering events, so increases the electrical resistance. ($R_2 > R_1$) The Mott two-current model for the electrical conductivity in metals can be introduced here to understand the GMR effect.[9] The bottom graphs of Figure 2.2 shows the two-current channel model of trilayer structure correspond to the top graph. If the Mean free path for both spin directions is much larger than the layer thickness. We can represent the resistances of same-spin and opposite-spin channel as R_1 and R_2 . So the resistances for the P and AP cases are $R_p = 2R_1R_2/(R_1 + R_2)$ and $R_{ap} = (R_1 + R_2)/2$. The GMR ratio can be expressed as

$$\begin{aligned} GMR &= \frac{R_{ap} - R_p}{R_p} \\ &= \frac{(R_1 - R_2)^2}{4R_1R_2} \end{aligned} \tag{2.1}$$

For most of the general systems, $R_1, R_2 > 0$. It follows that $R_{ap} > R_p$, so the GMR ratio is positive.

So far we have considered that GMR arises from P and AP magnetization of the successive FM layers. Here we need to discuss the variance of magnetoresistances when the magnetization alignments of two FM layers are in between P and AP states. Dieny et. al. had performed an experiment[10] that rotated the external magnetic field and measured the magnetoresistance of the metallic spin valves. (A spin valve consists of a fixed FM layer, a NM layer, and a free FM layer) They found that GMR varies linearly with $\cos(\theta)$, and can be described by the formula

$$R(\theta) = R_p + (R_{ap} - R_p) * \frac{1 - \cos(\theta)}{2} \tag{2.2}$$

where R_p and R_{ap} are the resistances of the spin valve for the P and AP states respectively.

θ is the angle between the two magnetization. This functional angular dependence of GMR is also confirmed by the theoretical calculation via free-electron model and first principle calculation.

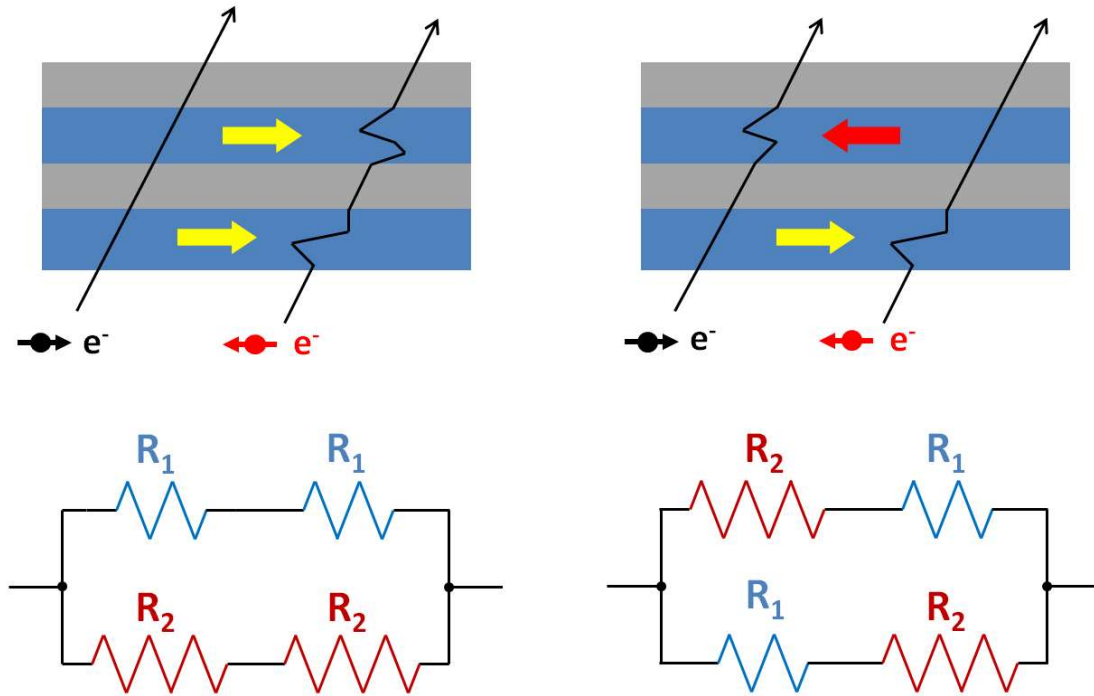


Figure 2.2: **Top:** The schematic drawings of two spin polarity electrons going through FM/NM/FM multilayers. The left graph shows parallel (P) state of two FM layers. The electron with the same spin orientation as the FM layers pass through this multilayer straightly while the electron with opposite spin orientation is largely scattered when passing through FM layer. The right graph shows anti-parallel (AP) state. Both electrons go straight through in one layer and scatter in another layer. **Bottom:** The Mott two-current model of P and AP states of FM/NM/FM structure correspond to the tops. The same-spin and opposite-spin channel is represented as R_1 and R_2 .

2.1.2 Tunneling Magnetoresistance (TMR)

The tunneling magnetoresistance (TMR) occurs in a similar structure as GMR by replacing the nonmagnetic metallic interlayer with an ultra thin insulating material, such as Al_2O_3 and MgO . For these FM/I/FM hetero-structures, the transport property is strongly dependent on the tunneling probabilities of spin carriers between the two FM layers. The first explanation of TMR is published by Julliere [6] and it is schematically depicted in Figure 2.3. In this model, the tunneling conductance of P and AP states are proportional to

$$G_p \propto n \cdot n' + (1 - n) \cdot (1 - n') \quad G_{ap} \propto n \cdot (1 - n) + n' \cdot (1 - n') \quad (2.3)$$

where n and n' are the fractions of tunneling electrons in FM1 and FM2 respectively whose magnetic moments are parallel to the magnetization. The conduction electron polarizations of FM1 and FM2 can be derived as $P_1 = 2n - 1$ and $P_2 = 2n' - 1$. Now the calculation of TMR is given by

$$\begin{aligned} TMR &= \frac{R_{ap} - R_p}{R_p} = \frac{G_p - G_{ap}}{G_{ap}} \\ &= \frac{2P_1P_2}{1 - P_1P_2} \end{aligned} \quad (2.4)$$

This well-known TMR expression derived by Julliere model serves as a starting point for analyzing MTJs. However, in Julliere model, the tunneling electrons only depends on the two FM layers and have no distinctions between the different types of electrons. (e.g. s-band electrons and d-band electrons) The electrons tunneling rates are assumed to be equal and do not depend on the properties of the tunneling barrier at all. It was failed for the case

of MgO-based MTJs, in which the observed TMR values were found to far exceed those predicted by the Julliere model.[7, 8] By replacing the MgO tunnel barrier with the Al₂O₃ barrier, the TMR values can reach as high as 410 %.[11] The main difference comes from the structure of these two materials. The Al₂O₃ tunnel barrier is polycrystalline while the MgO is single-crystalline or highly textured along (001) direction. This single crystal nature of MgO, combined with some special properties of FMs (Co, Fe, CoFe, CoFeB) leads to an enhancement of spin polarization for the tunneling electrons due to the Δ_1 spin filtering. Such large changes in TMR combined with advances in nanofabrication process has made the MgO-based MTJs a promising candidate for next generation non-volatile memory and drained a lot of attention to the studies.

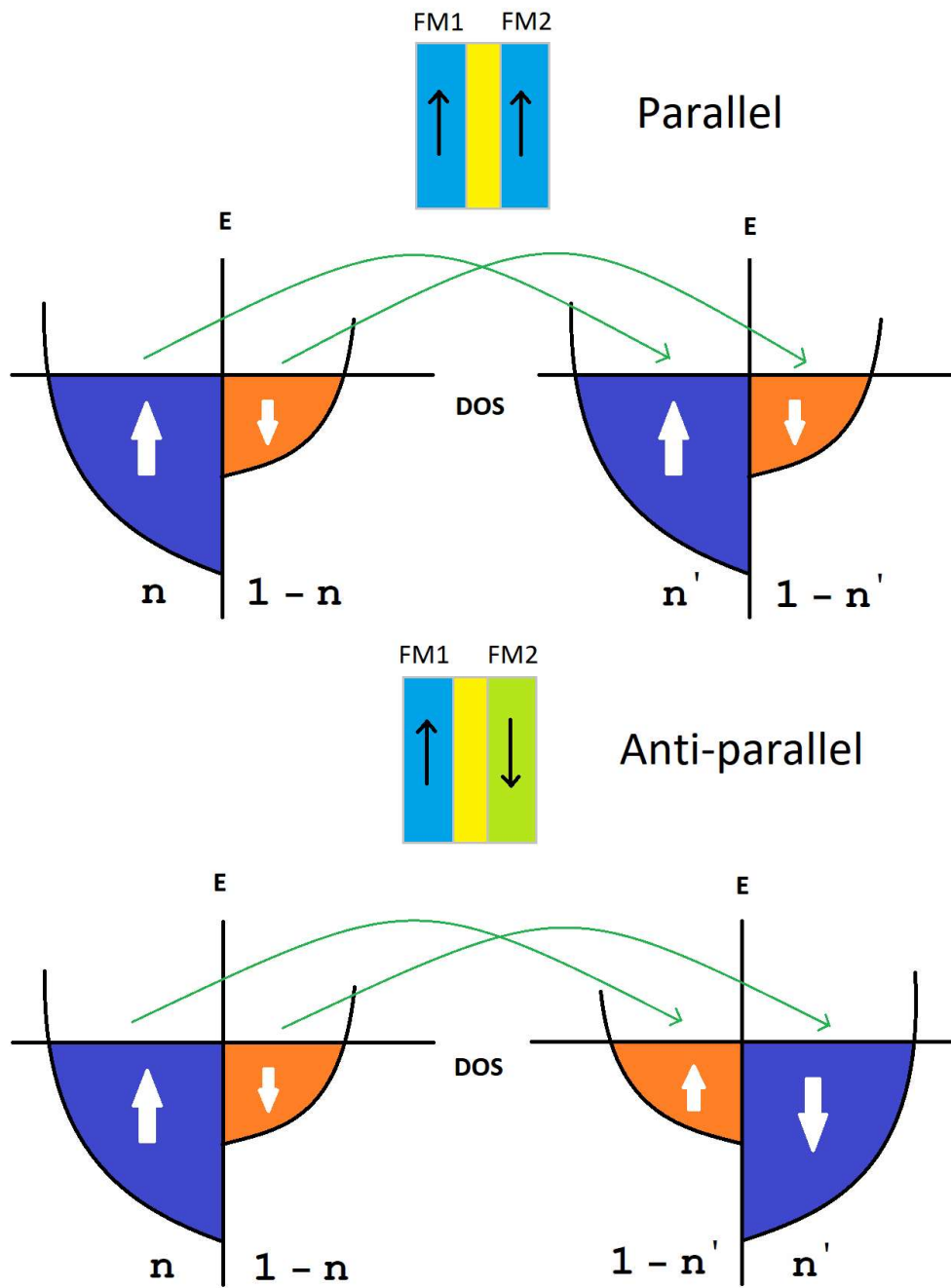


Figure 2.3: Julliere model for tunneling magnetoresistance.

2.2 Lateral Spin Transport Devices

While people have gained much of the technological successes of spintronics in multilayered structures, there is significant interest in developing lateral spintronic devices. In a lateral geometry, multiterminal devices are fabricated and the manipulation of spin via electrostatic gating becomes possible. An example of such a device was first proposed by Datta and Das in 1990.[12] A spin-based transistor, in which spin injected from the FM contact, transited in non-magnetic channel, and then detected in another FM contact. The schematic is shown in Figure 2.4. However, for this type of lateral spin devices, there are new challenges which must be overcome. Primarily, spins must remain polarized in the channel for longer distances in lateral devices as compared to the multilayered devices. Therefore, alternative materials that possess long spin diffusion property or special hetero-structures that create a channel suppress the spin scattering of carriers are desirable.

2.2.1 Non-local Measurements and Spin Diffusion

A sensitive way of measurement of spin injection is the so-called non-local geometry [cite], which is employed to identify spin injection and spin diffusion in lateral structures. (See Figure 2.4.) In this type of measurements, there is no current flow between the two FM electrodes. After the spins are injected from FM1 into the non-magnetic channel, the electrons are directed away from the FM2 due to the applied electric field. However, the spin polarization will diffuse and make its way to FM2 even though there is no electrical current between FM1 and FM2.

The idea of spin diffusion is like the diffusion of gas particles. For a standard electron diffusion, electrons in the left region diffuse to the right region while electrons in the right region diffuse to the left. The left and right regions are just exchange electrons, so there is no

net current between two regions. If the electrons in the left region are 100 % spin up polarized and electrons in the right region are unpolarized (50 % spin up and 50 % spin down). While the 100 % polarized electrons in the left region diffuse to the right, and the unpolarized right electrons diffuse to the left. This generate a net spin current without a net charge current in between the two regions. In the non-local measurement, spins diffuse from FM1 through NM channel to FM2. This spin-polarization produce a spin-dependent chemical potential under the FM2 electrode. When the non-local voltage is measured between the FM2 and a position far away on the NM, the voltage is asymmetrical to this spin-dependent chemical potential, depending on the relative orientation between the magnetization of FM2 and the direction of spin-polarization that diffuse to the FM2. (in the NM and under the FM2) For this non-local detection method, ideally there is no background level, which means it could greatly improve the signal-to-noise ratio and provide more sensitive spin detection.

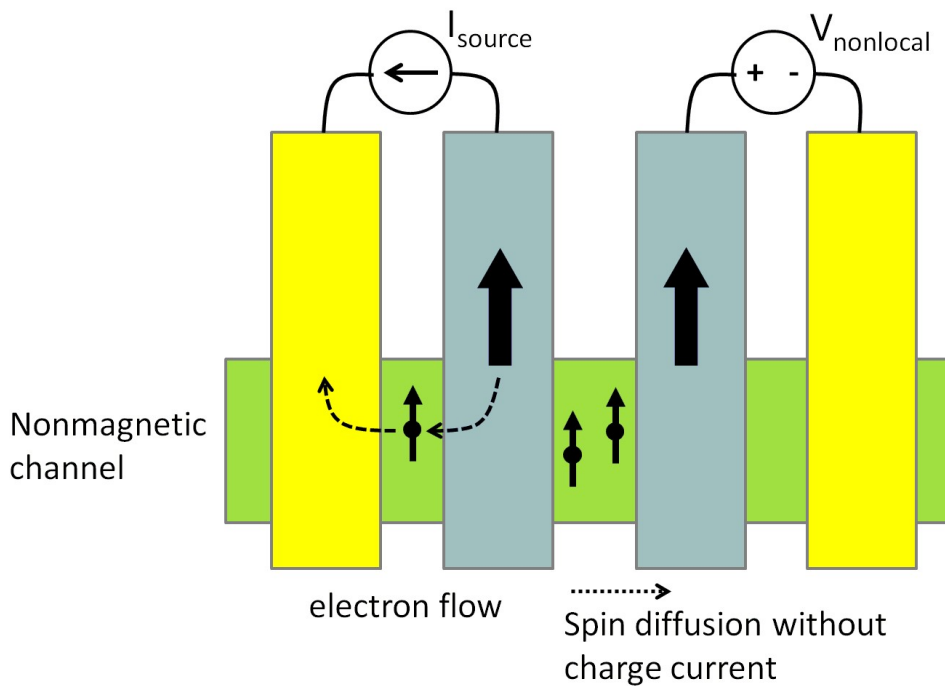


Figure 2.4: Lateral spin valves in a non-local measurement geometry, with schematic for the geometry.

2.2.2 Spin Injection and Detection

Spin injection from a ferromagnet into a non-magnetic material is a key for nonlocal measurements. Figure 2.5 shows the junction between a ferromagnetic metal and a non-magnetic metal. The spin-related transport properties within the FM and NM magnetic layers are best described by the spin-dependent chemical potentials ($\mu_{FM,\uparrow,\downarrow}, \mu_{NM,\uparrow,\downarrow}$) and average chemical potential ($\mu_{FM} = \frac{1}{2}(\mu_{FM,\uparrow} + \mu_{FM,\downarrow})$). Under a bias current, the polarized current generates a spin-dependent average chemical potential at the interface. This average chemical potential is discontinuous at the interface due to an intrinsic difference in the spin chemical potentials between the two materials. The amplitude of this potential drop, often called spin accumulation, at the interface depends on the properties of two different spin conduction channels and two materials with different electrical conductivities. Across the interface, the spin-dependent chemical potentials decay exponentially within the non-magnetic layer. This exponential decay corresponds to a characteristic length-scale, spin diffusion length ($\lambda_{sf} = \sqrt{D\tau_s}$). D is the diffusion constant of the respective materials and τ_s is the spin lifetime, which is characteristic time the spin population relaxes. It is fundamental to understand the nature of spin-relaxation in different materials in order to realize spin-dependent transport behaviors.

In four terminal nonlocal measurements, current is injected through one of the ferromagnetic electrodes and flows to the left and voltage is detected from another FM electrode to the right. Underneath the FM contact, the picture for spin injection and accumulation is comparable to the one discussed previously. In non-magnetic metal channel, there is a positional dependence of the spin-dependent chemical potential. The pure spins diffuse in the NM channel to the right is corresponded to the decay behavior of spin-dependent chemical potential. ($\mu_{\uparrow,\downarrow} \propto e^{-x/\lambda_{sf}}$) If the spins remain polarized in NM channel, by employing a right FM contact not too far away (L/λ_{sf} is not too large), the voltage measurement detects the spin-dependent chemical potential depending on the relative orientation of the dominant spins' polarized

direction and the magnetization direction of the right FM electrode.

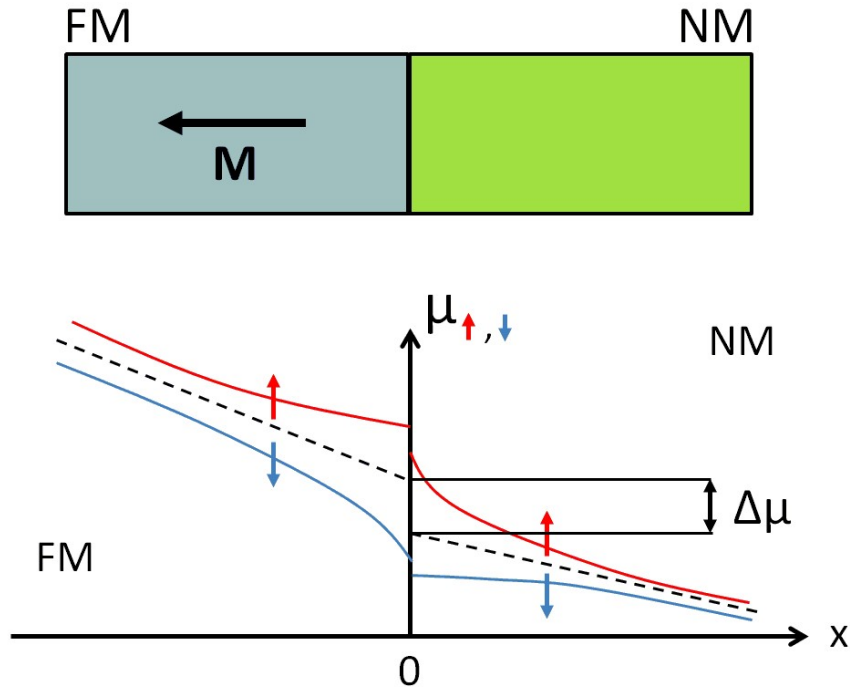


Figure 2.5: Spin Injection at FM/NM Interface. **Top:** Schematic of the interface between a ferromagnetic metal (FM) and a non-magnetic metal (NM). **Bottom:** Adapted from [2]. Spin-dependent chemical potentials as a function of position at the interface of FM and NM materials.

2.3 Spin Hall Effect

It was proposed that when an electrical current circulates in a paramagnetic metal should lead to a transverse spin current in the system, called Spin Hall Effect (SHE). [13–15] The SHE originates from the spin-orbit interaction in metals and semiconductors. When an electron flow through a non-magnetic metal and encounter a local potential due to the large spin-orbit coupling of existing impurities or defects, the local potential causes a spin-asymmetry

scattering of the electron. The electron will acquire a transverse velocity depends on the spin orientation. Figure 2.6 shows the schematic graph of the SHE. In this simple explanation, the red arrows are spin up electrons and the green ones represent spin down electrons, and the spin imbalance leads to the spin accumulation in both edges, i.e. $y = 0$ and $y = L$. SHE can be separated to intrinsic SHE and extrinsic SHE according to its mechanisms. The difference between the intrinsic and extrinsic SHE is similar to the mechanisms of spin relaxation. For intrinsic SHE, the electrons are affected by local potentials and acquire a transverse velocity in between the scattering events. While a transverse velocity or displacement is generated by electrons during the scattering event are referred to as extrinsic SHE. The impurity concentration is essential for SHE in normal metal systems. Due to the different dependence of Spin Hall conductivity to the different mechanisms of SHE, both intrinsic and extrinsic SHE can contribute to the SHE in different metal systems. As a consequence, charge current in a normal metal system can be converted to pure spin current, which could be applied in all kinds of spintronic systems. The efficiency of converting charge current to spin current depends on the quality and the elements of metals. In general, heavy metals (HMs) have an averaged higher Spin Hall angle due to stronger spin-orbit coupling. So here we use the HM, platinum (Pt), which has a good conductivity and high spin Hall angle, to combine with FM multilayer for the study of spin Hall oscillator system.[15]

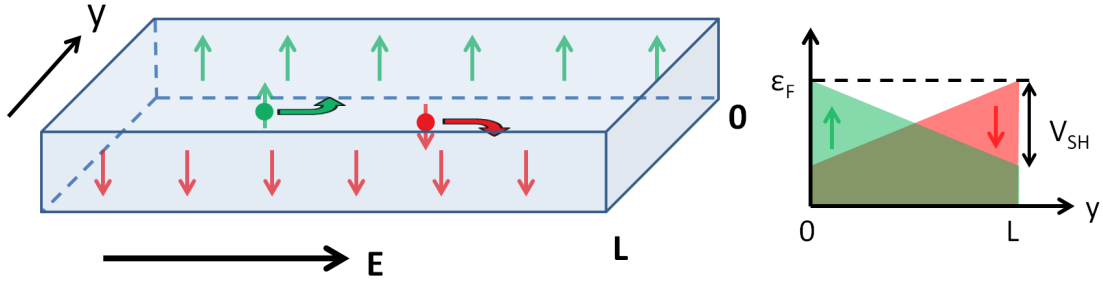


Figure 2.6: The schematic of spin Hall effect (SHE). The spin-up (green) and spin-down (red) charge carriers are deflected perpendicular from its original trajectories and imbalance accumulated to the two edges $y = 0$ and $y = L$. The right graph shows that the electric voltages at two edges are the same, V_{SH} , however spin dependent chemical potential differently.

2.4 Magnetization Dynamics

2.4.1 Spin Transfer Torque (STT)

In 1996, the effect of spin transfer torque (STT) in a magnetic multilayer system had been predicted by Slonczewski [16], which suggests that the flow of spin polarized electric current can excite the magnetic states of ferromagnets (FMs) due to exchange interactions. We can use a simple schematic example to understand STT, shown in Figure 2.7.

When a conduction current is applied through a magnetic multilayer, it is polarized by first FM layer (FM1) and transported to the second FM layer (FM2). If the spin polarized current is differ from the direction of local magnetic moments in the FM2 layer, they exert torques onto each other and cause deflections from their original directions. This torque is called spin transfer torque, τ_{st} denotes by black arrow in the right graph. The local magnetic moment in FM2 is express by the blue arrow, \vec{m} . The polarization of electron current is denotes by red arrow, \vec{p} . For conduction current, it carries the spin information of the local moments and interact with other magnetic moments after passing the FM2 layer. For the local magnetic

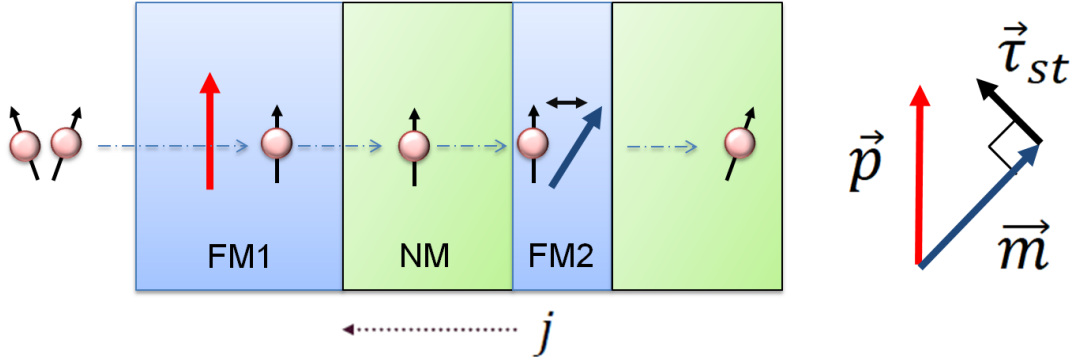


Figure 2.7: A example schematic shows spin transfer torques (STTs). The random spin electron current is polarized when pass through the FM1. This spin polarized current is transferred to FM2 and exert torque to local magnetic moment due to exchange interaction. After interaction, both magnetization in FM2 and transferred carriers change its spin orientations.

moment in the FM2, it could have three possible results. First, if the STT torque is too small and not continuously applied on the local moment, the magnetization will differ from its original direction and relax back to its local minimum. Second, if the STT happens to be the cancellation of the magnetic damping torque of the magnetization, the local moments could stay deviated from its local minimum and start the precession motion. Finally, if the STT is overwhelming the damping of the system, it could cause the switching of the local moments to another local minimum. These results are schematically shown in Figure 2.8. [3]

Here, I describe this STT behaviors with some assumptions and intrinsic properties of the system. For example, a system can have just one or two local minimums, it depends on geometry, material property, composition, and an external applied field of a system. So let's introduced the Landau-Lifshitz-Gilbert (LLG) equation [17, 18] to describe the equation of motion of single magnetic moment (with magnetization \vec{m}) in a multilayer metallic spin valve

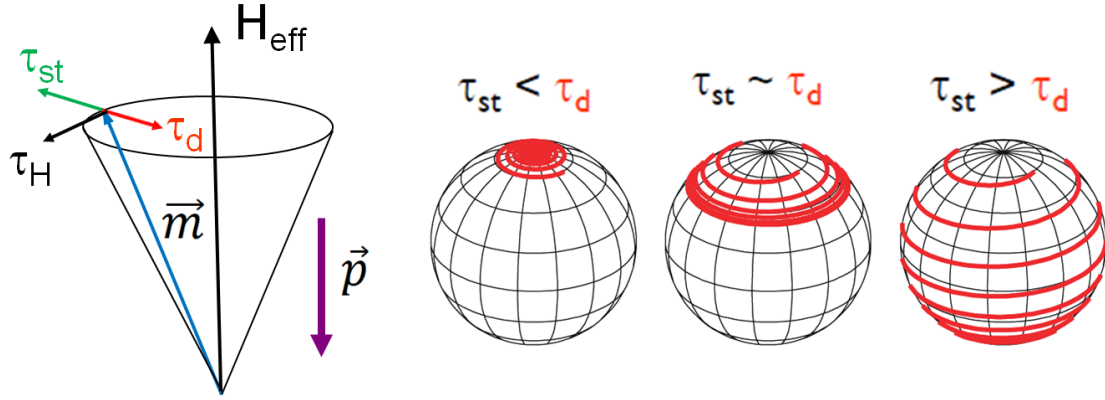


Figure 2.8: Illustration of the affection of spin transfer torque (STT) that leads to different motions of magnetic moment. If $\tau_{st} < \tau_d$, the magnetic moment relax back to its equilibrium. If $\tau_{st} \approx \tau_d$, the magnetic moment moves along a stable trajectory and self-oscillates. If $\tau_{st} > \tau_d$, the magnetic moment could oscillates in a larger and larger trajectory and eventually switches to another equilibrium position. [3]

system.

$$\begin{aligned}
 \frac{d\vec{m}}{dt} &= -\gamma\vec{m} \times \vec{H}_{eff} + \frac{\alpha}{|\vec{m}|}\vec{m} \times \frac{d\vec{m}}{dt} + \eta\frac{\mu_B I}{eV}\vec{m} \times (\vec{p} \times \vec{m}) \\
 &= \tau_H + \tau_d + \tau_{st}
 \end{aligned}
 \tag{2.5}$$

The first term of this equation is field like torque which usually is small and can be ignored mostly in this metallic spin valve system. The second term is damping like torque, in which α is the Gilbert damping parameter. [18] This torque tends to pull the magnetization toward its equilibrium position. The third term is the STT. As we mentioned in this section STT can excite dynamics of magnetization once STT is comparable to damping like torque of a system. The continuous precession motion of a magnetic moment is usually a GHz auto-oscillations which will be further discussed in next section.

2.4.2 Spin Torque Oscillator (STO) and Spin Hall Oscillator (SHO)

Spin torque oscillator (STO) is a special nanoscale magnetic device in which its magnetization is excited and auto-oscillated when the damping torques are compensated by the spin transfer torques (STTs). The conventional STOs are widely understood in current perpendicular-to-plane (CPP) metallic spin valves and magnetic tunnel junctions (MTJs). The oscillation of magnetization in these system is basically the change of MR (GMR or TMR), thus the auto-oscillation can be detected electrically as a microwave voltage. Another new type of STOs, called Spin Hall oscillator (SHO), is also introduced here. Since we know that the excitation of oscillation is induced by spin carriers which exchange interact with the local moment, it doesn't matter that the spin current come from a polarized current or other ways. We have learned that spin Hall effect (SHE) in a heavy metal (HM) layer can create pure spin current transverse to bias current direction. So SHOs which rely on SHE induced spin current to excite self oscillations are studied by combining the HM layer to FM layer or magnetic multilayer.

2.5 Topological Insulator

Topological insulators (TI) are materials with special quantum states that have a insulating in the bulk, but have a protected conducting (gapless) states on their edge or surface. These states are exist due to the spin-orbit interactions and time-reversal symmetry. The systems of TIs can be separated to two categories, 2 dimensional (2D) TIs and 3 dimensional (3D) TIs. 2D TIs, also called Quantum spin Hall insulators, was firstly experimentally observed in HgTe/CdTe quantum wells (QWs) system in 2007.[19, 20] In this system, the normal insulating state is shown when the thickness of QW is less than the critical value. However, when the thickness of QW exceeds the critical value, the topological nontrivial state is obtained. In this topological state, it's edge states carry unidirectional spin current and

leads to a quantized conductance, $2e^2/h$, associated with the edge states. The 3D TIs were predicted in $\text{Bi}_{1-x}\text{Sb}_x$, Bi_2Se_3 , Bi_2Te_3 , and Sb_2Te_3 compounds with a large bulk band gap and a gapless surface state consisting of single Dirac cone.[21–24] The numerous desirable properties were identified experimentally and theoretically in these materials. Next, the properties of TI surface states will be discussed in more detail.

2.5.1 Topological Surface States

A couple of striking properties of topological surface states(TSS) have been identified in 3D TI materials. For example, the electrical conducting behaviors in bulk are semiconductors for these 3D TIs. However, unlike the semiconducting materials,3D TIs behave like metallic states at cryogenic temperature due to the existence of Dirac cone at Fermi level. Moreover, while applying perpendicular magnetic field, the magneto-transport property shows the weak anti-localization effect, lower resistivity at zero field, and indicates the lack of electron back-scattering of the time reversal protected TSS. The most important property of TSS is spin-momentum locking (SML). Figure 2.9 demonstrates the SML. The spin of the TI Dirac surface state lies in-plane, and is locked at right angles to the carrier momentum. So an unpolarized charge current creates a net spin polarization. This remarkable spin-dependent property creates a direct electrical access to the TSS of TIs and enables a great application in spintronics.

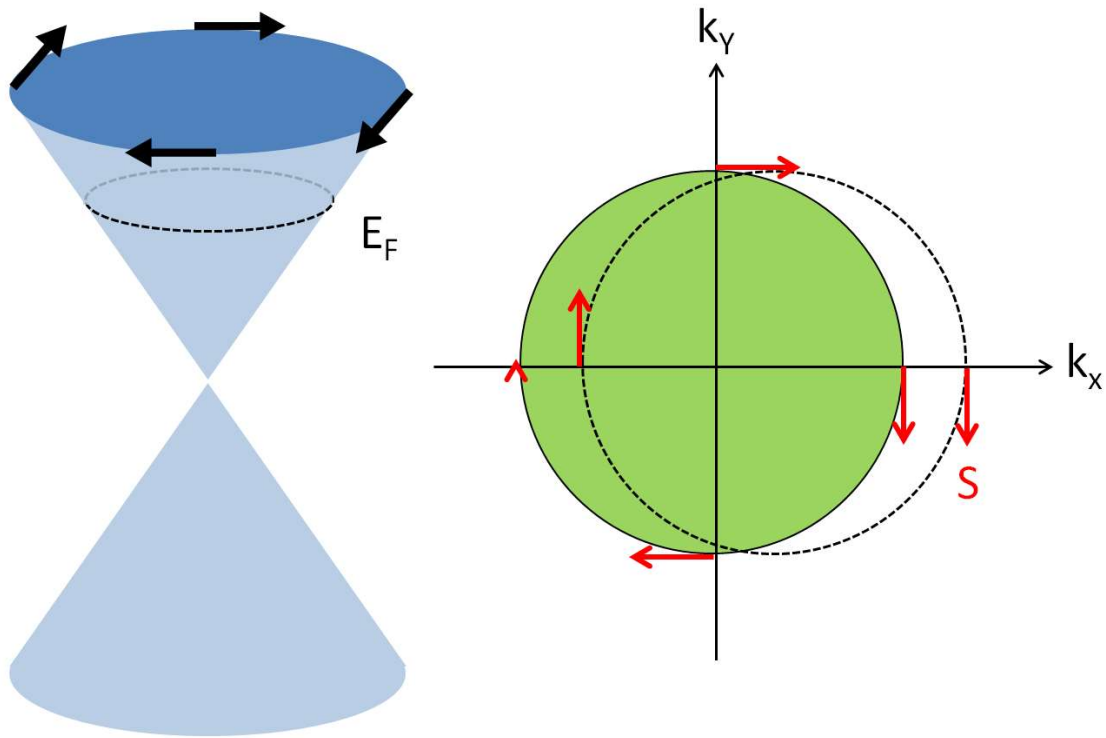


Figure 2.9: **Left:** Dirac cone of the TI surface states, with the spin at right angles to the momentum at each point. **Right:** Top view of the $k_x - k_y$ plane of the TI surface states. An applied voltage produces a net momentum along k_x and spin-momentum locking gives rise to a net spin polarization oriented in-plane and at right angles to the current.

Chapter 3

Experimental Details

3.1 Nano-Fabrications Instruments and Methods

3.1.1 Sputtering Deposition

Sputtering deposition uses argon plasma to eject small amount of source material then deposit onto a surface (substrate) while placing substrate in the trajectory of ejected material. Conductive material can be deposited by using DC power supply and insulator material can be deposited by using RF power source. The reason why the RF (13.56 MHz) power source is used is to accelerate argon plasma and get rid of the accumulated charges on the insulating target surface. The sputtering deposition is usually performed in an ultra high vacuum(UHV) chamber. By using the magnetic field to confine charged particles (Ar plasma), it enhances both the efficiency of the initial ionization process and also allows plasma to be generated at lower pressures which can reduce the deposition rate of materials. This is named as magnetron sputtering. The Base pressure of the sputtering deposition system in our lab can reach 5×10^{-9} torr. The few-nanometer thin films with uniformity close to the substrate can

be deposited by flowing low pressure argon gas into the chamber and modifying power levels. For our system, the deposition rate is quite stable for a given power. The precise values can be extracted out by measuring the thickness of thin films. Figure 3.1 is the schematic and a picture of sputtering deposition system.

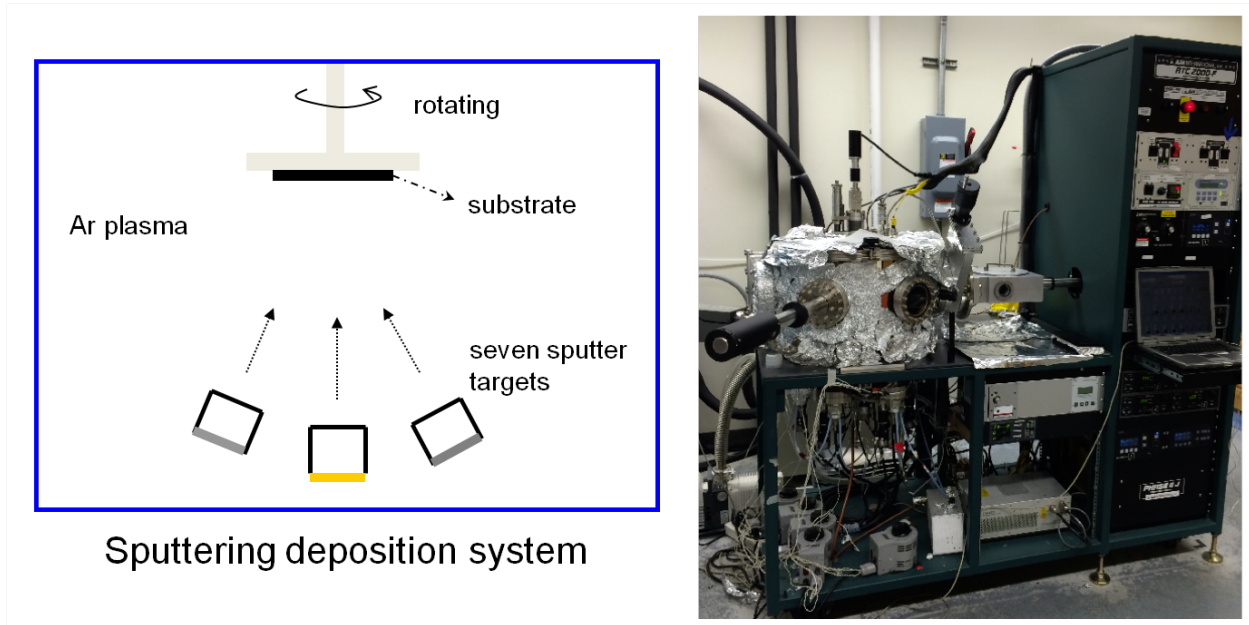


Figure 3.1: **Left:** The mechanism of sputtering deposition system. **Right:** The pictures of AJA magnetron sputtering system in the Lab.

3.1.2 Electron Beam Evaporation

Here, we introduce another way to deposit multilayer thin films, electron beam evaporation (E-beam evaporation). Unlike sputtering deposition that we use for growing couples of nanometer materials. The E-beam evaporation can be used for depositing tens of nanometer to microns of materials. E-beam evaporation is a form of physical vapor deposition. Basically, an intense electron beam is generated from a high voltage charged filament and accelerated via electric and magnetic field to a target material. The kinetic energy of electrons is transferred to the target material, which vaporized the material in a high vacuum chamber. This vapor can be used to coat a substrate positioned above the evaporating material. The E-beam evaporation was used to deposit alignment marks and contact leads on the device structures. The material combinations can be Ti/Au, Cr/Au, or Al/Au. The first layer (Ti, Cr, Al) is the adhesion layer with the thickness from 5 to 10 nm. The gold layer, with the thickness from 30 to 60 nm usually, offers a good contact for electrical conducted measurement.

3.1.3 Scanning Electron Microscopy and Electron Beam Lithography

A scanning electron microscopy (SEM) uses focused electron beam to scan sample's surfaces to create an image. The electrons interact with solid samples and generate signals which include information of sample's surface topography and chemical compositions. The most command signal that reveal sample's surface image is secondary electrons. The high energy electron beam interacts with the atoms of sample surface and excite the energy states of atoms. Then, the lower energy electrons are emitted by these atoms when the atoms fall back to their ground states. These emitted electrons are called secondary electrons which are detected and compose a 2-dimensional image. Figure 3.2 is an example of SEM image

of a Sb_2Te_3 nanoribbon. One of the most important applications of SEM is electron beam lithography (EBL), which uses focused electron beam to write a pattern on a thin-layer of E-beam resist. Depends on the types of resists, the pattern or mask can be developed. This resist-composed pattern or mask structure could be used for deposit materials onto it. Then, after a lift-off procedure to remove the resist, a pattern of desired materials shows up on the substrate. This technique can create nanoscale devices for different desired measurements and applications.

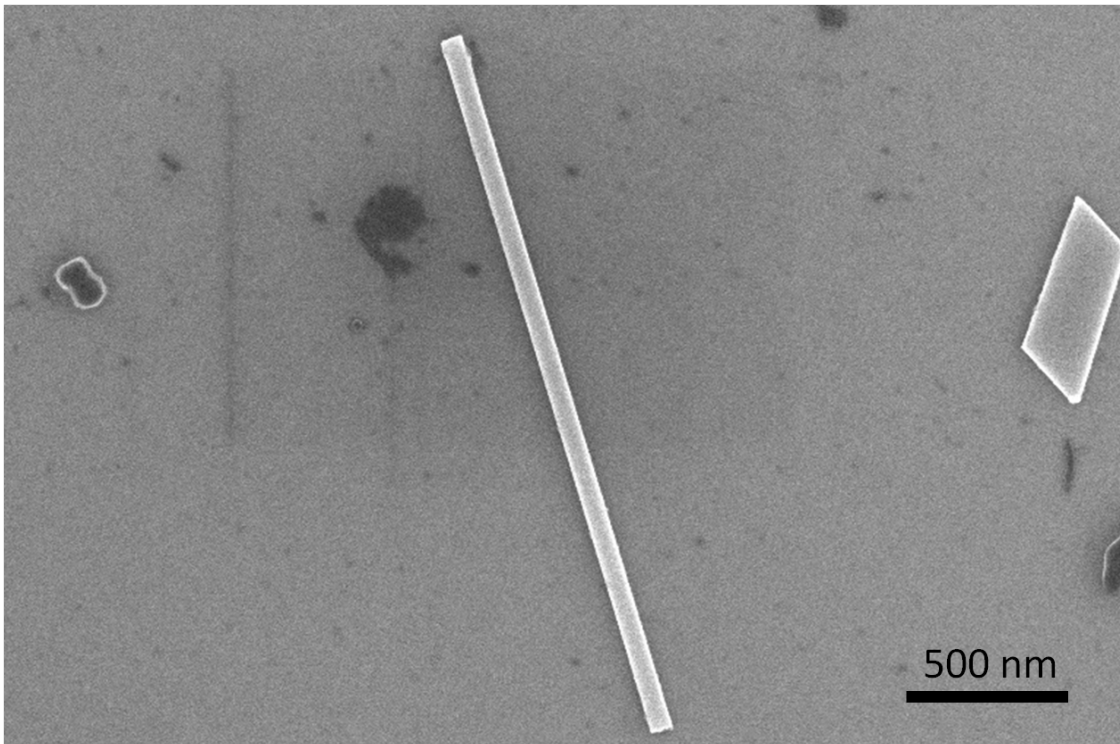


Figure 3.2: The SEM image of a Sb_2Te_3 nanoribbon. The scale bar is 500 nm.

3.1.4 Ion Miller Etching

In general, etching process is an essential procedure for micro- or nano-fabricated devices. Usually it can be categorized to two groups, wet etch or dry etch. Depends on the materials and structures, we can choose the most efficient and reliable methods to perform etching process. The dry ion beam milling used to be the good way for etching of nano-sized structure

due to the repeatability and precision. In general, the ion milling can simply be pictured as an atomic sand blaster by using accelerated Argon ions to bombard the target surface. Due to the rotation of the sample stage and the changeable stage angles, the ion milling etching process can create clean and straight side walls of samples. This method is beneficial to determine the nanowire geometry in our study.

3.1.5 In-Filed Oven Annealing

Setting up the reference ferromagnetic layer orientation is needed for the GMR spin-valve structure devices. Usually, there are two ways to determine the reference layer orientation of the spin-valve structure we focused on above. We can do the deposition with a magnetic field applied during the process or do the post annealing in a magnetic field. Here, we perform the post annealing in a special sample holder with strong permanent magnets to apply the magnetic field. The annealing procedure is in a high power oven equipped with a pumping station. The oven chamber is capable to anneal at ambient temperature 300°C in 2.4×10^{-6} torr high vacuum environment.

3.2 Device Fabrication Procedures

3.2.1 Nanofabrication of GMR-based SHO Nanowire Devices

This section describes the fabrication recipe of GMR-based SHO nanowire devices in detail.

1. A clean sapphire substrate is directly placed on the holder and straight into the load-lock of the sputtering system for the deposition of multi-layers. The pressure is kept below 2×10^{-8} torr before the deposition. The multi-layer, IrMn (4 nm)/Co (2 nm)/Cu (4

nm)/Co (0.5 nm)/Py(3.5 nm)/Pt (5 nm), is deposited by the magnetron sputtering. The system as shown in Figure 3.1. Before all the layers, the sapphire is treated by a 60 second low power (40 W) Argon plasma cleaning.

2. The as grown multi-layer thin film is diced to small pieces of around 1.5×1.5 cm² in size. A 2 mm straight scratch is marked at the left and bottom corner of the sample. The scratch is a good reference point when exploring under the scanning electron microscope. Also, a scratch of the sample creates lots of particles and rugged topography under the microscope, which will be a feature for the focusing purpose of SEM.
3. The MMA/PMMA e-beam resist is spin-coated on the surface of the sample. The recipe for first MMA layer is set to 4000 rpm for spinning 45 seconds, and the thickness is around 100 nm. An 1.5 minute bake on the 150°C hotplate for the cure of the MMA layer. After the sample cool down to room temperature, the second PMMA layer is coated by 1800 rpm spinning for 1 minute. Then follows an 180°C baking for 1.5 min. The layer is also 100 nm thick. This procedure is prepared the sample for EBL patterning.
4. The goal of first EBL writing is to place the alignment marks on the sample. Figure 3.3 shows the pattern of alignment marks. The drawing is done in Layout and save the pattern to .gds file. The pattern writing program that integrate to SEM system is NPGS, which allows you to convert the .gds file to .dc2 file. The .dc2 file store the pattern in vectorized data that it can be used by NPGS to control and move the e-beam source to the desired position. The EBL procedure is done in FEI Magellan SEM system, the working distance is 7 mm. The dosage for writing the pattern should always be tested and calibrated based on the real current of e-beam and the sizes of pattern. For writing the alignment marks in this SEM system, I use 25 pA current, 300 $\mu\text{C}/\text{cm}^2$ dose, and 11 nm as center to center distance.

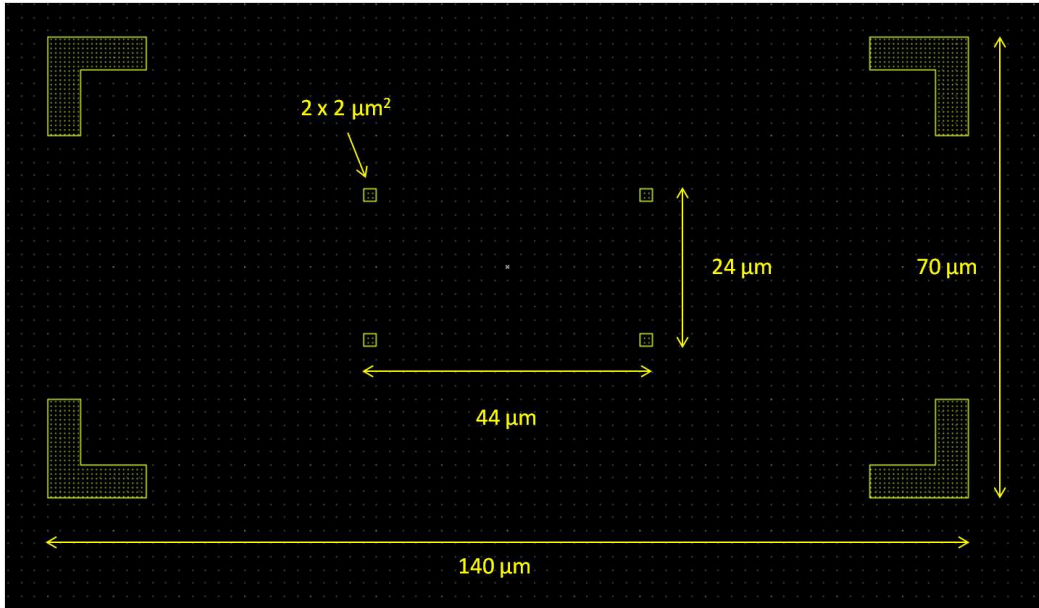


Figure 3.3: The drawing of an alignment mark used for milling defined nanowire devices.

5. After SEM writing the alignment marks on the resist, the sample is developed to expose the pattern. The sample is immersed in the MIBK/IPA solution for a minute. (MIBK:IPA = 1:3) Then, place the sample in IPA solution for another 30 seconds. Dry the sample with nitrogen gas.
6. Next, the metal is deposited on the sample to define alignment marks. The deposition is usually done in e-beam evaporator. However, it also can be done our sputtering system. In e-beam evaporator, 5 nm Ti layer is deposited first served as an adhesion layer. Then, 45 nm gold layer is deposited. In the sputtering chamber, Nb(5 nm)/Au (40 nm) is deposited usually. Al and Ta also can be used as adhesion layers.
7. Lift-off is done here fro removing the e-beam resist and leave the alignment marks on the sample surface. The sample is placed in acetone bath for an hour. Sometimes heat

up the acetone bath to 65°C could help lift-off more easily.

8. Now the sample with the alignment marks is spin-coated again to write the nanowire geometry. In this step, the negative resist or HSQ (or a negative resist) is used. We would like to have the shape of nanowires covered by the negative resist as the hard mask. Rest of parts will be etched down and leave the multi-layer nanowires. The negative resist is spin-coated on the sample by using 3600 rpm for 45 second. Follows by one minute bake on the hotplate at 90°C.
9. Here I choose 13 pA current for SEM writing. The nanowires are 50 to 200 nm wide and 50 μm long. The drawing of a nanowire is shown in Figure 3-4. The dosage ranges from 350 to 550 $\mu C/cm^2$. Since the alignment marks are already on the sample surface, this is the step that needs alignment marks. We need to align the e-beam to be exactly at the center of each alignment mark, then write a nanowire. Doing so we can make sure the electrodes can precisely contact to the nanowires in such a small scale.
10. Developing is done in MAD-525 solution for 90 seconds and cleaned in water.



Figure 3.4: The drawing of a nanowire geometry.

11. Now etch down the sample by ion milling etching. The etching rate is different for different metal layers. A full calibrations of etching rate for each layer need to done initially. Then, we can calculate the etching time for each layer roughly and do a one time calibration on the multilayer sample. A special process is done here by just etching down the multilayer to the bottom Pt layer. Here we use sapphire substrate, and it's non-conductive. When doing the EBL writing again on the next step, the

insulated surface will cause electron charges accumulate on the surface and distort the writing patterns.

12. Spin-coating MMA/PMMA resist layers again for contact electrodes EBL writing. Again, follows the alignments to make sure the electrode patterns are correctly written on the nanowires. In GMR-based SHO nanowire devices, two contacts and a close active region is fabricated. So the e-beam currents that used to write the inner small pattern and outside contact pads are different. Here is how I choose currents for writing different size of patterns. 25 pA is used to write rectangles within 10 μm , and 100 pA is used for 50 μm . Rectangles that larger than 50 μm are written by 800 pA or 1600 pA.
13. Developing the sample, then use e-beam evaporator or sputtering again to deposit the contact electrodes. Ti/Au or Nb/Au is used as well. Finally, lift-off the resist to expose the contact electrodes.
14. Image all the devices by SEM. Figure 3-5 is an example SEM image of a milled defined nanowire device.
15. Finally, use ion milling etching to etch down the bottom Pt layer to prevent shorting between the leads. A slightly over-etching is allowed in this step. A final completed device is shown in Figure 3-5, from center zoom out to whole device.

The cartoon drawings of nano-fabrication procedures of a multilayer nanowire device is shown in Figure 3.6.

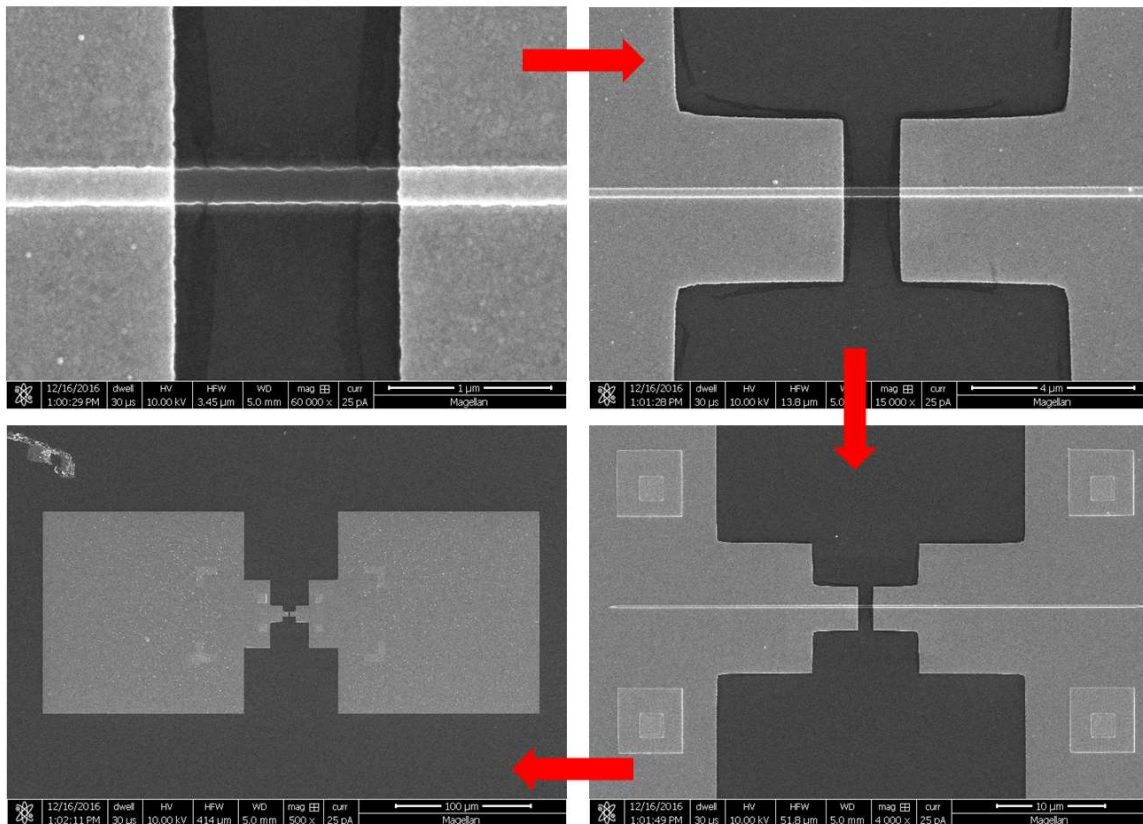


Figure 3.5: SEM images of a GMR-based SHO nanowire device. Top left: The 60,000x magnification image. Top right: The 15,000x magnification image. Bottom right: The 4000x magnification image. Bottom left: The 500x magnification image.

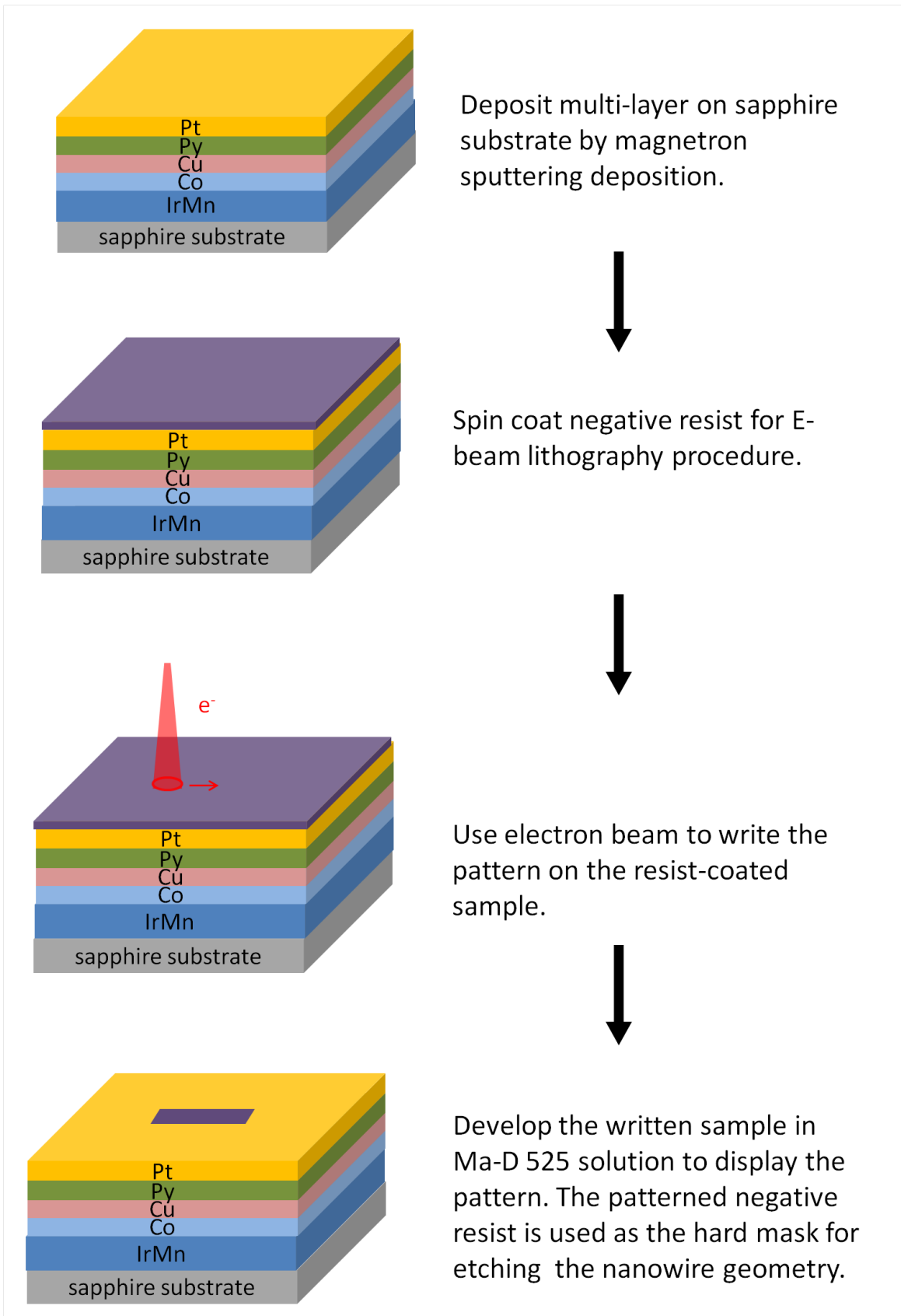


Figure 3.6: Nano-fabrication procedures.

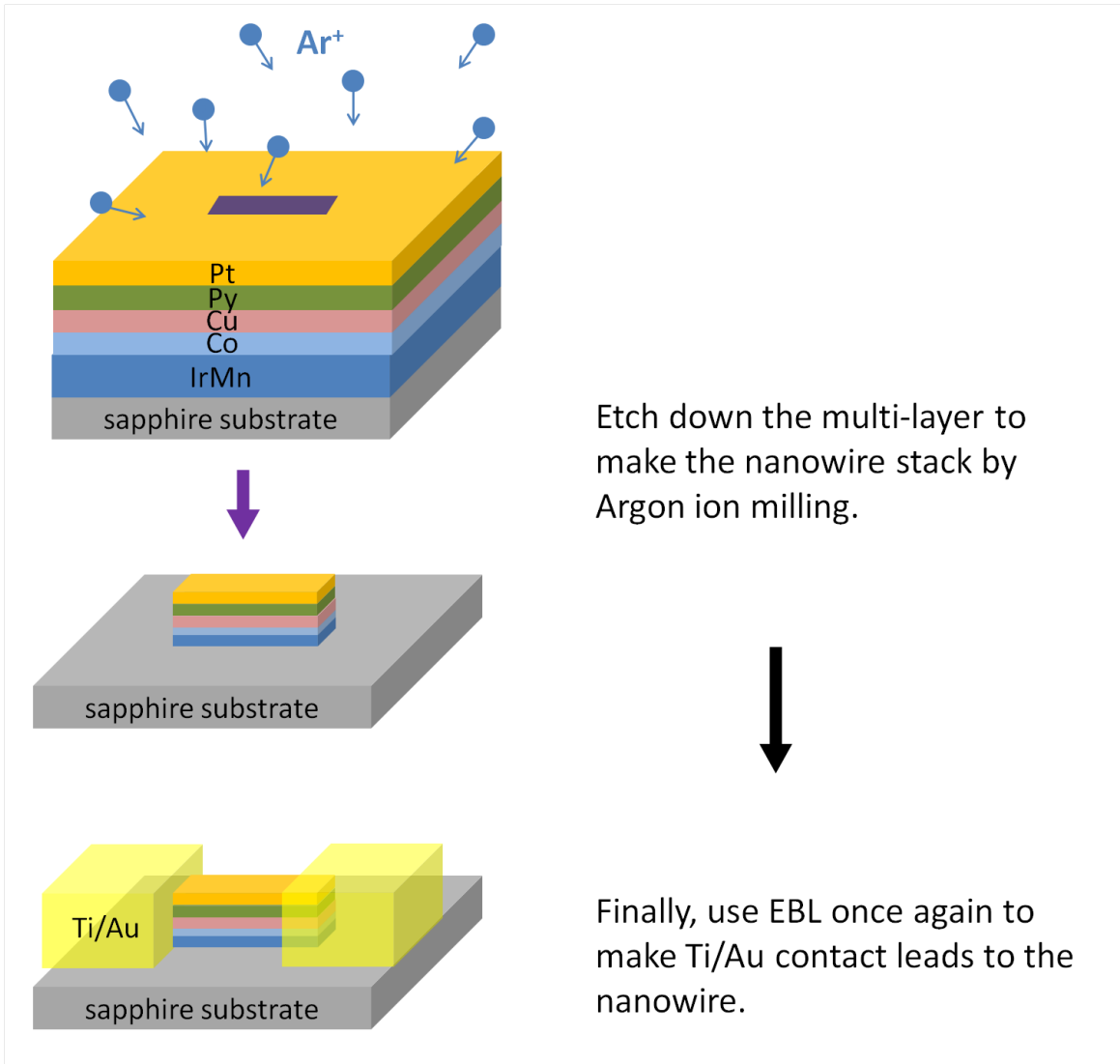


Figure 3.7: Nano-fabrication procedures.

3.2.2 Nanofabrication of Sb_2Te_3 Lateral Devices

In this section, the fabrication recipe of Sb_2Te_3 lateral devices is discussed in detail. Unlike the GMR-SHO devices that I described above, the Sb_2Te_3 nanowires are not defined by etching. The CVD grown Sb_2Te_3 nanowires are sonicated off from substrates and transferred in the IPA solution. Then, we drop-cast the dilute Sb_2Te_3 nanowire solution on the sapphire substrate to make devices. Sb_2Te_3 nanowires are randomly distributed on the substrate and in random orientations. Therefore, before we drop the Sb_2Te_3 on the substrate, the sapphire substrate need to be prepared to have the alignment marks on it.

1. A clean sapphire substrate is directly placed on the holder and straight into the load-lock of sputtering system for the deposition of a 3 nm Pt layer. This Pt layer is used as the conducting layer on the substrate for EBL.
2. The alignment marks is defined by EBL/deposition process as above. The design of the alignment marks for this process is shown in Figure 3-7. The small cross is $2 \times 2 \mu\text{m}$, and distance between the crosses is $50 \mu\text{m}$. One domain is defined with a number 2 at the left and bottom corner and domain size is $500 \mu\text{m}$. When writing the alignment marks, a 9×9 array of domains is written at the center of the substrate. So the total area that this type of alignment marks occupied is $4.5 \times 4.5 \text{ mm}^2$. It is we build a tiny visible coordinate plane on the substrate. Once a Sb_2Te_3 is found on the substrate, we can record it's coordinate.
3. Once the alignment marks is defined on the substrate, 3 nm Pt layer is removed by ion milling etching in order to avoid electrical shorts underneath Sb_2Te_3 nanowires. Then, Sb_2Te_3 nanowire solution is dropped on the substrate and naturally dried in the air. Couple drops are needed for reaching enough density. Microscope inspections are needed to make sure there are enough nanowires located in the alignment marks area. The sample is load into the sputtering system for deposition of a 3 nm Pt layer again.

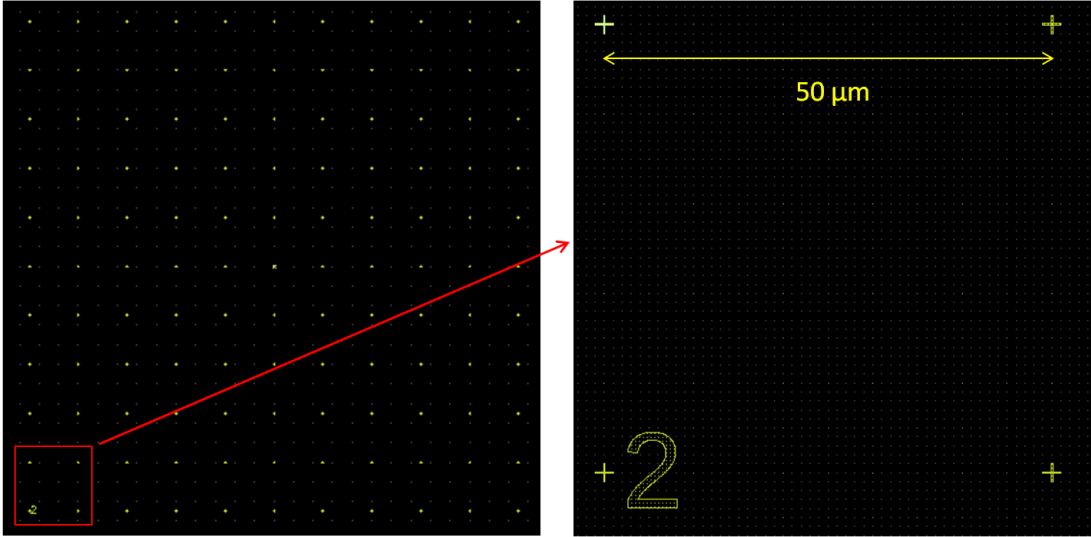


Figure 3.8: The drawings of an alignment mark used for random located nanowires.

This Pt layer is still needed for EBL steps and imaging purpose in SEM.

4. Looking for Sb_2Te_3 nanowires by SEM. The images of each nanowire are taken and it's coordinate is recorded. Here is the way I do for making these devices. Since there are 9×9 domains, the domain in the m th row, n th column is defined as $D_{m,n}$. In each domain, the number 2 is defined as $(0,0)$. If a Sb_2Te_3 nanowire is found near a cross at the center of a domain. Then, the coordinate of this nanowire is defined as $(250, 250)$. (unit in μm) For example, a nanowire is recorded at $D_{1,1}(100, 300)$. A SEM image with the nanowire and the most closet cross is taken in order to draw the contact patterns. A example image is shown in Figure 3-8. In order to wire bonding to a fabricated nanowire device, the size of outside contact pad is usually $100 \times 100 \mu\text{m}^2$. A device with four contacts could be as large as $500 \times 500 \mu\text{m}^2$. Therefore, maxima of 9 devices could possibly be made in one substrate, located at $D_{1,1}$, $D_{1,5}$, $D_{1,9}$, $D_{5,1}$, $D_{5,5}$, $D_{5,9}$, $D_{9,1}$, $D_{9,5}$, $D_{9,9}$.
5. Before write the contact leads by EBL, the contact pattern need to created for each Sb_2Te_3 nanowire. Figure 3-9 shows a four contacts pattern on a fake nanowire. Re-

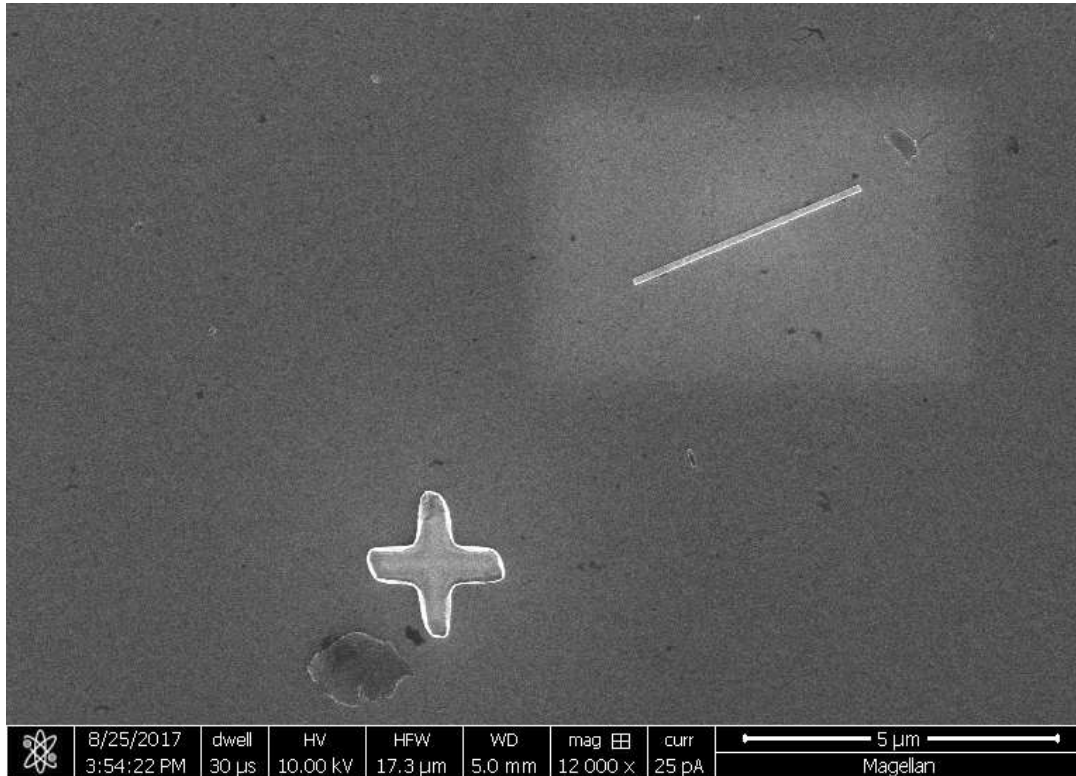


Figure 3.9: The SEM image of a Sb_2Te_3 nanowire with a cross nearby to define its coordinates.

member that SEM image of each nanowire and a nearby cross was taken. Now the image need to be adjust to the right scale as the contact patterns. Then, the .dc2 file is created in Design CAD environment with the pattern correctly on the nanowire and also define the origin at the center of the cross.

6. Spin-coat the sample for EBL writing the contact electrodes. In this procedure, all you need to do is aligning crosses precisely step-by-step and find out the cross of origin that near the nanowire. Then, run its own pattern file to write it.
7. One step of EBL contact writing can be done on this type of devices for just one type of electrodes. Two-steps of writing also can be used for creating two different types of electrodes. An example of Sb_2Te_3 lateral device is shown in Figure 3-10 with all four

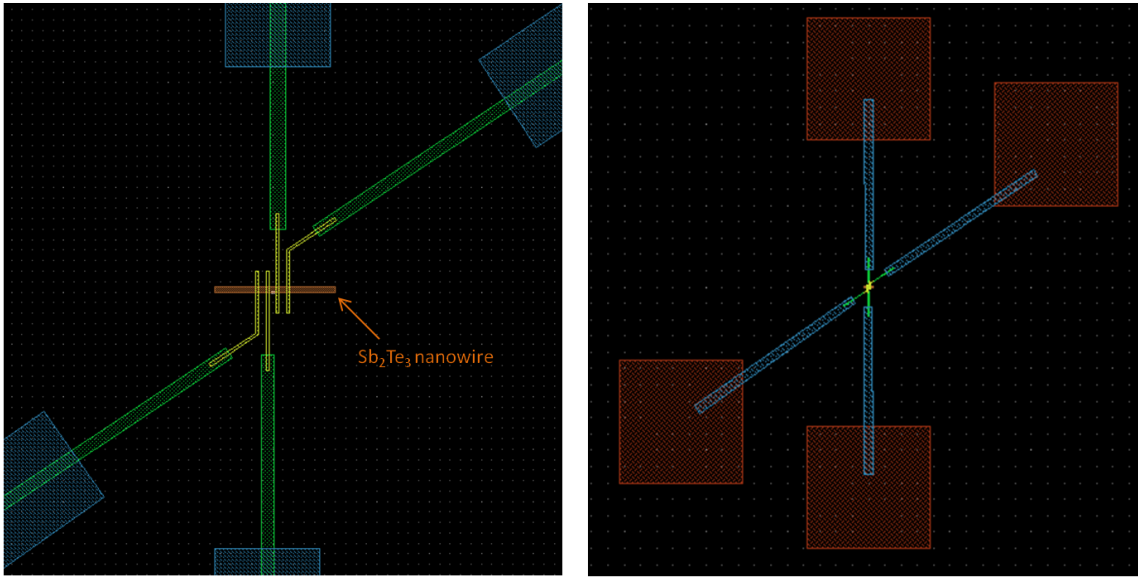


Figure 3.10: The drawing of four electrodes contacts for randomly located small nanowires.

electrodes are Co (40 nm)/Al(5 nm) electrodes.

8. Finally, the sample is loaded into etching system to remove 3 nm Pt layer.

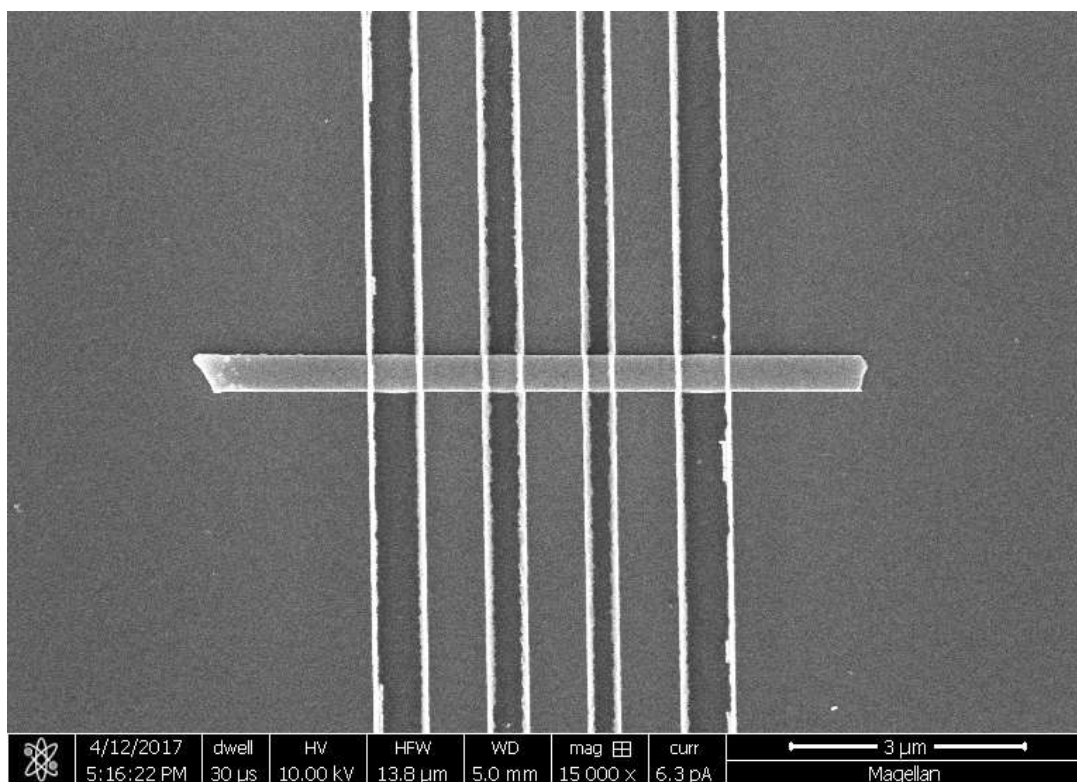


Figure 3.11: The SEM image of a lateral Sb_2Te_3 nanowire device with four Co (40 nm)/Al(5 nm) electrodes.

Chapter 4

GMR-based and AMR-based SHOs

4.1 Introduction

STOs which rely on spin angular momentum exerts on a FM to excite magnetization self oscillations have great potential for applications in communication, navigation, and microwave sensing systems.[16, 25–31] Recent observations of a new type of STOs have attracted a lot of interests due to its simple and flexible design of devices. Based on spin Hall effect (SHE) [13–15, 32–35], a lateral current in a non-magnetic layer generates transverse pure spin current, the adjacent FM layer is excited by spin orbit torques and self-oscillates to generate microwave AC signals. Recent studies on Pt-metallic FM devices with different geometries [36–42] and Pt-magnetic insulator system [43] also indicate that that these current-in-plane (CIP) SHOs have comparable characteristics and advantages to STOs.

One of the key reasons that obstacle SHOs toward the real application is the magnitude of microwave output powers. From the studies up to date of STOs, the system which based on magnetic tunnel junctions (MTJs) demonstrates higher output powers up to 0.1 to 10 μW . [44–48] However, due to the nature of quantum behavior of MTJs, tunneling

magneto-resistance (TMR) effect arisen from highly polarized, non-scattered tunneling current requires current perpendicular to the plane (CPP) geometry of the device. This limited the possibility by applying lateral SHE into MTJs-based system, thus the nanoscale MTJ device fabrication becomes a consumable and complicate process. Let alone there is an issue related to impedance mismatch to RF circuits of TMR-based STO systems. Since conventional CPP-GMR STO devices usually provides reasonable microwave power output with narrower linewidth oscillation modes [49–53], we suggest to apply CIP-GMR structure into SHO system. To our knowledge, this GMR-based SHO system could be the biggest power boost among the lateral SHO systems.

In this dissertation, we investigate the dynamics of magnetization of GMR-based SHO nanowire devices. The device structure combine with Pt layer to the metallic spin valve multilayers, which consists of a free FM, a normal metal (NM), a pinned FM, and an anti-ferromagnetic (AFM) layers. Figure 4.1(b) shows the schematics of this SHO system. The comparison to the bi-layer (HM/FM) SHO device is also included.(The schematic shows in Figure 4.1(a)) The operation of these devices relies on the SHE, which converts the charge current flow in the plane of HM layer into the pure spin current flow across the HM/FM interface. This pure spin current works as the anti-damping torque on the magnetization of free FM layer and results in self-oscillations. The self-oscillation corresponds to the resistance oscillation of MR. Figure 4.1(c) and (d) show the angular dependence of AMR and GMR. If the equilibrium direction of magnetization is fixed at 90 degree, the spin Hall effect induced spin current direction, the oscillations happens at the red circle point for both GMR and AMR SHOs. The AC resistance difference (δR_{ac}) is obviously larger at the incline slop position for GMR angular curve than the valley position for AMR angular curve. Therefore, the investigation of angular dependence of the GMR-based SHOs supports the enhancement of output powers. It also reveals the most efficient consuming of spin orbit torque while in operation of these devices. Moreover, the microwave power generation is corresponded to CIP GMR. Since the GMR value is usually larger than the AMR, the microwave power

output of GMR SHO is far above the power output by any bilayer AMR-based SHO systems. The maxima power output achieved of GMR SHOs is 2 nW in our studies.

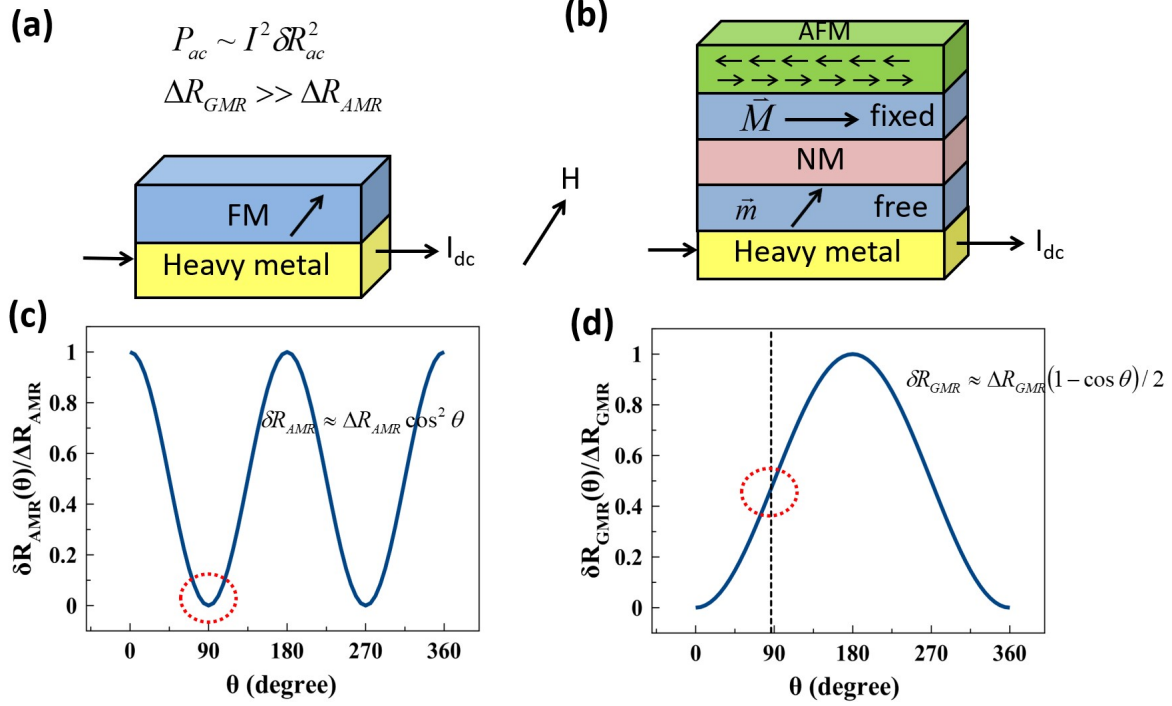


Figure 4.1: **(a)** The schematic of AMR-based SHO structure which includes one FM layer and one HM layer. The in-plane DC current flow through the HM layer to generate spin current in in-plane perpendicular direction via Spin Hall effect and add onto the FM layer. The top two equation simply imply the behavior that AC output power is proportional to resistance oscillation. The amplitude of resistance oscillation comes from MR, which is GMR or AMR here. And the GMR magnitude is much larger than AMR magnitude. **(b)** The schematic of GMR-based SHO structure, which includes a free FM layer, a normal metal (NM) layer, a fixed FM layer and a AFM layer. **(c)** The normalized AMR angular dependence plot. The AMR variance is proportional to $\cos(\theta)^2$. **(d)** The normalized GMR angular dependence plot. The GMR variance is proportional to $(1 - \cos(\theta))/2$.

4.2 SHO nanowire devices, GMR and Spectrum

The GMR-based SHO nanowire devices were patterned from a sapphire (substrate)/IrMn (4)/Co (2)/Cu (4)/Co (0.5)/Py (3.5)/Pt (5) multilayer (thickness in nanometers), which was deposited by magnetron sputtering. The 0.5 nm cobalt layer was inserted in between Cu and Py layer to modify the interface and enhance the GMR ratio. [54] This metallic spin valve multilayer was processed with an in-field post annealing at 250°C for 1 hour to determine the orientation of pinned FM layer (Co layer) by AFM exchange bias pinning effect [55, 56]. The magnetization orientation of Co layer was along the nanowire axis and defined as the easy axis. The geometry of nanowire was defined by using e-beam lithography and Argon ion milling. The width was 65 nm and the length was 40 μm in order to approximate the demagnetization field close to zero along the wire axis. The device was fabricated to have a 740 nm microwave emission active region in between the two attached Ti (5 nm)/Au (40 nm) contact leads. Figure 4.2(a) shows the scanning electron microscopy (SEM) image and the layer structure of the GMR-based SHO device. The AMR-based SHO nanowire device was also fabricated with a similar geometry (width 70 nm, active region 650 nm) shown in Figure 4.2(b). This control sample was made from the sapphire (substrate)/Cu (4)/Co (0.5)/Py (3.5)/Pt (5) multi-layers. By adding the Cu layer in this control sample, we can keep similar current density flow through the Pt layer to excite self-oscillations.

For the GMR-based SHO nanowire and the AMR-based SHO nanowire, the electrical measurements were performed in a cryogenic system at liquid helium temperature (4.2 K). The magneto-resistance (MR) curves were investigated of both devices by sweeping an external magnetic field along the easy (hard) axis. The MR difference of GMR-based SHO nanowire is about 10 times larger than the value of AMR-base SHO nanowire. The GMR effect with the field along the easy and hard axis of the device are shown in Figure 4.3(a) and Figure 4.3(b). Figure 4.4 shows the AMR value with the field applied perpendicular to the nanowire axis. Since the microwave signal, $V_{ac} \approx I_{dc}\delta R_{ac}$, is generated from the self-oscillations of magne-

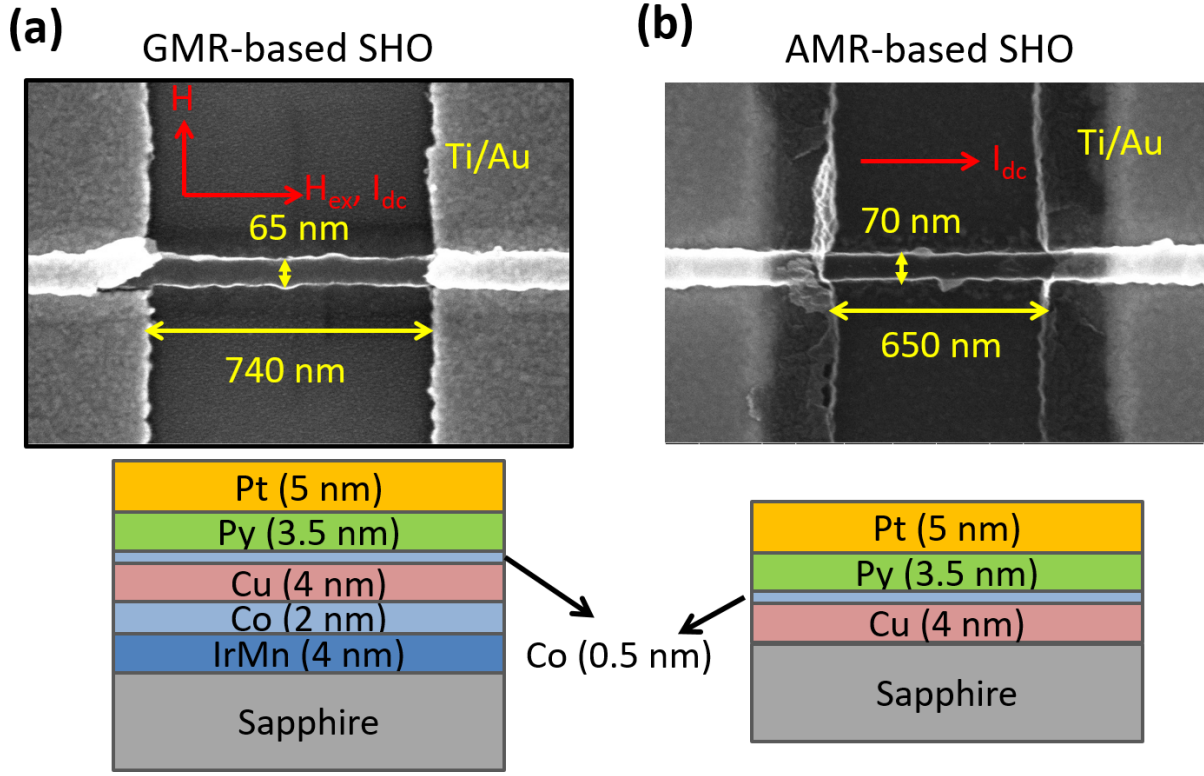


Figure 4.2: (a)/(b) The scanning electron microscopy (SEM) image of GMR/AMR-based SHO nanowire device and its multilayer structure showing on the bottom.

tization that is magneto-resistance oscillations (δR_{ac}). Therefore, the microwave emission power of GMR-based SHO is expected to be much larger than that of AMR-based SHO based on the MR values.

Figure 4.5 shows the microwave emission spectrum of the devices. A dc current was applied to the device to excite the self-oscillation and the microwave signal was generated via the GMR or AMR resistance oscillations and measured by a spectrum analyzer. Figure 4.5(a) is the power spectral density amplitude of GMR-based SHO as functions of emission frequency and applied dc bias. An 800 G external field was applied in-plane perpendicular to the nanowire axis. (Hard axis) Figure 4.5(c) shows the single spectra at 6 mA cross section line of Figure 4.5(a). In comparison with the GMR-based SHO, Figure 4.5(b) and (d) also shows the spectrum of AMR-based SHO and the cross section spectra at 3.65 mA. In order to

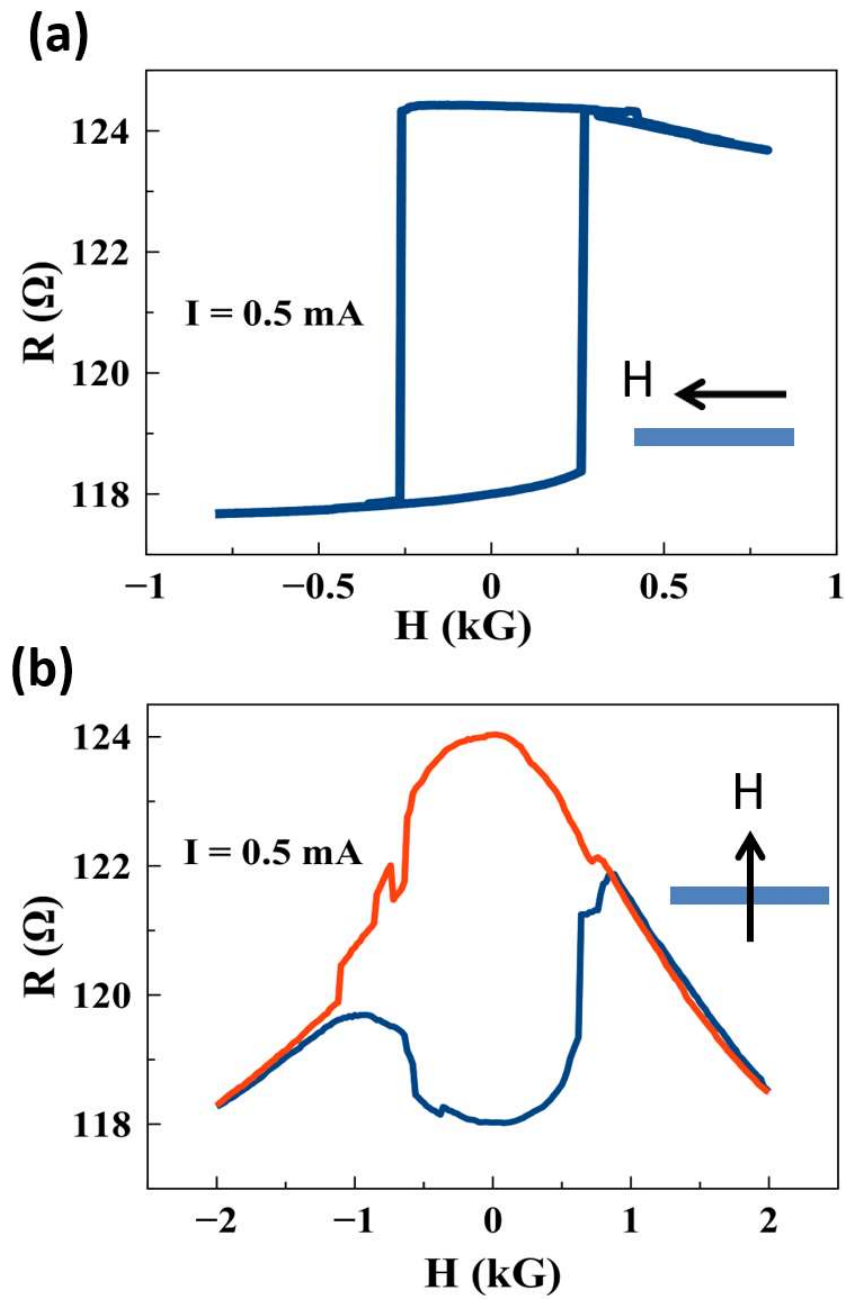


Figure 4.3: (a)/(b) The MR of the GMR-based SHO device with the magnetic field applying in-plane parallel to the easy/hard axis.

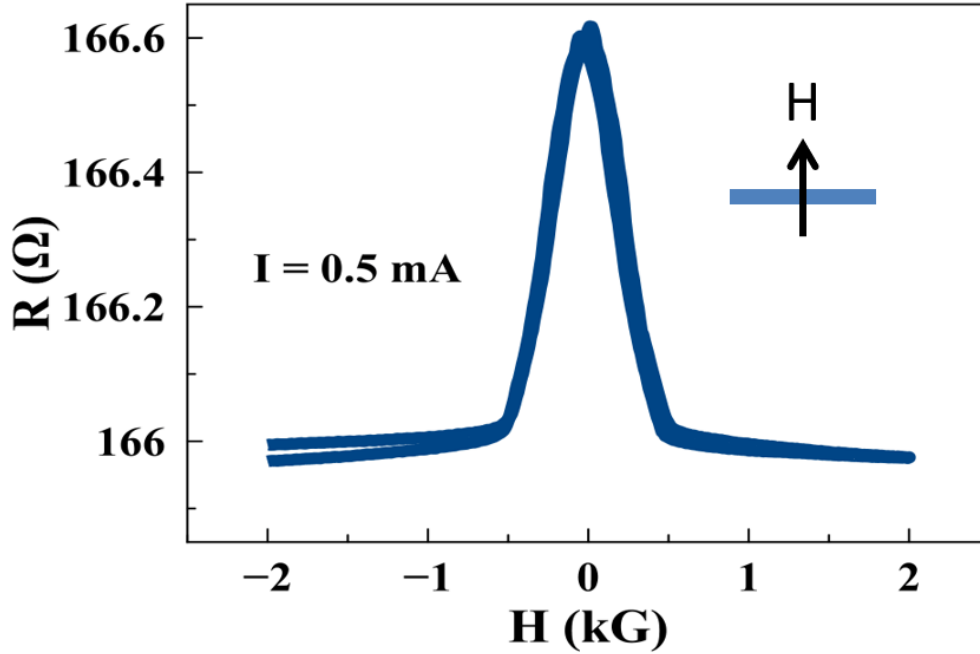


Figure 4.4: The MR of the AMR-based SHO device with the magnetic field applying in-plane parallel to the nanowire axis.

compare to the GMR-based SHO device with similar conditions, an 800 G external field was applied to the AMR-based SHO device 85 degree with respect to the nanowire axis (near perpendicular to the nanowire axis). In Figure 4.5(a), the oscillation frequency increases as applied dc bias increases. This blue-shift behavior is likely from the dynamic dipolar interaction to the pinned cobalt layer oscillation modes. In previous reports[36, 40, 42], the frequency red-shifts of spectrum is usually observed in Pt/Py AMR-based SHO systems. One of the possible reasons is due to the dc bias induced oersted field exerting on the FM layer and decreasing the effective magnetic field. In the AMR-based SHO device which we reported in this letter, a copper layer was specifically added under the Permalloy (Py) layer. Since the current density flow through the top Pt layer is similar to the bottom Cu layer, there is no obviously shifting of spectrum (Figure 4.5(c)) as a function of applied dc bias. To be noticed, the excitation bias current of GMR-based SHO is larger than the one of AMR-based SHO. Also, the linewidth of the self-oscillation mode of GMR-based SHO is

larger than the one of AMR-based SHO. (Figure 4.5(c) and Figure 4.5(d)) This implies that the thermal noise, which comes from the shunted current through the spin valve multilayer, on GMR-based SHO is greatly limiting the emission efficiency.

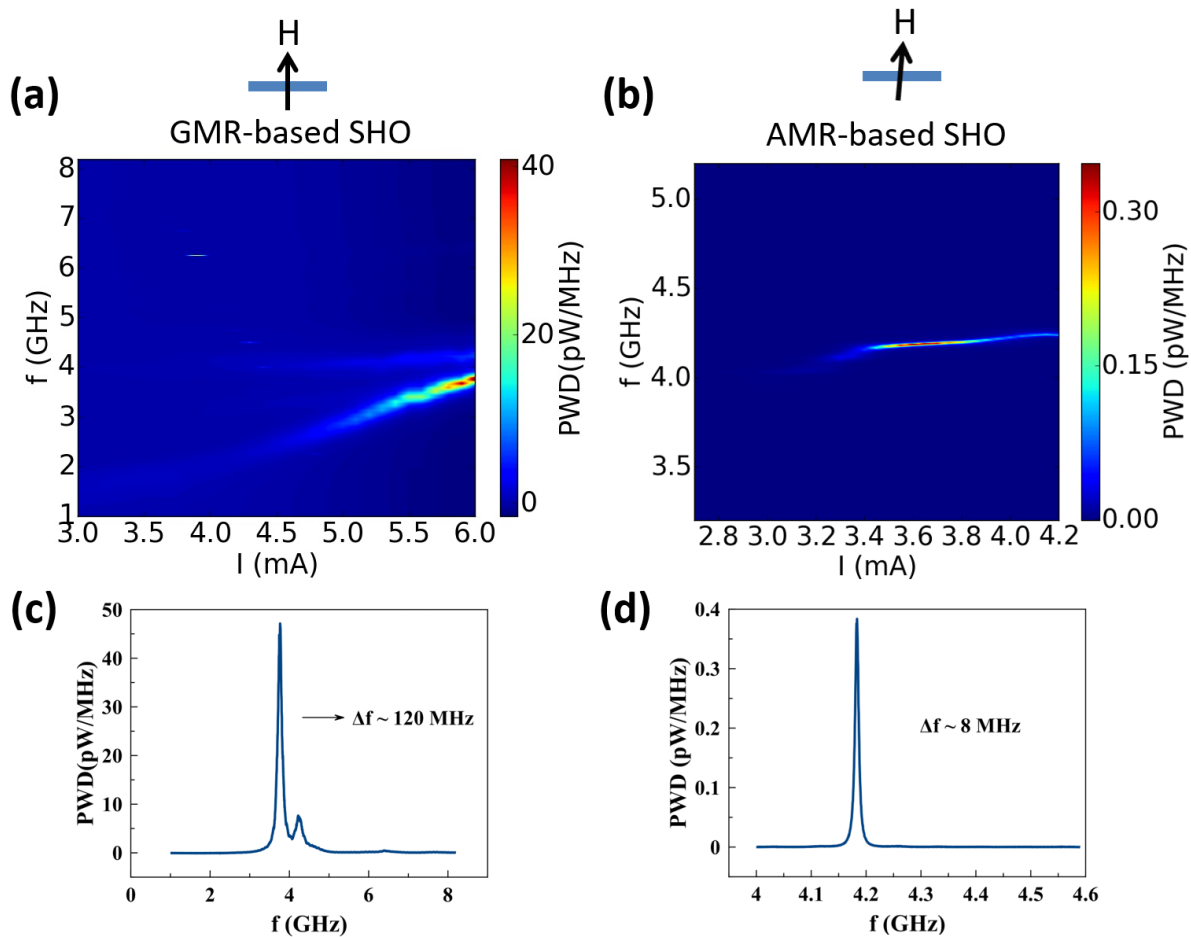


Figure 4.5: **(a)** Current bias (I_{dc}) dependent power spectral density (PSD) of GMR-based SHO device at $H = 800$ G. **(b)** Current bias (I_{dc}) dependent PSD of AMR-based SHO device at $H = 800$ G. **(c)** The PSD cross line profile of GMR-based SHO spectrum at $I_{dc} = 6$ mA. **(d)** The PSD cross line profile of AMR-based SHO spectrum at $I_{dc} = 3.65$ mA.

4.3 Integrated power analysis

Next we extracted out the integral microwave emission power of both devices for comparison. Figure 4.6 shows the integrated power as a function of applied dc bias current of both

GMR-based SHO (blue curve) and AMR-based SHO (red curve). The Figure 4.6(b) is the enlargement of the red curve in Figure 4.6(a). The highest output power of the GMR-based SHO device happened at 6 mA is around 1.2 nW whereas the highest power of AMR-based SHO device is 4.6 pW at 3.6 mA. In an approximated evaluation, the microwave emission power is proportional to the square of current and GMR and AMR resistance differences. $P_{GMR(AMR)} \sim (I_{dc} \cdot \Delta R_{GMR(AMR)})^2$ By calculating the ratio from the equation, $P_{AMR}/P_{GMR} \approx 0.004$, this value is surprisingly matched to the experimental result. In our experiments, the integrated power of the GMR-based SHO did not reach the highest power output in Figure 4.6(a), because we limited the applied bias current to protect of nano-geometry device. Therefore, the non-maxima power output usually demonstrates that the spin wave mode of GMR-based SHO is less coherent in oscillations and thus less emission power output than expected. However, the AMR-based SHO has been shown that maxima emission power should be happened while its magnetization equilibrium orientation is at 45 degree with respect to the nanowire axis. So the integrated power of AMR-based SHO taken at 85 degree with respect to nanowire axis (shown in Figure 4.6(b)) is smaller in magnitude than that in the maxima position. Since both the GMR and AMR-based SHOs output less microwave power in our experimental configuration, this leads to the result to be quite reasonable.

4.4 Angular dependence

As we mentioned in previous paragraphs, the output power of SHO is related to the oscillations of MR of FM layer, which depends on the magnetization orientation relative to a reference direction. This reference direction is the pinned FM layer direction of the GMR-based SHO, and its also the current flow direction of both GMR and AMR-based SHOs. In this report, we have it always along the nanowire direction. Therefore, the integrated

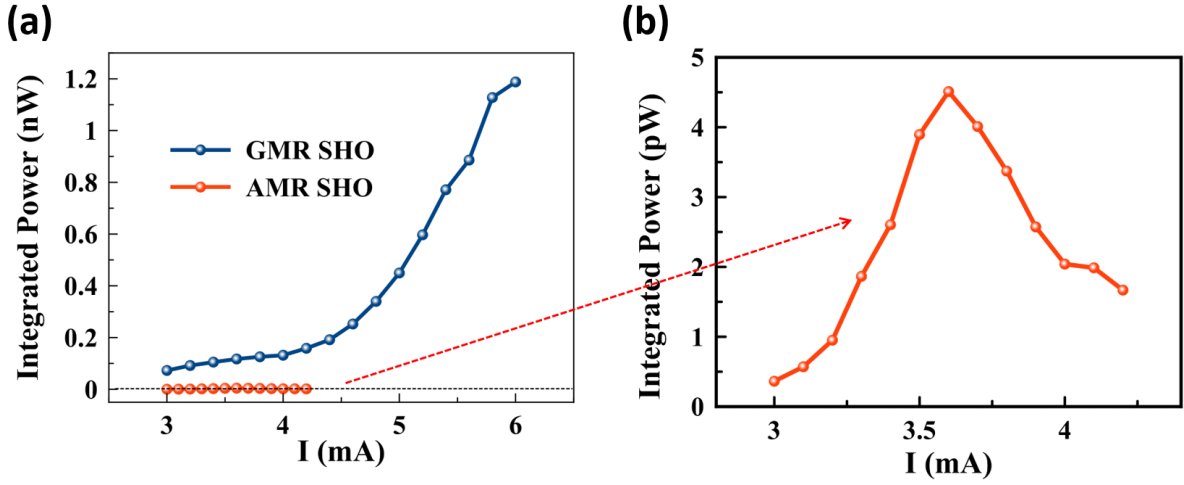


Figure 4.6: **(a)** The bias dependent auto-oscillation integral microwave power of GMR based SHO (blue) and AMR-based SHO (red). **(b)** The enlarge image of the red curve plotted in (a).

power of SHOs possesses an angular dependence due to the origins of angular differences of AMR and GMR. The resistance oscillations can be written as the changes of the relative angles. $\delta R_{ac} \frac{\partial \Delta R(\theta)}{\partial \theta} \delta \theta(\omega, t)$. For GMR-based SHO, $\frac{\partial \Delta R_{GMR}}{\partial \theta} \sim \sin(\theta)$, the maxima of resistance oscillation is happened at 90 degree with respect to nanowire axis. Whereas for AMR-based SHO, $\frac{\partial \Delta R_{AMR}}{\partial \theta} \sim \sin(2\theta)$, the maxima is at 45 degree. Figure 4.7 shows the integrated power angular dependence of both the GMR and AMR-based SHOs. A 500 G external field was applied at the angle θ related to the nanowire axis. The microwave emission signals were taken in a 90 degree range at a constant bias current. There is one single maximum of GMR-based SHO at $\theta = 90$ degree and two maxims of AMR-based SHO at 70 and 110 degrees. Figure 4.7(a) proves that the maxima power of GMR-based SHO is exactly at 90 degree angle and the power drops quickly when the external field is applied off from the 90 degree angle. In Figure 4.7(b), the highest power output of AMR-based SHO is not at 45 degree instead it is symmetric and 20 degree off from the 90 degree angle. Since the demagnetization field of 1-D nanowire is much larger along the wire axis, the magnetization orientation is dragged toward the nanowire axis. Also, the spin orbit torque which comes from the spin Hall Effect in Pt layer is most efficiently transferred as an anti-damping torque

at 90 degree. The threshold current of SHO possesses a trend as function of external field direction relative to the nanowire axis. So power maxima angles of AMR-based SHO should be in between the 45 and 90 degree angles as what we expected.

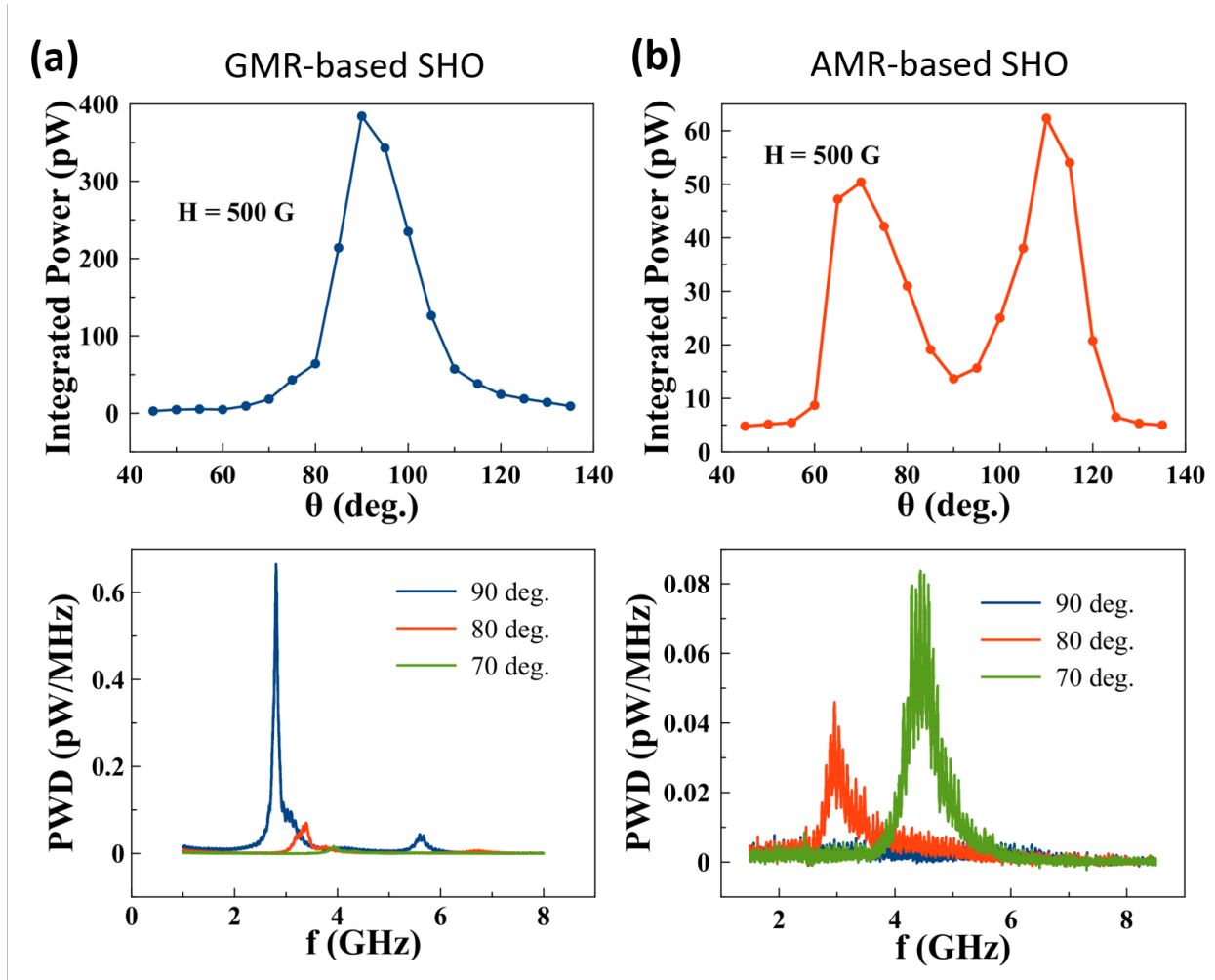


Figure 4.7: (a) The angular dependence of the integral power of GMR-based SHO at $H = 500$ G. θ indicates the angle of applied external field related to the nanowire axis. The bottom graph shows the single spectra of θ equals to 90, 80, and 70 degree. The integrated power decreases as the θ increases. (b) The angular dependence of the integral power of AMR-based SHO at $H = 500$ G.

4.5 Conclusion

There have been lots of studies on different SHO systems, for example, nanogap contacts on heavy metal (HM)-FM disk, nano-constriction of Pt-Py bilayer structure, and 1D Pt-Py nanowire. In these SHO systems, the advantages include easier fabrication steps and direct optical measurement on the oscillation active region. However, these SHOs usually exhibit lower emission power output. By integrating the GMR stack into the SHO nanowire, we still keep the benefits of the SHO systems and also largely enhanced the output powers. The possible improvements of GMR-based SHO could be introduced and enhance the output powers even more. For example, the thermal stability can be increased by decreasing the distance of contact leads. The GMR stack could be optimized by increasing the stiffness of pinned layer and GMR ratio of devices. Recent study on multiple nano-constricted bilayer SHO devices have shown that the mutual synchronization of SHOs was achieved and enhanced the output power. The method which synchronizes multiple nano devices has been applied to both STO and SHO to increase output powers. This also promises the GMR-based SHOs to be able to reach sufficient power for real applications. We have shown that by integrating the GMR metallic spin valve stack into the SHO nanowire device, the output powers can be significantly enhanced. Remarkably, comparing to the conventional bilayer AMR-based SHO system, the output powers can be increased more than an order of magnitude. Further, the simple fabrication of oscillators could be beneficial for developing and building into future electronic applications.

Chapter 5

Ionizing Radiation Effect on Perpendicular Magnetic Tunnel Junctions

5.1 Introduction

Spin transfer torque random access memories (STT-MRAM) are non-volatile memories that have the advantage of fast write times [57], low power consumption, and scalability of storage densities up to terabits/cm². The magnetic tunneling junction (MTJ), the core component STT-MRAM, is believed to be radiation hard, i.e. robust to the effects of ionizing radiation, therefore making STT-MRAM attractive for applications such as in/near outer space; particle accelerators; and nuclear reactors, warfare, or catastrophe. However, the effects of ionizing radiation on nanoscale MTJs capable of current-induced switching have not been experimentally studied. Here we report studies on the effect of extreme total ionizing dose gamma and neutron radiation on perpendicular anisotropy magnetic tunnel junctions

(pMTJs).

Previously, Ren et al. [4] have shown gamma and neutron radiation hardness of micron scale MTJs with in-plane free and reference layers. Their results showed that there was no statistically significant change in either the tunneling magnetoresistance (TMR) or the coercivity of their devices after either irradiation. However, these devices were too large to be practical for STT-MRAM application as they cannot be switched by applied current.

The focus here is to study the radiation effects on nanoscale MTJs that have characteristics suitable for use as STT-MRAM. For this reason, we study MTJs with easy magnetization axis perpendicular-to-plane, or so called pMTJs, as pMTJs are the current most promising candidate toward device applications. Specifically we focus on the effects of irradiation by gamma rays and thermal neutrons plus gamma rays.

A typical structure of the pMTJ element for use in STT-MRAM is schematically shown in Figure 5.1, where two effective ferromagnetic layers (typically CoFeB based) are separated by an insulating tunnel barrier (typically MgO). In order to reduce stray fields, the reference layer is generally made to be a synthetic antiferromagnet (SAF) consisting of two ferromagnetic layers anti-ferromagnetically coupled across a thin non-ferromagnetic spacer. Additionally two non-ferromagnetic metallic layers are required to make the electrical contact to the top and bottom of the nanopillar.

Unlike conventional memory elements, STT-MRAM has no semiconductor silicon layers and any dopants as core ingredients. The effect of generation of defects in STT-MRAM is way much less important than in semiconductor due to the influence in electric transport properties. So the metallic layers of STT-MRAM are expected to be robust against ionizing component. However, the Boron in the typically used CoFeB magnetic layers could be likely one issue due to the large cross section B^{10} to thermal neutrons[58] which leads to creation of a Li^7 atom, a neutron, and an alpha particle.

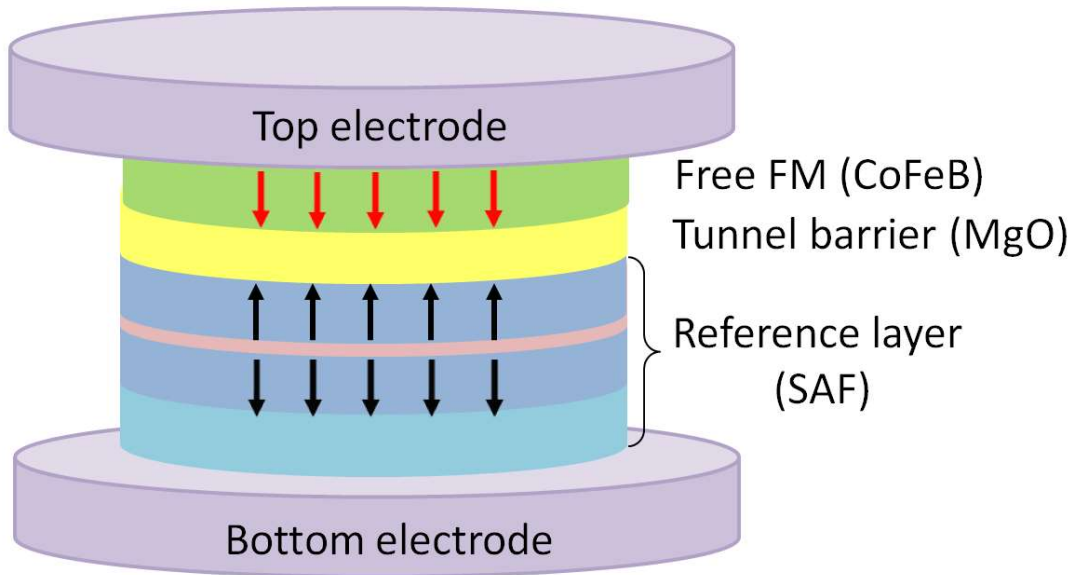


Figure 5.1: Schematic of a perpendicular MTJ.

One would expect that the main radiation induced damages to be mostly at interfaces and at the insulating tunnel barrier layer. In particular, radiation induces charge excitation and atomic displacements that cause, respectively, charge accumulation and color center formation in bulk. In thin films, the radiation-induced charges can create charge sheet buildup and affect potential drop across the tunnel barrier layer [59, 60]. Radiation induced defects within the tunnel barrier can also create a conduction channel for additional leakage current and drastically alter the TMR, and hence change the bit state of the memory cell.

5.2 Irradiation considerations

Gamma radiation was provided using an in-house 5,000 Ci Cs-137 gamma cell at a dose rate of 2.14 kGy/h water equivalent dose, which is approximately equivalent to 1.96 kGy/h in silica using a conversion factor of 0.916.[61] The accumulated gamma dose to the chips was 160 kGy (160,000 J energy deposited per kg mass) to water or 147 kGy(SiO₂). After irradiation of the samples to reach the total dose, the samples were removed from the gamma cell and taken for post irradiation characterization.

A mixed radiation field of low linear energy transfer (LET) radiation from gamma and high energy beta as well as neutrons was provided using the UC Irvine TRIGA[®] reactor. The samples were lowered into an irradiation position in the Lazy Susan compartment of the reactor core where the LET dose was approximately 40 kGy/h dose to water and the thermal neutron dose was 0.8×10^{12} n/cm²·s. The samples were irradiated for 8 hours and were subsequently removed from the core and placed in a shielded lead cave to allow the radioactive isotopes to decay. After a sufficient time (~ 6 months) for safe handling, the samples were taken for post irradiation characterization. At the time of post irradiation characterization, the radiation dose at the surface of the samples was 0.9 mrem/h. The remaining radioactivity was primarily due to Ta¹⁸².

5.3 Experimental Details and Data

To study the effects of ionizing radiation on nanoscale pMTJs, we examine sets of both nominally circular 60 nm (diameter) and elliptical $50 \times 150 \text{ nm}^2$ (minor \times major axes) pMTJs. The stacking structure is as follows: (bottom electrodes)|pinned FM|MgO|free FM|(top electrodes).

A subset of the devices (23 circular, 18 elliptical) were exposed to 2.14 kGy/h(H_2O) gamma radiation for a total dosage of 147 kGy(SiO_2). After irradiation of the samples to reach the total dose, the samples were removed from the gamma ray chamber and taken for post irradiation characterization.

Additionally, nominally identical samples (54 circular, 69 elliptical) were exposed to a mixed radiation field of low linear energy transfer (LET) radiation from gamma and high energy beta for 8 hours in TRIGA[®] reactor. The total LET dose was 293 kGy(SiO_2) and the thermal neutron dose was $0.8 \times 10^{12} \text{ n/cm}^2 \cdot \text{s}$. The samples were irradiated for 8 hours and were subsequently removed from the core of reactor and placed in a shielded lead cave to allow the radioactive isotopes to decay. After a sufficient amount of time (6 months) for safe handling, the samples were taken for post irradiation characterization. At the time of post irradiation characterization, the radiation dose at the surface of the samples was still 0.9 mrem/h. The remaining radioactivity was primarily due to Ta^{182} , from the Ta used in the electrodes.

Finally, a subset of samples (16 elliptical) were not exposed to any irradiation. These samples were also characterized before and after the 6 month time span as the TRIGA[®] irradiated samples.

For all devices, the TMR and field switching characteristics were determined by means of resistance vs. external field measurements. The MTJ nanopillars were contacted by

microwave probe, and the TMR was measured by applying small probing direct current (5 μ A) while the perpendicular field magnitude was swept. Example data for an elliptical nanopillar before and after neutron (TRIGA[®]) radiation is shown in Figure 5.2(a). The TMR value is determined from the resistance values with free layer parallel (P-state) and anti-parallel (AP-state) to the reference layer, given by

$$TMR = \frac{R_{ap} - R_p}{R_p} \times 100\%. \quad (5.1)$$

Two parameters are defined using the mean positions of transition of free layer state from P \rightarrow AP and AP \rightarrow P. One is the field at the center of the bistable region H_o determined as the average of these quantities, and the other is the width of the bistable region H_w taken as the difference of the positions, see Figure 5.2(a). The shift from zero field of H_o is due to the fact that the SAF in these structures is not fully compensated. H_w is a measure of the coercivity of the free layer and thus its stability.

The current switching characteristics were determined by setting the external field to the determined H_o value and sweeping the applied direct current. Again two other parameters are defined using the mean positions of the current induced transition, the current at the center of the bistable region I_o and the width of the bistable region I_w , see Figure 5.2(b).

The TMR and field switching data (H_o and H_w) are shown for before/after gamma irradiation of circular devices in Figure 5-3(a) represent by blue/red respectively. The plotted error bars are based on the range of positions of P \rightarrow AP and AP \rightarrow P transitions based on 10 repeated measurements. The shifting of H_o and H_w before/after gamma irradiation is defined as ΔH_c and ΔH_w . ($\Delta X = X^{after} - X^{before}$) In Figure 5.3(b) and 5.3(c), we plot the distribution of the shifting of H_o and H_w for 23 circular devices. The most of population is centered at 0 for ΔH_o and ΔH_w , which suggest that there is no specific effect of gamma irradiation on field switching characteristics. The current switching data (I_o and I_w) and it's shifting

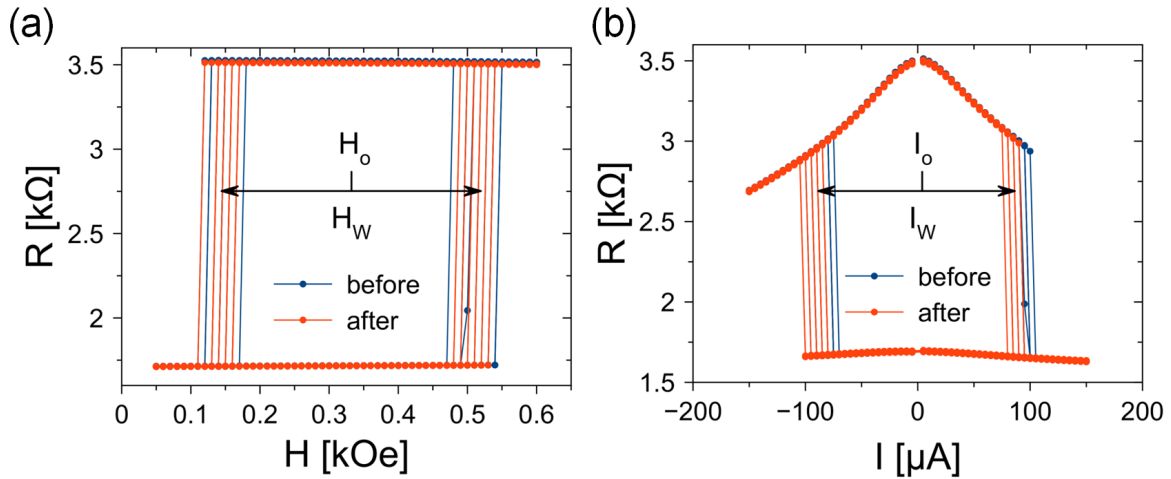


Figure 5.2: **(a)** Field and **b** current induced switching characteristics before and after neutron irradiation.

before/after gamma irradiation are plotted in Figure 5.4. Almost the same result is derived as the field switching data that there is nearly zero effect on pMTJ devices after gamma irradiation.

Figure 5.5 (a) shows the TMR and field switching data for before/after neutron (TRIGA[®]) irradiation of 63 elliptic devices. The shifting of H_o and H_w , ΔH_o and ΔH_w , is also plotted in Figure 5.5(b) and 5.5(c). Since TRIGA[®] source is a mixing of gamma ray and thermal neutrons, not only gamma ray could excite electrons to high energy states but also neutrons could interact with CoFeB layer and cause defects. A higher possibility that the MTJs could be damaged after extreme dose of neutron radiation. There is negligibility difference in TMR and H_o before/after neutron irradiation. However, The H_w shrank to slightly narrower after neutron irradiation. The distribution of ΔH_w decreased 8 % after neutron irradiation. When we look into the current switching data shown in Figure 5.6(a) to 5.6(c), I_o was not changed but I_w was also narrowing. The distribution of ΔI_w decreased 2.6 %.

We summarized a Table of ioning radiation effect on pMTJ samples.

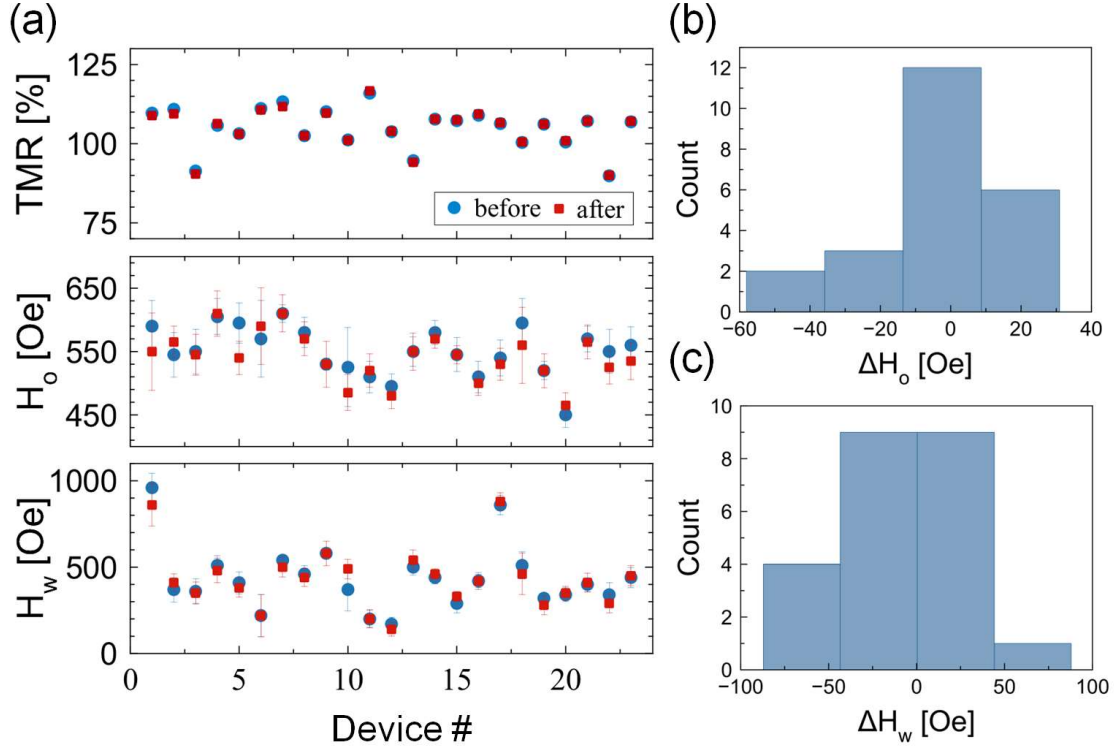


Figure 5.3: Before and after gamma irradiation results for 23 circular devices. **(a)** From top to bottom, TMR ratio; center of bistable field H_o ; width of switching field H_w . **(b)/(c)** The distribution of $\Delta H_o/\Delta H_w$ for 23 circular devices. $\Delta H_o/\Delta H_w$ is defined as $H_o^{after}/H_w^{after} - H_o^{before}/H_w^{before}$.

The mean parameter change ΔX and sample standard deviation σ_X are shown in Table 5.1, where $X = TMR, H_o, H_w, I_o, \text{ or } I_w$. The mean change is defined as $\Delta X = X^{after} - X^{before}$. For example, a negative value for the change in the width of the field switching loop given $\Delta H_w = H_w^{after} - H_w^{before}$ corresponds to a narrowing of the loop after irradiation. The average errors ϵ , determined using the interquartile range (IQR) of positions of $P \rightarrow AP$ and $AP \rightarrow P$ transitions as above, of H_w and I_w are also tabulated in Table 5.1. Note the average errors for H_o and I_o are half those of H_w and I_w , respectively. In the following, we compare ΔX to its corresponding σ_X as well as ϵ_X as a metric significant change.

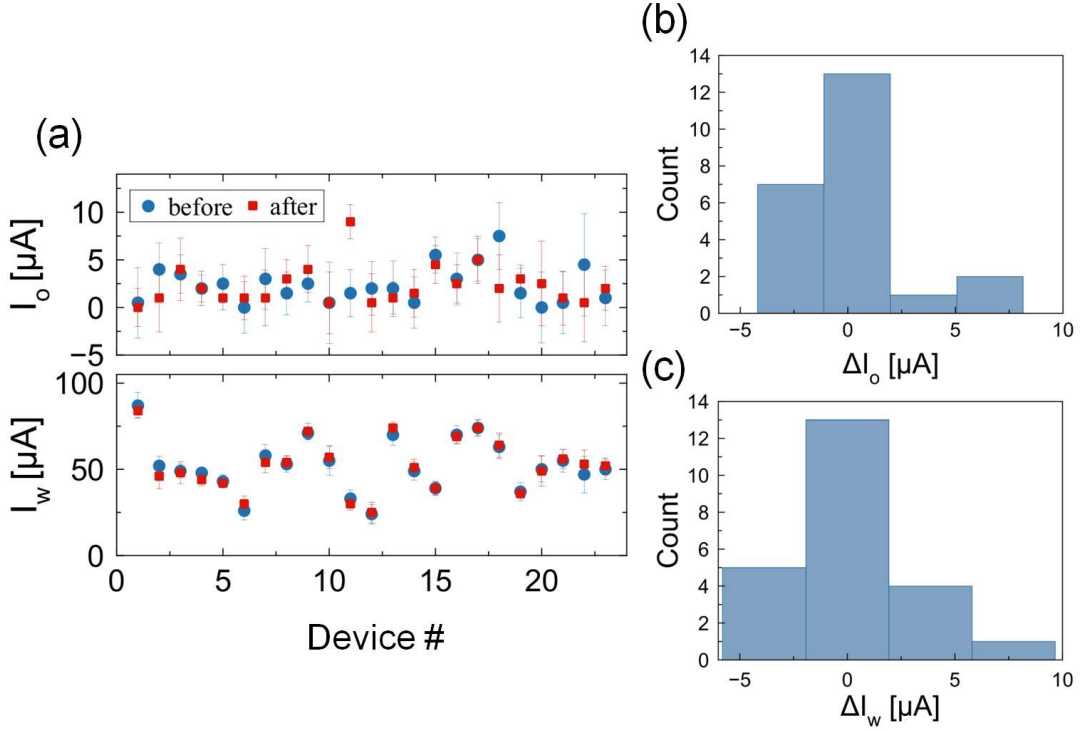


Figure 5.4: Before and after gamma irradiation results for 23 circular devices. (a) top: center value of current switching loop I_o ; bottom: width of current switching loop I_w (b)/(c) The distribution of $\Delta I_o/\Delta I_w$ for 23 circular devices. $\Delta I_o/\Delta I_w$ is defined as $I_o^{after}/I_w^{after} - I_o^{before}/I_w^{before}$.

As can be seen in Table 5.1 and figures above, in general the TMR was unaffected by either gamma or neutron irradiation. The sample-to-sample variation in this case is much larger than any difference before/after on any particular device. The only devices that displayed indication of change in TMR were the elliptical pMTJs subjected to TRIGA[®]. However, the mean change was less than 1 % and was equal to one standard deviation.

For the vast majority of the devices the before/after medians of H_o , H_w , I_o , and I_w overlap within one IQR, see Figures 5.3, 5.4, 5.5 and 5.6. This is evident from the overlap of the field and current switching loop traces in Figure 5.1 (a) and (b). All of the gamma irradiated samples showed negligible changes in all parameters. For the neutron irradiated samples,

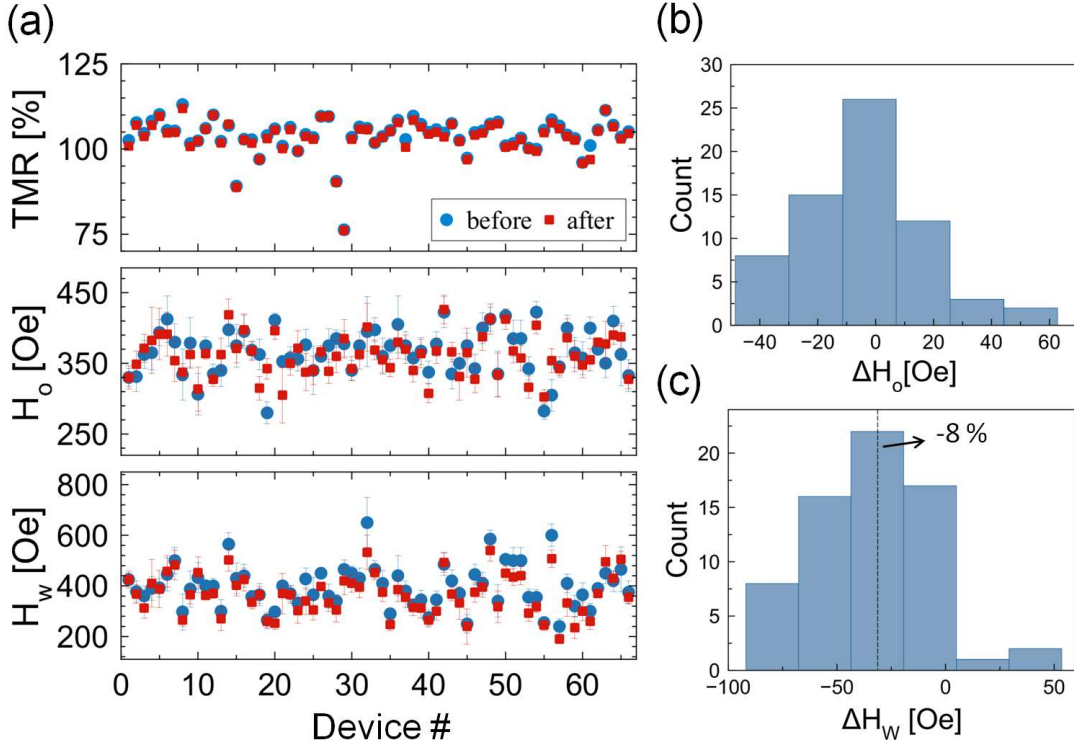


Figure 5.5: Before and after TRIGA[®] (neutron + gamma) irradiation results for 66 elliptical devices. (a) From top to bottom, TMR ratio; center of bistable field H_o ; width of switching field H_w . (b)/(c) The distribution of $\Delta H_o/\Delta H_w$ for 66 elliptical devices.

the circular devices exhibited a similar behavior. However, the elliptical neutron irradiated samples displayed a trend in a reduction in field switching loop widths with $|\Delta H_w| \approx \sigma_{H_o}$. Additionally, for these devices both ΔH_w and ΔI_w are negative, a correlation that could result from the pMTJ becoming less thermally stable. (However, this could also be attributed to changes in the room temperature.) Furthermore, ΔH_w (= 33 Oe) in this case is smaller than the mean IQR (= 40 Oe) for the individual measurements.

The elliptical samples that were not subjected to any irradiation showed a similar, yet opposite effect, as those for the elliptical neutron samples. In this case $|\Delta H_w| \approx \sigma_{H_o}$, and both ΔH_w and ΔI_w were positive with effect size similar to the neutron ellipses. For this

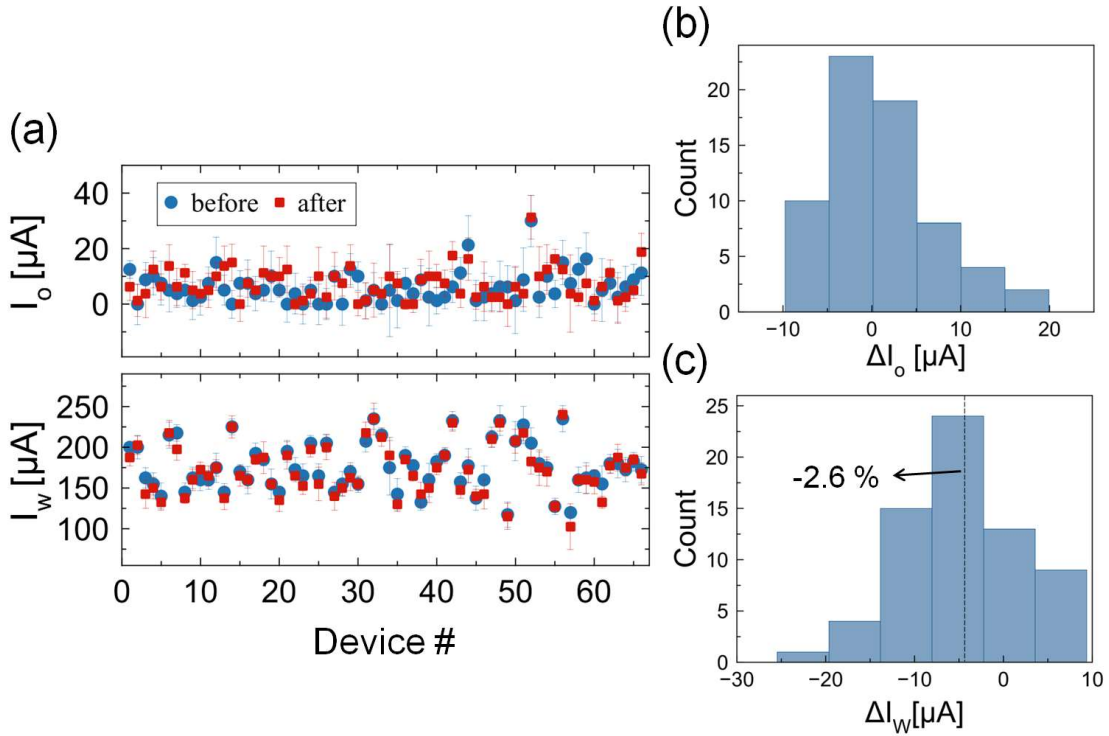


Figure 5.6: Before and after TRIGA (neutron + gamma) irradiation results for 66 elliptical devices. (a) top: center value of current switching loop I_o ; bottom: width of current switching loop I_w (b)/(c) The distribution of $\Delta I_o/\Delta I_w$ for 66 elliptical devices.

effect not to be due to measurement error or thermal variation, these samples would have had to become more thermally stable by sitting in ambient conditions. While possible, this is not a very probable explanation since the effect is smaller than the typical IQR.

5.4 Conclusion

In summary, our work shows that nanoscale perpendicular magnetic tunnel junctions suitable for use in ST-MRAM applications are robust to the effects of harsh ionizing radiation. We subjected devices to extreme total dose of either gamma irradiation or gamma plus thermal

Table 5.1: Summary of irradiation effects on samples

Shape	Radiation	N	ΔTMR %	σ_{TMR} %	ΔH_o Oe	σ_{H_o} Oe	ΔH_w Oe	σ_{H_w} Oe	ϵ_{H_w} Oe	ΔI_o μA	σ_{I_o} μA	ΔI_w μA	σ_{I_w} μA	ϵ_{I_w} μA
Circle	Gamma	23	-0.1	0.6	-9	20	-4	43	60	0	3	0	3	5
Ellipse	Gamma	28	-0.1	0.7	0	19	-2	17	44	3	5	-3	7	11
Circle	TRIGA [®]	54	-0.1	0.4	-11	25	-25	41	60	0	2	-1	4	6
Ellipse	TRIGA [®]	66	-0.6	0.6	-5	21	-32	30	40	1	6	-4	8	13
Ellipse	None	16	0.1	2.5	9	18	33	36	40	1	5	7	10	12

neutron irradiation. The tunneling magnetoresistance, field switching, and current induced switching characteristics showed negligible changes with respect to device operation.

Chapter 6

Spin-dependent transport properties in lateral Sb_2Te_3 nanowire devices

6.1 Introduction

Topological insulator (TI) nanostructures such as Sb_2Te_3 nanowires[62] has shown an unusual band structure with the coexistence of a conducting surface band and an insulating bulk band.[63] Spin-orbit interaction and time-reversal symmetry protected gapless states are the two unique properties that can conduct research works on not only to understand the fundamental principles but also to develop new applications on spin polarized devices. The previous research works on Sb_2Te_3 nanowires was focus on electron transport properties of topological surface states from nano-Angle Resolved Photoemission Spectroscopy(nano-ARPES) measurements. The positions of conducting surface Dirac cone and bulk valence band in momentum space were confirmed based on the result.[62] However, most of 3D TI systems have been further studied on electric spin-dependent transports with promising results of spin filtering from spin-momentum locking effect.[64–67] In this chapter, we

conducted the spin dependent transport experiments on Sb_2Te_3 nanowire lateral devices at cryogenic temperature. We have shown the results of weak anti-localization (WAL) and spin momentum locking (SML) effects of the Sb_2Te_3 nanowire device. Based on these results, we have a further understanding of TI material and it's possible application in spintronics.

6.2 Synthesis and fabrication of Sb_2Te_3 nanowire devices

The focus was on Sb_2Te_3 nanowires, one of 3D TI materials. The great interest is studying the spin-dependent transport behavior of Sb_2Te_3 nanowires. However, most of as-grown Sb_2Te_3 nanowires are usually heavily p-doped with its Fermi level lying in the bulk valence band. Therefore, in order to investigate the intrinsic properties of TI Sb_2Te_3 nanowires, the synthesis of high quality single crystalline nanowires is essential. The high quality Sb_2Te_3 nanoribbon (nanowire with rectangular cross section) that we studied in this project was grown by a low pressure catalytic chemical vapor deposition (CVD) method with vapor-liquid-solid growth mechanism. It is a typical chemical vapor deposition (CVD) system that consists of mass flow control units, rapidly thermal control furnace, and high vacuum pumping system. The as-grown Sb_2Te_3 nanowires were transferred onto the SiO_2/Si (001) substrate dispersively in order to make electrical contacts. The Sb_2Te_3 nanowire lateral devices are fabricated by patterning PMMA/MMA bilayer resist using two-step aligned e-beam lithography. Two outer non-magnetic metal (Nb/Au) electrode contacts and two inner ferromagnetic (FM) spin valve ($\text{AlO}_x/\text{Permalloy}/\text{Cu}/\text{Co}$) electrode contacts were deposited by magnetron sputtering. The channel distances between the electrodes are 0.9-1.2 μm and the width of the Sb_2Te_3 nanowire is 180 nm. After lift-off, the device is annealed in a high vacuum oven at 220°C for one hour. The schematic of the Sb_2Te_3 nanowire lateral device is shown in Figure 6.1. The completed device SEM image is shown in Figure 6.2. The

two Nb/Au electrodes were Ohmic contacts to the Sb_2Te_3 nanowire whereas the two FM electrodes were tunneling-conducted through thin Aluminum oxide barrier. The two FM electrodes (T2 and T3) were served as the spin injector and the spin detector of the device. For non-local lateral measurements, to create a high spin polarization current injected from the FM metals into the TI nanowire is crucial. People have proved that the Ohmic contacts between FM metals and graphene largely reducing the spin polarization of injecting current due to conductance mismatch.[68] In previous studies of electrical detection of SML effect of the TI systems[64, 65], introduce FM electrodes and tunneling contacts to TI surfaces is the key part of experiments. In order to alleviate the conductance mismatch, a thin Aluminum oxide barrier was inserted between the FM electrode and the Sb_2Te_3 nanowire in our system.

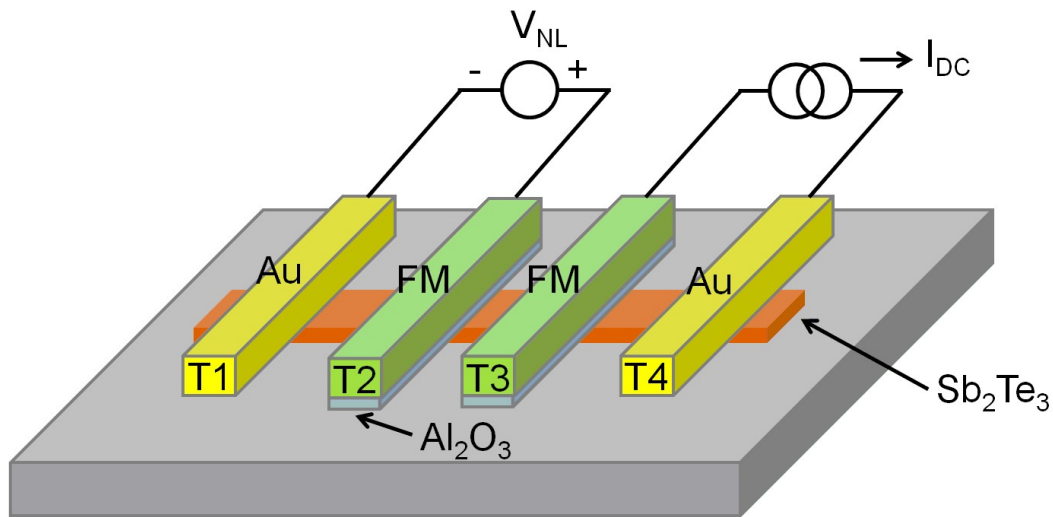


Figure 6.1: Schematic of the nonlocal spin valve device on a TI Sb_2Te_3 nanowire channel.

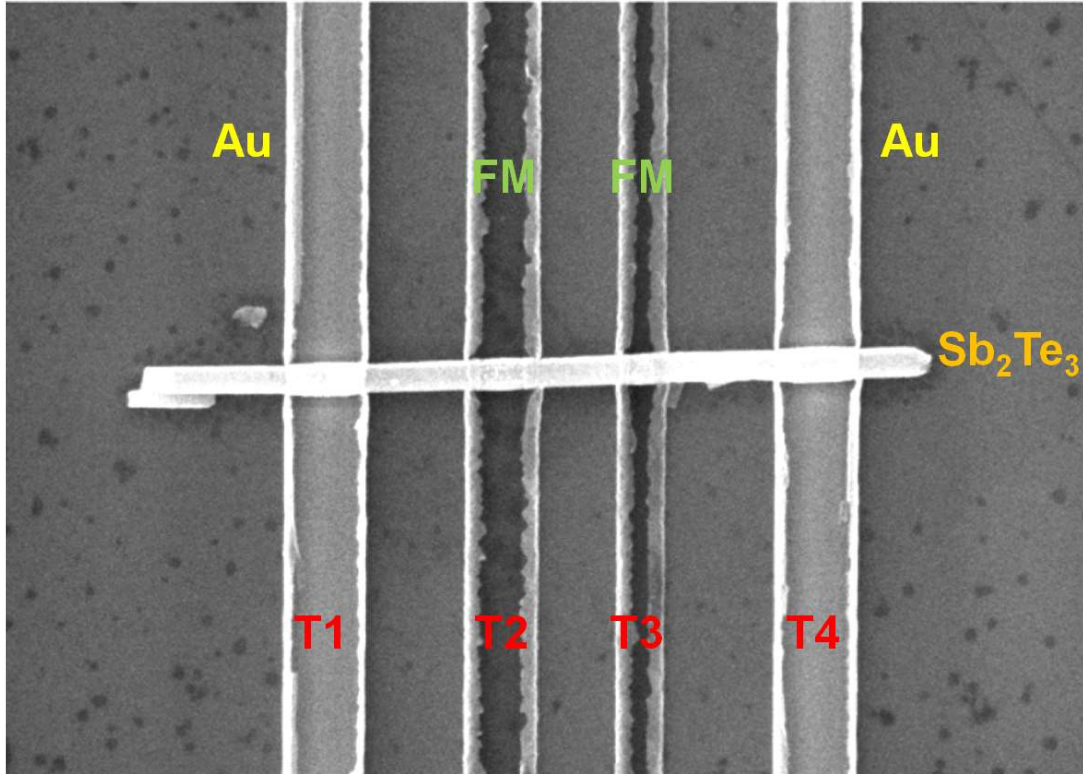


Figure 6.2: SEM image of the device with two inner Py/Cu/Co/CoO_x composite spin valve electrodes and two outer Nb/Au non-magnetic electrodes.

6.3 Magneto-transport properties of lateral Sb_2Te_3 nanowire devices

In Figure 6.3, the temperature dependent magneto-transport was measured through two Nb/Au contacts with the sweeping magnetic field in-plane perpendicular to the Sb_2Te_3 nanowire (Out-of-plane to the two side walls of Sb_2Te_3 nanowire). This MR behavior shows the weak anti-localization (WAL) effect at low temperature and decreases as temperature goes up, which suggests a strong spin-orbit (SO) coupling of TSS in the Sb_2Te_3 nanowire.[69]

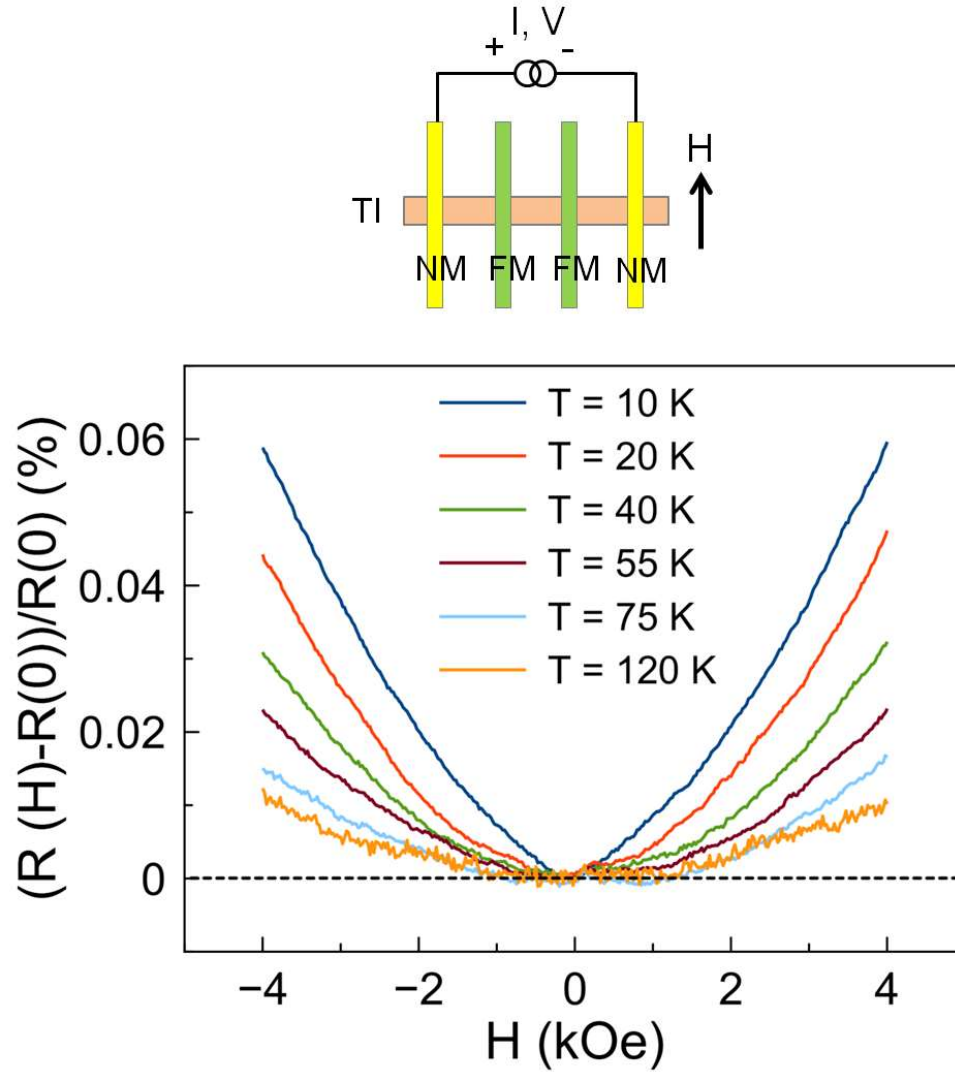


Figure 6.3: The temperature dependent magneto-transport measured through two Nb/Au contacts with the sweeping magnetic field applied along the electrodes (out-of-plane to the two side walls of Sb_2Te_3 nano-ribbon). The magnetoresistance (MR) behavior shows the weak anti-localization (WAL) effect at low temperature and decreases as temperature goes up, which suggests a conduction in Fermi Dirac states in the Sb_2Te_3 nanowire

For the nano-fabricated devices that conduct spin-dependent transport measurements, the FM electrodes can be complicatedly contributed to the magneto-transport data. In order to

simplify the data and focus on the spin-transport behavior of the TI nanowire, the two FM electrode contacts are fabricated to be straight wires and connected to Au electrodes to the outer contact pads. Also, the two-point magnetoresistance measurement has been performed between the one FM electrode and one NM electrode. Since there is no magnetic response of NM electrode, the 2-point MR measurement exhibits the behavior of single FM electrode. Thus, the property of the FM electrode can be unambiguously determined. Figure 6.4 and Figure 6.5 demonstrate the MR data of FM T2 and T3. In Figure 6.4(a)/(b), magnetic field was applied in-plane perpendicular/parallel to the FM electrode T2, the hysteresis and asymmetry MR loops demonstrate that T2 is a slightly exchange bias pinned spin valve electrode and is mostly dominated by anisotropic magnetoresistance (AMR) of Py layer. The magnitude of MR difference approves that it's AMR of Py layer. However, based on the GMR-like behavior in Figure 6.4(a), it suggests that the Py layer is magnetic-coupled to the top Co layer. For FM electrode T3, Figure 6.5(a) and 6.5(b), it's similar to the FM T2. The MR loops show the AMR of T3 Py layer, which is coupled to Co layer as well. But with much lower exchange bias pinning amplitude on the top Co layer.

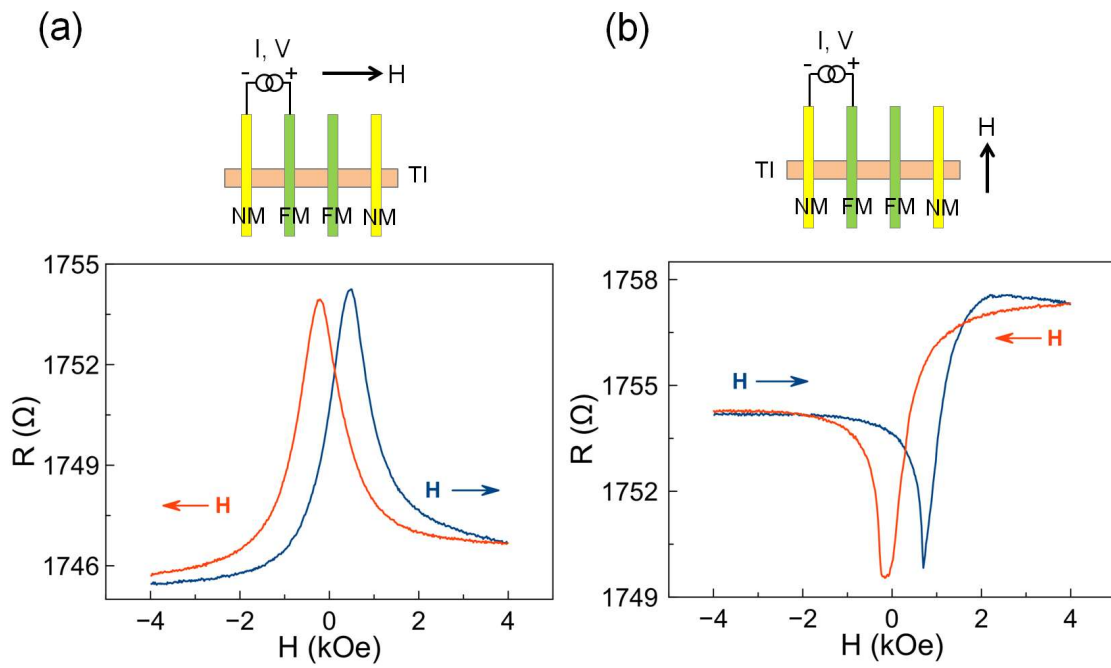


Figure 6.4: The two-point magnetoresistance measured through T1 and T2 with magnetic field applied (a) perpendicular (b) parallel to the FM T2 electrode.

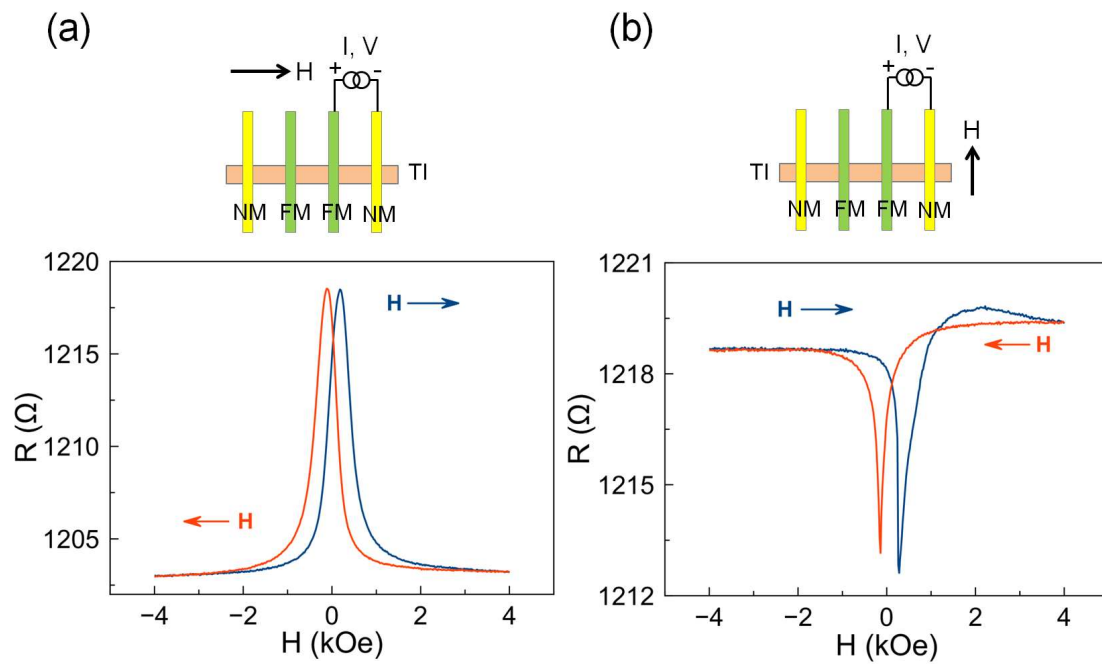


Figure 6.5: The two-point magnetoresistance measured through T3 and T4 with magnetic field applied (a) perpendicular (b) parallel to the FM T3 electrode.

The four-point magneto-transport measurements unambiguously pointing out the quantum transport to be dominated by massless Dirac fermions at the surface of the TI nanowires. Spin-momentum locking (SML) effect, the electron spin lies in-plane on the TI surface and lock at a right angle to the electrons momentum direction, allows a DC bias current to create a spin polarization in TI lateral device. This spin polarized net current can be detected electrically via the FM electrode contact.[70–72] Here we performed two types of measurement to detect SML behavior of the Sb_2Te_3 device. First, the DC current was applied from T3 to T4 and the responding voltage was measured from T2 to T1 with magnetic field applied along the electrodes, which is named non-local measurements. In Figure 6.6(a) and 6.6(b), a constant $+24 \mu\text{A}$ and $-24 \mu\text{A}$ current applied through the Sb_2Te_3 nanowire device, and a forward/reverse field sweep from negative/positive 0.75 kOe to positive/negative 0.75 kOe were performed to measure the non-local voltage. The blue/red curve represents the forward/reverse field sweep data. These measurements show a step-like voltage change behavior when the FM electrode flips its magnetization. This voltage hysteresis loop also changes completely in opposite when the current polarity was reversed. These measurements indicate the evidence of SML effect in the Sb_2Te_3 device.

This phenomenon can be explained by the schematic drawings, Figure 6.6(c) to 6.6(f). The propagation direction and spin population of electrons are considered at different magnetization orientation of FM electrodes. In Figure 6.6(c), the FM electrodes are aligned to the negative magnetic field (point down), thus the injected electrons with spin parallel to the magnetization (spin-down) have higher population propagating in TI. However, the SML effect of TSS limit spin down electrons propagating to the right towards electrode T4 for positive current, hence the potential difference between T2 and T1 is smaller due to the low spin accumulation. If the FM electrodes flip to upward direction (point up) as shown in Figure 6.6(d), the spin-up electrons now become the majority transporting on TI surface. Because the SML effect allows the spin-up electrons diffuse to the left which increases the spin accumulation under the FM detector (T2). Therefore, this result a larger voltage detec-

tion of non-local signal. The Figure 6.6(e) and (f) are the schematic drawings for negative applied current, which suggests a completely opposite trend of voltage detections. This step-like voltage detections in non-local geometry is quite surprising. However, there has been some discussion about the spin diffusion of TSS can be quite long for the applications.[73, 74] Therefore, this non-local measured data could be a direct proof of long spin diffusion length of spin transport through TSS channel. This also opens a possible quantitatively exploration of determining spin diffusion behaviors in TSS of the Sb_2Te_3 device.

The second type of 4-point measurements that we did is applied the current from T1 to T3 and measured the voltage between the T2 and T4. Similar results were obtained showing in Figure 6.7(a) and 6.7(b). The step-like voltage loops changing to opposite shape when the current polarity was reversed due to the SML effect of TSS in the Sb_2Te_3 nanowire device. The schematic explanations are shown from Figure 6.7(c) to 6.7(f).

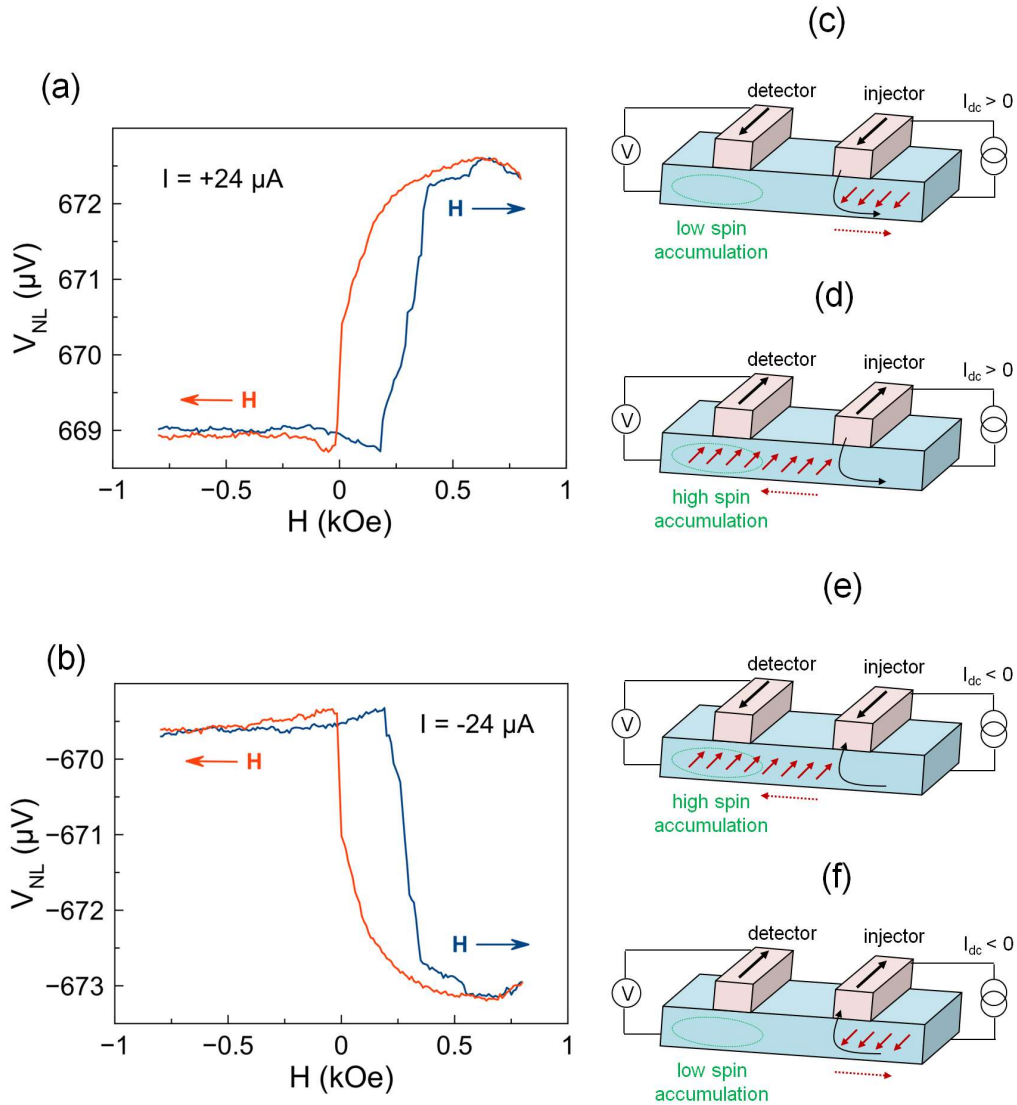


Figure 6.6: **The electrical detection of spin-momentum locking (SML) effect of the lateral Sb_2Te_3 nanowire device.** (a), (b) The field dependent voltage measured by applying current across T3 and T4 and detecting through T2 and T1 for $+24 \mu A$ and $-24 \mu A$, respectively. (c)/(d) schematic drawings of a positive current applied through T3 to T4 and the magnetization of FM electrodes point down/up. (e), (f) schematic drawings of a negative current applied through T3 to T4 and the magnetization of FM electrodes point down/up.

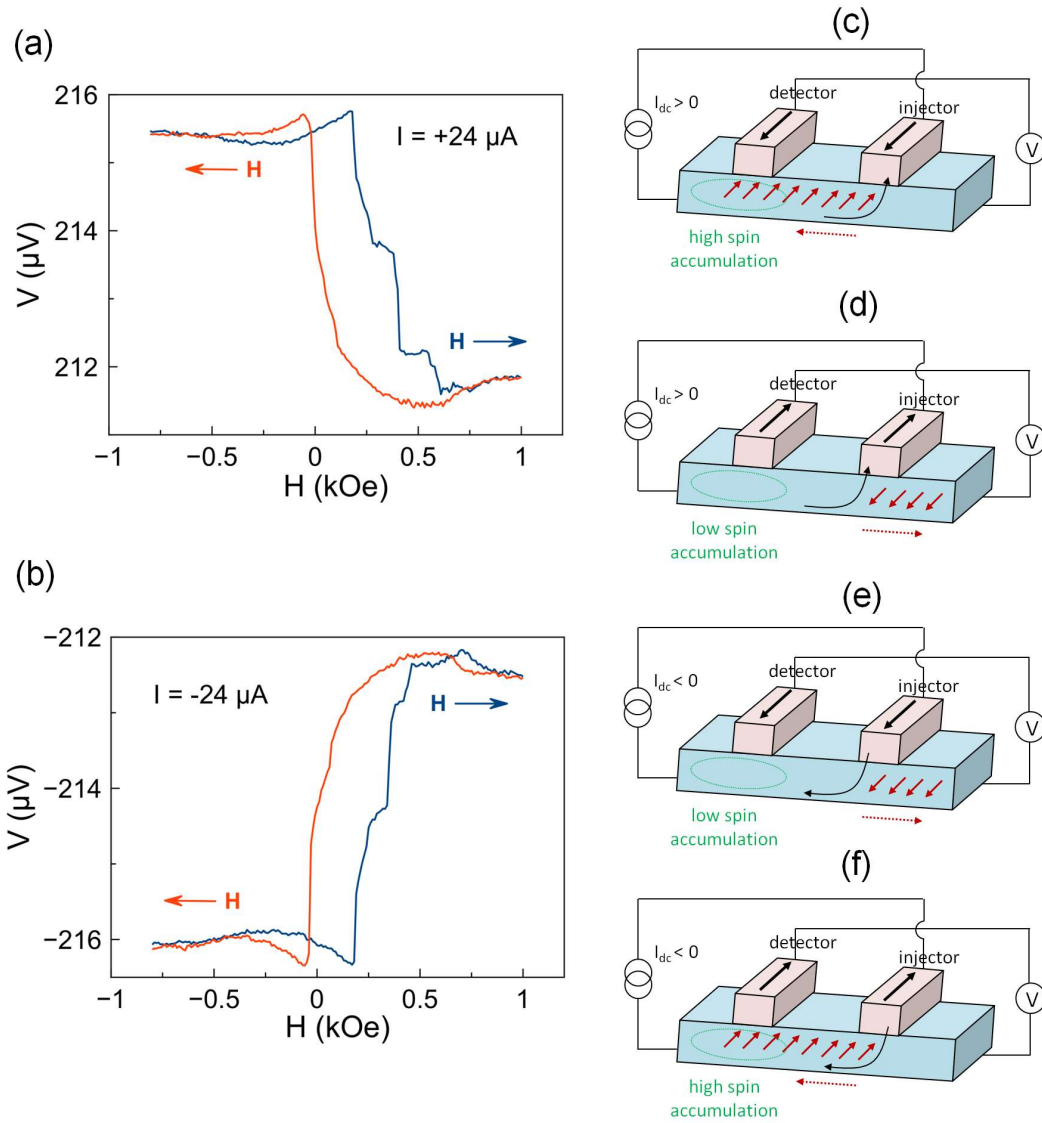


Figure 6.7: **The electrical detection of spin-momentum locking (SML) effect of the lateral Sb_2Te_3 nanowire device.** (a), (b) The field dependent voltage measured by applying current across T1 and T3 and detecting through T2 and T4 for $+24 \mu\text{A}$ and $-24 \mu\text{A}$, respectively. (c)/(d) schematic drawings of a positive current applied through T1 to T3 and the magnetization of FM electrodes point down/up. (e), (f) schematic drawings of a negative current applied through T1 to T3 and the magnetization of FM electrodes point down/up.

6.4 Temperature dependence of Magneto-transport properties

Unlike regular semiconductors, the conduction in bulk decreases as temperature goes down, most of 3D TIs show a decrease of resistivity when temperature decreases to cryogenic temperature. The competition of conducting in bulk or in TSS is always being an important problem for the electrical detection of SML effect in TI devices. Here, we show a temperature-dependent non-local voltage detections of the lateral Sb_2Te_3 device in Figure 6.8. In previous paragraph, we have discussed that the sharp switching of the detected voltage should be from the effect of SML that limit one polarity of spins' transportation on TSS. This temperature-dependent data also proves the SML behavior of the Sb_2Te_3 nanowire device. The coercivity of hysteresis loop shrank as temperature increased. Then, at certain temperature after 55 K, the step-like behavior disappeared. The data at 120 K became a common magneto-transport loop of non-local measurement which suggests a dominantly bulk conduction of the Sb_2Te_3 nanowire device.

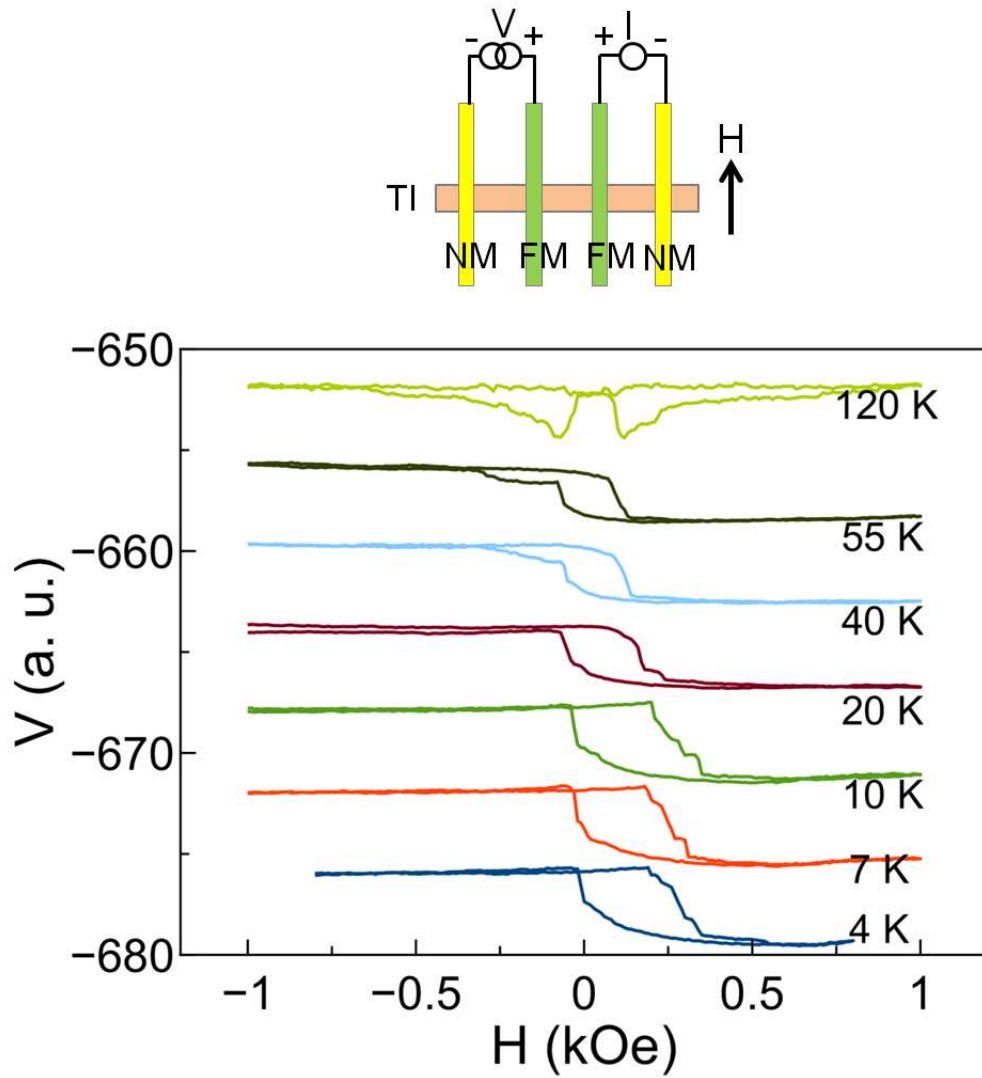


Figure 6.8: **Temperature dependence of SML effect in the lateral Sb_2Te_3 nanowire device.** Top shows the circuit schematic. The non-locally detected voltages measured from 4 K to 120 K.

Bibliography

- [1] M. N. Baibich, J. M. Broto, A. Fert, F. Nguyen Van Dau, F. Petroff, P. Etienne, G. Creuzet, A. Friederich, and J. Chazelas. Giant magnetoresistance of (001)fe/(001)cr magnetic superlattices. *Phys. Rev. Lett.*, 61:2472–2475, Nov 1988. doi: 10.1103/PhysRevLett.61.2472. URL <https://link.aps.org/doi/10.1103/PhysRevLett.61.2472>.
- [2] Igor Žutić, Jaroslav Fabian, and S Das Sarma. Spintronics: Fundamentals and applications. *Reviews of modern physics*, 76(2):323, 2004.
- [3] Daniel C Ralph and Mark D Stiles. Spin transfer torques. *Journal of Magnetism and Magnetic Materials*, 320(7):1190–1216, 2008.
- [4] Fanghui Ren, Albrecht Jander, Pallavi Dhagat, and Cathy Nordman. Radiation tolerance of magnetic tunnel junctions with mgo tunnel barriers. *IEEE Transactions on Nuclear Science*, 59(6):3034–3038, 2012.
- [5] G. Binasch, P. Grünberg, F. Saurenbach, and W. Zinn. Enhanced magnetoresistance in layered magnetic structures with antiferromagnetic interlayer exchange. *Phys. Rev. B*, 39:4828–4830, Mar 1989. doi: 10.1103/PhysRevB.39.4828. URL <https://link.aps.org/doi/10.1103/PhysRevB.39.4828>.
- [6] Michel Julliere. Tunneling between ferromagnetic films. *Physics Letters A*, 54(3):225–226, 1975.
- [7] Stuart SP Parkin, Christian Kaiser, Alex Panchula, Philip M Rice, Brian Hughes, Mahesh Samant, and See-Hun Yang. Giant tunnelling magnetoresistance at room temperature with mgo (100) tunnel barriers. *Nature materials*, 3(12):862, 2004.
- [8] Shinji Yuasa, Taro Nagahama, Akio Fukushima, Yoshishige Suzuki, and Koji Ando. Giant room-temperature magnetoresistance in single-crystal fe/mgo/fe magnetic tunnel junctions. *Nature materials*, 3(12):868, 2004.
- [9] Nevill Francis Mott. The electrical conductivity of transition metals. *In Proceedings of the Royal Society of London A: Mathematical, Physical and Engineering Sciences*, 153(880):699–717, Feb 1936.

- [10] Bernard Dieny, Virgil S Speriosu, Stuart SP Parkin, Bruce A Gurney, Dennis R Wilhoit, and Daniele Mauri. Giant magnetoresistive in soft ferromagnetic multilayers. *Physical Review B*, 43(1):1297, 1991.
- [11] Shinji Yuasa, Akio Fukushima, Hitoshi Kubota, Yoshishige Suzuki, and Koji Ando. Giant tunneling magnetoresistance up to 410% at room temperature in fully epitaxial co/ mg o/ co magnetic tunnel junctions with bcc co (001) electrodes. *Applied Physics Letters*, 89(4):042505, 2006.
- [12] Supriyo Datta and Biswajit Das. Electronic analog of the electro-optic modulator. *Applied Physics Letters*, 56(7):665–667, 1990.
- [13] J. E. Hirsch. Spin hall effect. *Phys. Rev. Lett.*, 83:1834–1837, Aug 1999. doi: 10.1103/PhysRevLett.83.1834. URL <https://link.aps.org/doi/10.1103/PhysRevLett.83.1834>.
- [14] Shufeng Zhang. Spin hall effect in the presence of spin diffusion. *Physical Review Letters*, 85(2):393–396, 7 2000. ISSN 0031-9007. doi: 10.1103/PhysRevLett.85.393.
- [15] Axel Hoffmann. Spin hall effects in metals. *IEEE transactions on magnetics*, 49(10): 5172–5193, 2013.
- [16] John C Slonczewski. Current-driven excitation of magnetic multilayers. *Journal of Magnetism and Magnetic Materials*, 159(1-2):L1–L7, 1996.
- [17] LALE Landau and Evgeny Lifshitz. On the theory of the dispersion of magnetic permeability in ferromagnetic bodies. *Phys. Z. Sowjetunion*, 8(153):101–114, 1935.
- [18] TL Gilbert. Armour research foundation project no. A05, 1956.
- [19] Markus König, Steffen Wiedmann, Christoph Brüne, Andreas Roth, Hartmut Buhmann, Laurens W Molenkamp, Xiao-Liang Qi, and Shou-Cheng Zhang. Quantum spin hall insulator state in hgte quantum wells. *Science*, 318(5851):766–770, 2007.
- [20] Andreas Roth, Christoph Brüne, Hartmut Buhmann, Laurens W Molenkamp, Joseph Maciejko, Xiao-Liang Qi, and Shou-Cheng Zhang. Nonlocal transport in the quantum spin hall state. *Science*, 325(5938):294–297, 2009.
- [21] Liang Fu and Charles L Kane. Topological insulators with inversion symmetry. *Physical Review B*, 76(4):045302, 2007.
- [22] Hai-Jun Zhang, Chao-Xing Liu, Xiao-Liang Qi, Xiao-Yu Deng, Xi Dai, Shou-Cheng Zhang, and Zhong Fang. Electronic structures and surface states of the topological insulator bi 1- x sb x. *Physical Review B*, 80(8):085307, 2009.
- [23] Haijun Zhang, Chao-Xing Liu, Xiao-Liang Qi, Xi Dai, Zhong Fang, and Shou-Cheng Zhang. Topological insulators in bi 2 se 3, bi 2 te 3 and sb 2 te 3 with a single dirac cone on the surface. *Nature physics*, 5(6):438, 2009.

- [24] Yuqi Xia, Dong Qian, David Hsieh, L Wray, Arijeet Pal, Hsin Lin, Arun Bansil, DHYS Grauer, Yew San Hor, Robert Joseph Cava, et al. Observation of a large-gap topological-insulator class with a single dirac cone on the surface. *Nature physics*, 5(6):398, 2009.
- [25] S. I. Kiselev, J. C. Sankey, I. N. Krivorotov, N. C. Emley, R. J. Schoelkopf, R. A. Buhrman, and D. C. Ralph. Microwave oscillations of a nanomagnet driven by a spin-polarized current. *Nature*, 425:380–383, 2003.
- [26] Tingsu Chen, Randy K Dumas, Anders Eklund, Pranaba K Muduli, Afshin Houshang, Ahmad A Awad, Philipp Dürrenfeld, B Gunnar Malm, Ana Rusu, and Johan Åkerman. Spin-torque and spin-hall nano-oscillators. *Proceedings of the IEEE*, 104(10):1919–1945, 2016.
- [27] L Berger. Emission of spin waves by a magnetic multilayer traversed by a current. *Physical Review B*, 54(13):9353, 1996.
- [28] Andrei Slavin and Vasil Tiberkevich. Nonlinear auto-oscillator theory of microwave generation by spin-polarized current. *IEEE Transactions on Magnetism*, 45(4):1875–1918, 2009.
- [29] Q Mistral, Joo-Von Kim, T Devolder, P Crozat, C Chappert, JA Katine, MJ Carey, and K Ito. Current-driven microwave oscillations in current perpendicular-to-plane spin-valve nanopillars. *Applied physics letters*, 88(19):192507, 2006.
- [30] PM Braganca, BA Gurney, BA Wilson, JA Katine, S Maat, and JR Childress. Nanoscale magnetic field detection using a spin torque oscillator. *Nanotechnology*, 21(23):235202, 2010.
- [31] William H Rippard, Matthew R Pufall, S Kaka, Stephen E Russek, and Thomas J Silva. Direct-current induced dynamics in $co_90fe_{10}/ni_{80}fe_{20}$ point contacts. *Physical Review Letters*, 92(2):027201, 2004.
- [32] K Ando, S Takahashi, K Harii, K Sasage, J Ieda, S Maekawa, and E Saitoh. Electric manipulation of spin relaxation using the spin hall effect. *Physical review letters*, 101(3):036601, 2008.
- [33] Xin Fan, Jun Wu, Yunpeng Chen, Matthew J Jerry, Huaiwu Zhang, and John Q Xiao. Observation of the nonlocal spin-orbital effective field. *Nature communications*, 4:1799–1799, 2013.
- [34] Jairo Sinova, Dimitrie Culcer, Q Niu, NA Sinitsyn, T Jungwirth, and AH MacDonald. Universal intrinsic spin hall effect. *Physical Review Letters*, 92(12):126603, 2004.
- [35] Luqiao Liu, Takahiro Moriyama, DC Ralph, and RA Buhrman. Spin-torque ferromagnetic resonance induced by the spin hall effect. *Physical review letters*, 106(3):036601, 2011.

- [36] Vladislav E Demidov, Sergei Urazhdin, Henning Ulrichs, Vasyl Tiberkevich, Andrei Slavin, Dietmar Baither, Guido Schmitz, and Sergej O Demokritov. Magnetic nano-oscillator driven by pure spin current. *Nature materials*, 11(12):1028–1031, 2012.
- [37] RH Liu, WL Lim, and S Urazhdin. Spectral characteristics of the microwave emission by the spin hall nano-oscillator. *Physical review letters*, 110(14):147601, 2013.
- [38] M Ranjbar, P Drrenfeld, M Haidar, E Iacocca, M Balinskiy, TQ Le, M Fazlali, A Houshang, AA Awad, RK Dumas, et al. Cofeb-based spin hall nano-oscillators. *IEEE Magnetics Letters*, 5:1–4, 2014.
- [39] RH Liu, WengLee Lim, Sergei Urazhdin, et al. Dynamical skyrmion state in a spin current nano-oscillator with perpendicular magnetic anisotropy. *Physical review letters*, 114(13):137201, 2015.
- [40] VE Demidov, S Urazhdin, A Zholud, AV Sadovnikov, and SO Demokritov. Nanoconstriction-based spin-hall nano-oscillator. *Applied Physics Letters*, 105(17):172410, 2014.
- [41] AA Awad, P Dürrenfeld, A Houshang, M Dvornik, E Iacocca, RK Dumas, and Johan Åkerman. Long-range mutual synchronization of spin hall nano-oscillators. *Nature Physics*, page 14, 2016.
- [42] Zheng Duan, Andrew Smith, Liu Yang, Brian Youngblood, Jürgen Lindner, Vladislav E Demidov, Sergej O Demokritov, and Ilya N Krivorotov. Nanowire spin torque oscillator driven by spin orbit torques. *Nature communications*, 5:5616, 2014.
- [43] Martin Collet, Xavier De Milly, O dAllivy Kelly, Vladimir V Naletov, Rozenn Bernard, Paolo Bortolotti, J Ben Youssef, VE Demidov, SO Demokritov, JL Prieto, et al. Generation of coherent spin-wave modes in yttrium iron garnet microdiscs by spin-orbit torque. *Nature communications*, 7:10377, 2016.
- [44] Alexey V Nazarov, Konstantin Nikolaev, Zheng Gao, Haeseok Cho, and Dion Song. Microwave generation in mgo magnetic tunnel junctions due to spin transfer effects. *Journal of Applied Physics*, 103(7):07A503, 2008.
- [45] Thibaut Devolder, Laurence Bianchini, Joo-Von Kim, Paul Crozat, Claude Chappert, Sven Cornelissen, Maaïke Op de Beeck, and Liesbet Lagae. Auto-oscillation and narrow spectral lines in spin-torque oscillators based on mgo magnetic tunnel junctions. *Journal of applied physics*, 106(10):103921, 2009.
- [46] Sumito Tsunegi, Kay Yakushiji, Akio Fukushima, Shinji Yuasa, and Hitoshi Kubota. Microwave emission power exceeding 10 μ w in spin torque vortex oscillator. *Applied Physics Letters*, 109(25):252402, 2016.
- [47] Hitoshi Kubota, Kay Yakushiji, Akio Fukushima, Shingo Tamaru, Makoto Konoto, Takayuki Nozaki, Shota Ishibashi, Takeshi Saruya, Shinji Yuasa, Tomohiro Taniguchi, et al. Spin-torque oscillator based on magnetic tunnel junction with a perpendicularly

- magnetized free layer and in-plane magnetized polarizer. *Applied Physics Express*, 6(10):103003, 2013.
- [48] Zhongming Zeng, Pedram Khalili Amiri, Ilya N Krivorotov, Hui Zhao, Giovanni Finocchio, Jian-Ping Wang, Jordan A Katine, Yiming Huai, Juergen Langer, Kosmas Galatsis, et al. High-power coherent microwave emission from magnetic tunnel junction nano-oscillators with perpendicular anisotropy. *Acs Nano*, 6(7):6115–6121, 2012.
- [49] IN Krivorotov, DV Berkov, NL Gorn, NC Emley, JC Sankey, DC Ralph, and RA Buhrman. Large-amplitude coherent spin waves excited by spin-polarized current in nanoscale spin valves. *Physical Review B*, 76(2):024418, 2007.
- [50] PM Braganca, BA Gurney, AGF Garcia, JA Katine, and JR Childress. Dependence of nonlinearity and spectral linewidth on bias current in large-angle spin-torque oscillators. *Physical Review Applied*, 4(1):014017, 2015.
- [51] Shehzaad Kaka, Matthew R. Pufall, William H. Rippard, Thomas J. Silva, Stephen E. Russek, and Jordan A. Katine. Mutual phase-locking of microwave spin torque nano-oscillators. *Nature*, 437:389–392, 2005.
- [52] Ye Pogoryelov, PK Muduli, Stefano Bonetti, Fred Mancoff, and Johan Åkerman. Spin-torque oscillator linewidth narrowing under current modulation. *Applied Physics Letters*, 98(19):192506, 2011.
- [53] Joo-Von Kim, Vasil Tiberkevich, and Andrei N Slavin. Generation linewidth of an auto-oscillator with a nonlinear frequency shift: Spin-torque nano-oscillator. *Physical review letters*, 100(1):017207, 2008.
- [54] SSP Parkin. Origin of enhanced magnetoresistance of magnetic multilayers: Spin-dependent scattering from magnetic interface states. *Physical review letters*, 71(10):1641, 1993.
- [55] PA Grünberg. Exchange anisotropy, interlayer exchange coupling and gmr in research and application. *Sensors and Actuators A: Physical*, 91(1):153–160, 2001.
- [56] Mannan Ali, Christopher H Marrows, M Al-Jawad, Bryan J Hickey, Arkajyoti Misra, Ulrich Nowak, and Klaus-Dieter Usadel. Antiferromagnetic layer thickness dependence of the irmn/co exchange-bias system. *Physical review B*, 68(21):214420, 2003.
- [57] GE Rowlands, T Rahman, JA Katine, J Langer, A Lyle, H Zhao, JG Alzate, AA Kovalev, Y Tserkovnyak, ZM Zeng, et al. Deep subnanosecond spin torque switching in magnetic tunnel junctions with combined in-plane and perpendicular polarizers. *Applied Physics Letters*, 98(10):102509, 2011.
- [58] SAR Wynchank, AE Cox, and CH Collie. The thermal neutron capture cross section of a natural boron. *Nuclear Physics*, 62(3):491–496, 1965.

- [59] A Scarpa, A Paccagnella, F Montera, G Ghibaudo, G Pananakakis, G Ghidini, and PG Fuochoi. Ionizing radiation induced leakage current on ultra-thin gate oxides. *IEEE Transactions on Nuclear Science*, 44(6):1818–1825, 1997.
- [60] James R Schwank, Marty R Shaneyfelt, Daniel M Fleetwood, James A Felix, Paul E Dodd, Philippe Paillet, and Véronique Ferlet-Cavrois. Radiation effects in mos oxides. *IEEE Transactions on Nuclear Science*, 55(4):1833–1853, 2008.
- [61] Conversion of absorbed-dose(water) to absorbed-dose(silicon). <https://www.nist.gov/programs-projects/high-dose-dosimetry>. 2010.
- [62] Yulieth C Arango, Liubing Huang, Chaoyu Chen, Jose Avila, Maria C Asensio, Detlev Grützmacher, Hans Lüth, Jia Grace Lu, and Thomas Schäpers. Quantum transport and nano angle-resolved photoemission spectroscopy on the topological surface states of single sb 2 te 3 nanowires. *Scientific reports*, 6:29493, 2016.
- [63] Charles L Kane and Eugene J Mele. Z 2 topological order and the quantum spin hall effect. *Physical review letters*, 95(14):146802, 2005.
- [64] CH Li, OMJ Vant Erve, JT Robinson, Y Liu, L Li, and BT Jonker. Electrical detection of charge-current-induced spin polarization due to spin-momentum locking in bi 2 se 3. *Nature nanotechnology*, 9(3):218, 2014.
- [65] André Dankert, Johannes Geurs, M Venkata Kamalakar, Sophie Charpentier, and Saroj P Dash. Room temperature electrical detection of spin polarized currents in topological insulators. *Nano letters*, 15(12):7976–7981, 2015.
- [66] Zilong Jiang, Cui-Zu Chang, Massoud Ramezani Masir, Chi Tang, Yadong Xu, Jagadeesh S Moodera, Allan H MacDonald, and Jing Shi. Enhanced spin seebeck effect signal due to spin-momentum locked topological surface states. *Nature communications*, 7:11458, 2016.
- [67] Jianshi Tang, Li-Te Chang, Xufeng Kou, Koichi Murata, Eun Sang Choi, Murong Lang, Yabin Fan, Ying Jiang, Mohammad Montazeri, Wanjun Jiang, et al. Electrical detection of spin-polarized surface states conduction in (bi0. 53sb0. 47) 2te3 topological insulator. *Nano letters*, 14(9):5423–5429, 2014.
- [68] WH Wang, W Han, K Pi, KM McCreary, F Miao, W Bao, CN Lau, and RK Kawakami. Growth of atomically smooth mgo films on graphene by molecular beam epitaxy. *Applied Physics Letters*, 93(18):183107, 2008.
- [69] Shinobu Hikami, Anatoly I Larkin, and Yosuke Nagaoka. Spin-orbit interaction and magnetoresistance in the two dimensional random system. *Progress of Theoretical Physics*, 63(2):707–710, 1980.
- [70] AA Burkov and DG Hawthorn. Spin and charge transport on the surface of a topological insulator. *Physical review letters*, 105(6):066802, 2010.

- [71] Dimitrie Culcer, EH Hwang, Tudor D Stanescu, and S Das Sarma. Two-dimensional surface charge transport in topological insulators. *Physical review B*, 82(15):155457, 2010.
- [72] Oleg V Yazyev, Joel E Moore, and Steven G Louie. Spin polarization and transport of surface states in the topological insulators Bi_2Se_3 and Bi_2Te_3 from first principles. *Physical review letters*, 105(26):266806, 2010.
- [73] Lingjian Kong, Yong Zhou, Song Liu, Zhu Lin, Liang Zhang, Fang Lin, Dongsheng Tang, Han-Chun Wu, Junfeng Liu, Hai-Zhou Lu, et al. Spin-polarized surface state transport in a topological kondo insulator Sb_2Te_3 nanowire. *Physical Review B*, 95(23):235410, 2017.
- [74] AR Mellnik, JS Lee, A Richardella, JL Grab, PJ Mintun, Mark H Fischer, Abolhassan Vaezi, Aurelien Manchon, E-A Kim, N Samarth, et al. Spin-transfer torque generated by a topological insulator. *Nature*, 511(7510):449, 2014.